

INFORMATION TO USERS

This manuscript has been reproduced from the microfilm master. UMI films the text directly from the original or copy submitted. Thus, some thesis and dissertation copies are in typewriter face, while others may be from any type of computer printer.

The quality of this reproduction is dependent upon the quality of the copy submitted. Broken or indistinct print, colored or poor quality illustrations and photographs, print bleedthrough, substandard margins, and improper alignment can adversely affect reproduction.

In the unlikely event that the author did not send UMI a complete manuscript and there are missing pages, these will be noted. Also, if unauthorized copyright material had to be removed, a note will indicate the deletion.

Oversize materials (e.g., maps, drawings, charts) are reproduced by sectioning the original, beginning at the upper left-hand corner and continuing from left to right in equal sections with small overlaps. Each original is also photographed in one exposure and is included in reduced form at the back of the book.

Photographs included in the original manuscript have been reproduced xerographically in this copy. Higher quality 6" x 9" black and white photographic prints are available for any photographs or illustrations appearing in this copy for an additional charge. Contact UMI directly to order.

UMI

**A Bell & Howell Information Company
300 North Zeeb Road, Ann Arbor MI 48106-1346 USA
313/761-4700 800/521-0600**

WASHINGTON UNIVERSITY

Department of Chemistry

Dissertation Committee:

Lee G. Sobotka, Chairperson

Robert J. Charity

Willem H. Dickhoff

Martin H. Israel

Ronald A. Lovett

Demetrios G. Sarantites

Robert Yaris

DYNAMICAL ASPECTS OF INTERMEDIATE-ENERGY
HEAVY-ION COLLISIONS

by

James Francis Dempsey

A dissertation presented to the
Graduate School of Arts and Sciences
of Washington University in
partial fulfillment of the
requirements for the degree
of Doctor of Philosophy

May, 1997

Saint Louis, Missouri

UMI Number: 9730938

**UMI Microform 9730938
Copyright 1997, by UMI Company. All rights reserved.**

**This microform edition is protected against unauthorized
copying under Title 17, United States Code.**

UMI
300 North Zeeb Road
Ann Arbor, MI 48103

ABSTRACT OF THE DISSERTATION

Dynamical Aspects of Intermediate-Energy Heavy-Ion Collisions

by

James Francis Dempsey

Doctor of Philosophy in Chemistry

Washington University in St. Louis, 1997

Professor Lee G. Sobotka, Chairperson

The production of neutrons, light charged particles (LCPs), and intermediate-mass fragments (IMFs), from the four reactions $55 \text{ MeV/A } ^{124,136}\text{Xe} + ^{112,124}\text{Sn}$, is studied with an experimental apparatus which is highly efficient for the detection of both charged particles and neutrons. The IMFs are found more localized in the mid-velocity region (parallel velocity close to center of mass) than are the LCPs, and the detected multiplicity of IMFs depends linearly on the charge lost from the projectile. IMF multiplicity is found to be largely independent of the neutron excess of the system, aside from a slight increase with increasing neutron excess that is expected from statistical-model simulations. Remnants of the projectile, with very little velocity reduction, are found for most of the reaction cross section. Isotopic and isobaric fragment yields in the projectile-velocity region indicate that charge-to-mass ratio neutralization is generally not achieved but is approached when little remains of the projectile. For all systems, the fragments found in the mid-velocity region are substantially more neutron rich than those found in the velocity region dominated by the emission from the projectile. This observation can be qualitatively accounted for if the mid-velocity source (or sources) is either more neutron rich or smaller, with

the same neutron-to-proton ratio, than the source with the velocity of the projectile. The observations of this work suggest that the intermediate mass fragments are, to a large extent, formed dynamically by a multiple neck rupture or a proximity-fission type mechanism. Though it remains unexplained, this process enhances the neutron-to-proton ratio of the emitted fragments. This scenario is reminiscent of low-energy ternary fission and one predicted by Boltzmann-Uehling-Uhlenbeck (BUU) calculations. However, these calculations predict too much velocity damping of the projectile remnant and do not produce a mid-velocity neutron enhancement. The calculations improve in the prediction of the extent of velocity damping when the in-medium nucleon-nucleon cross sections and the cost of creating low density material are reduced. A neutron-rich mid-velocity region of unbound nucleons can be produced if small symmetric clusters (e.g. α -particles) are formed in the expansion of this region during the final stages of the reaction. The equilibrium expectations of isospin observables for multifragmentation originating from a liquid-gas phase transition in nuclear matter are discussed. A fractionation of the proton and neutron concentrations among different density phases in such models is predicted and the influence of finite Coulomb interactions is investigated and found to be significant.

Contents

List of Tables	vi
List of Figures	vii
Acknowledgments	xiii
1 Introduction	1
1.1 Background	1
1.2 Experimental Objective	6
1.3 Theoretical Objective	7
2 Experimental Aspects	8
2.1 Experimental Layout	8
2.2 The Forward Array	10
2.2.1 Principle of Operation	10
2.2.2 Electronics	13
2.2.3 Calibration	16
2.3 The MINIWALL/BALL Array	18
2.3.1 Principle of Operation	18
2.3.2 Electronics	20
2.3.3 Calibration	27
2.3.4 Further Description	28
2.4 The Superball Neutron Multiplicity Meter	28
2.4.1 Principle of Operation	28
2.4.2 Electronics	31
2.4.3 Calibration	34
2.4.4 Further Description	35

2.5	Trigger Logic	35
2.6	Acquisition Code and Data Format	36
3	Data Analysis	37
3.1	Multiplicity Correlations	37
3.1.1	Motivation	37
3.1.2	Neutron and Charged Particle Correlations	37
3.1.3	IMF and Z_{plf} Correlations	42
3.1.4	Summary	45
3.2	Emission Patterns in Velocity Space	45
3.2.1	Motivations	45
3.2.2	Z_{plf} Emission Patterns	46
3.2.3	IMF and LCP Emission Patterns	46
3.2.4	IMF- Z_{plf} and LCP- Z_{plf} Azimuthal Correlations	50
3.2.5	Summary	51
3.3	Isotope Ratios	51
3.3.1	Motivation	51
3.3.2	Charge Neutralization	53
3.3.3	The N/Z Signature of IMFs and LCPs	56
3.3.4	Summary	56
4	Theoretical Models and Simulations	57
4.1	Statistical-Model Simulations	57
4.1.1	Standard Statistical Models: GEMINI	57
4.1.2	Expanding Evaporating Source Model	63
4.1.3	Comparison of Statistical Models and Data	65
4.1.4	Summary	70
4.2	Dynamical Reaction Simulations	70
4.2.1	The BUU Transport Equation	70
4.2.2	Comparison of Dynamical Models and Data	74
4.2.3	Inclusion of Light-Cluster Degrees of Freedom	76
4.2.4	Summary	79
4.3	Liquid-Gas Phase Transitions in Asymmetric Nuclear Matter	80
4.3.1	Equilibrium Expectations	80
4.3.2	Two-Component van der Waals Liquid	85

4.3.3	Two-Component Hard-Core Skyrme Liquid	96
4.3.4	Summary	103
5	Conclusions	104
5.1	Experimental Findings	104
5.2	Theoretical Insights	105
5.3	Future Studies	106
	Bibliography	108

List of Tables

2.1	55 MeV*A $^{124,136}\text{Xe} + ^{112,124}\text{Sn}$	10
2.2	Ions Used in Calibration of Forward Array	16
3.1	Multiplicity Shifts	44
4.1	Commonly Used EOS Parameters for BUU Simulations	74

List of Figures

1.1	Density distributions projected on the reaction plane which result from BUU simulations of $^{136}\text{Xe} + ^{209}\text{Bi}$ collisions at 28 MeV/nucleon for three different equations of state. Notice that PLFs and TLFs are connected by a “neck”-like structure extended between them and that a neck fragment appears to have been formed in the lower right panel.	5
2.1	A layout of the experimental setup is shown. The devices described in the following section are labeled. The beam which enters from the left of the figure, is approximately 1.8 meters from the floor. A computer-controlled target ladder assembly, not shown, was used to select the target.	9
2.2	A Photograph of the front and back sides of the $280\ \mu\text{m}$ ($67.05\ \frac{\text{mg}}{\text{cm}^2}$) thick annular silicon-strip detector used as the first element of the Forward Array.	11
2.3	A schematic of a single element of the forward array is displayed. A ΔE signal is produced by charge collection in a pie-sector of the annular-silicon first element. An E signal is then produced in the corresponding CsI(Tl) crystal as luminescence which is collected via a light-pipe and converted to charge in the PIN diode. The CsI(Tl) crystal and light-pipe are wrapped in reflecting aluminized mylar to increase light collection.	12
2.4	A two-dimensional histogram of the calibrated output of the Forward Array is plotted such that the first-element output (ΔE) is on the x-axis and the the second-element output (E) is on the y-axis.	14
2.5	A block diagram describing the electronics used to read out the elements of the Forward Array.	15

2.6	Fitted energy-calibration points for ions which traversed the pie-sector of the first element and stopped in the corresponding second element of the Forward Array.	17
2.7	A schematic of the elements of the MINIWALL/BALL detectors. . .	19
2.8	A schematic of the MINIWALL detector array.	21
2.9	A schematic of the MINIBALL detector array.	22
2.10	A two-dimensional histogram of the digitized FAST and SLOW regions from a MINIWALL detector with proper resolution.	23
2.11	A two-dimensional histogram of the digitized TAIL and SLOW regions from a MINIWALL detector with proper resolution.	24
2.12	A two-dimensional histogram of the digitized TAIL and SLOW regions from a MINIWALL detector with poor resolution. The loss of p,d,t resolution is evident.	25
2.13	A schematic of the charge-integration regions used to perform particle identification on the response of the MINIWALL/BALL detectors . .	26
2.14	A block-diagram schematic of the electronics used to read out the MINIBALL detectors. The electronics used to read out the MINIWALL detectors are the same in principle, with minor differences. Taken from R.T. deSouza et al.[59].	27
2.15	A perspective view of the Superball Neutron Multiplicity Meter. . .	29
2.16	The mean-free path of neutrons as a function of energy in BC521, a commercially available Gd-loaded inorganic scintillator, that is very similar to the scintillator fluid used in the Superball.	30
2.17	The results of a simulated distribution of capture times expected for neutrons with an initial energy of 1.0 MeV that are moderated in the Superball.	31
2.18	A block-diagram schematic of the electronics used to read out the Superball.	32
2.19	A time sequence of logical signals produced by the Superball.	33

3.1	Correlations between the number of detected charged particles (N_c) and the number of detected neutrons (N_n) for all 4 systems. The solid lines depict the ridges of the correlations (most probable value of N_n for each value of N_c). The dashed lines bracket the ridge and define the region used for generating mean values. The small second ridge at low values of N_n is due to instrumental effects.	39
3.2	Average value of N_n for each value of N_c for the 4 systems. The averages are calculated from the data inside the bracketed region (dotted lines) in figure 20. These data have been corrected for background but not efficiency.	40
3.3	The dependences of the average number of detected IMFs ($\langle N_{imf} \rangle$) on (a) the number of detected charged particles (N_c), (b) the number of detected light-charged particles (N_{lc}), and (c) the number of detected neutrons (N_n) are shown on the left-hand side. On the right-hand side, the dependences of (d) N_{imf} , (e) N_{lc} , and (f) N_n on the charge of the projectile-like fragment (Z_{plf}) are shown. Each panel shows the dependences for all four systems. The same key is used throughout.	41
3.4	The same as figure 22 but with the multiplicity shifts indicated in table 3.1 applied to the data.	43
3.5	Contour plots showing the variation of cross section with the the charge of the projectile-like fragment Z_{plf} and the energy per nucleon E/A for different numbers of coincident intermediate-mass fragments. The data from the LL system is displayed here. The dotted line is at the projectile energy 55 MeV/A. The data for the other systems look very similar.	47
3.6	The variation of $\langle E/A_{plf} \rangle$ (a), $\langle Z_{plf} \rangle$ (b), and the fractional yield or normalized probability of detecting a given number of IMFs (c), are shown as a function of the number of detected IMFs for all four systems.	48
3.7	Galilean-invariant cross-section maps for α -particles (left-hand side), ${}^6\text{He}$ fragments (center), and Li fragments (right-hand side) for four different gates on the charge of the projectile remnant, Z_{plf} (as indicated) for the HH system. These plots are boosted into the center-of-mass system and use a logarithmic color scale. The projectile velocity is ~ 5.0 cm/ns.	49

3.8	Azimuthal distributions of Li fragments relative to the PLFs for 5 bins in Z_{plf} and three cuts in velocity parallel to the beam velocity V_{par} (in the center-of-mass system) for the HH system. Because the PLFs and the Li fragments are detected in different arrays (FA and MINI-WALL/BALL, respectively), the detection method does not impose an auto-correlation. The angle, $\Delta\Phi$ is defined relative to the PLF direction.	52
3.9	The relative yield of ${}^6\text{He}$ to ${}^{3,4}\text{He}$ (a)-(c) and ${}^6\text{He}$ to Li (d)-(f) are shown as a function of V_{par} (in the center-of-mass system) for several gates on Z_{plf} . The key for the lines is the same as that used in the previous figures. For clarity, the data points themselves are suppressed. The statistical uncertainties are generally less than 5% with the exception of the LH system when Z_{plf} is large, in which case the statistical uncertainties are (when these data are shown) less than 15%. The ratios in (f) have been multiplied by a factor of 5 for display purposes. . .	54
3.10	The relative yield of ${}^6\text{He}$ to ${}^{3,4}\text{He}$, ${}^6\text{He}$ to Li, and t to ${}^3\text{He}$ are shown for the four systems for several gates on Z_{plf} . Sections (a), (b), and (c) display the ratios for the mid-velocity region, $0 \text{ cm/ns} < V_{par}(\text{centerofmass}) < 2.0 \text{ cm/ns}$, while sections (d), (e), and (f) display the ratios for the projectile region, $3.0 \text{ cm/ns} < V_{par}(\text{centerofmass}) < 7.0 \text{ cm/ns}$ for sections (d) and (e) and 4 cm/ns for section f). (The range had to be reduced for the last ratio due to the limitations imposed by the rather low t punch-through energy.)	55
4.1	The results of statistical-model calculations for the decay of excited ${}^{136}\text{Xe}$ and ${}^{124}\text{Xe}$ projectiles as a function of the initial excitation energy per nucleon (a),(b), and (c) and fragment size $\eta = A_{source}/A_{total}$ at fixed charge-to-mass ratio (d), (e), and (f). In the latter case, the charge-to-mass ratio is that of the H projectile, ${}^{136}\text{Xe}$, and the initial excitation energy per nucleon is 3.68 (arrow on left.) The circles are the results from GEMINI calculations and the diamonds are the results from EES. The key for the lines is the same as that used in the previous figures.	66

4.2	Statistical-model predictions (EES) of the percentage of IMFs which survive sequential decay and retain their IMF status as a function of the initial excitation energy per nucleon in the system (E_{int}^*/A [MeV]). The solid line connects results for a ^{136}Xe source while the dotted line connects the results for a ^{124}Xe source. The dashed line is the percentage difference in the survivability between the ^{136}Xe source and the ^{124}Xe source.	69
4.3	The results of BUU calculations for (a) the exit channel value of E/A for the projectile-like fragment and (b) the mass contained in mid-velocity IMFs at 250 fm/c. The circles show the results for a stiff ($\kappa = 380$ MeV) equation of state, the diamonds show the results for a soft ($\kappa = 200$ MeV) equation of state, the X's show the results for the ISO-SOFT equation of state which has an improved treatment of the isospin (N/Z) degree of freedom, and the squares show the results for the iso-soft equation of state when the scattering cross sections have a density-dependent reduction.	75
4.4	BUU simulation of a collision at an impact parameter of 8.8 fm between ^{136}Xe and ^{124}Xe at 55 MeV/nucleon[89]. The different panels show projections (in the plane defined by the projectile momentum (Z -axis) and the impact parameter (X -axis)) of the total (a),(b),(c), neutron (d),(e),(f), and proton (g),(h),(i) densities. The nucleons bound in light clusters are excluded from the contour plots (d-i). Sections (j-l) display the N/Z ratio $R_{n/p}$ as a function of the distance D from the center of mass along the projection of the space coordinates on the projectile-target separation axis, excluding (solid) and including (open) the nucleons bound in small clusters.	78
4.5	The binodal surface defining the phase-coexistence boundary for asymmetric nuclear matter plotted in Temperature T [MeV], pressure P [MeV/fm ³], and proton fraction Y space. The critical temperature T_c at $Y = 0.5$, the line of equal concentrations(LEC), the line of critical points (LCP), Taken from Müller and Serot.	82
4.6	An isothermal slice of the binodal surface shown in figure 4.5 for $T=10$ MeV. The critical point (CP), the point of equal concentration (EC), and the point of maximal asymmetry (MA) are all indicated.	83

4.7	A hard-core and Yukawa interaction that is consistent with the parameters of the van der Waals parameters used in this study.	88
4.8	The isospin asymmetry energy $S\left(\frac{\rho}{\rho_0}\right)$ as a function of $\frac{\rho}{\rho_0}$ for the three parameterizations suggested in the literature [97].	89
4.9	A sketch of the binodal surface defining the phase-coexistence boundary for the two-component van der Waals model plotted in Temperature T [MeV], density ρ [fm^{-3}], and proton fraction Y space, with and without the influence of finite Coulomb interactions.	93
4.10	The proton fraction found in the low-density phase Y_{gas} as a function of the proton fraction found in the high-density phase Y_{liquid} at equilibrium for four different temperatures with Coulomb (solid line) and without Coulomb (dashed line) for the Two-Component van der Waals Model. The dotted line marks equal concentrations in the phases. Above this line the gas phase is proton rich and below this line the gas phase is neutron rich relative to the liquid phase.	94
4.11	The liquid-gas phase coexistence curve for symmetry ($Y=0.5$) with and without Coulomb for the two-component Skyrme liquid.	101
4.12	The proton fraction found in the low-density phase Y_{gas} as a function of the proton fraction found in the high-density phase Y_{liquid} at equilibrium for four different temperatures with Coulomb (solid line) and without Coulomb (dashed line) for the Hard-Core Skyrme Model. The dotted line marks equal concentrations in the phases. Above this line the gas phase is proton rich and below this line the gas phase is neutron rich relative to the liquid phase.	102

Acknowledgments

First and foremost, I would like to acknowledge those people who have supported me throughout this work with love, for their support has been the most cherished. I would like to acknowledge the loving support of my wife Katrina who has left friends and family behind to be with and support me. I would also like to acknowledge the devoted support of my mother and father. I extend my greatest love and gratitude to them.

Next, I would like to acknowledge those people who have supported and shared my scientific interests. In this regard, I must first acknowledge those people who have supported me during my graduate studies at Washington University in St. Louis. Professor Lee G. Sobotka, my thesis advisor, is acknowledged for his mentorship and the admirable enthusiasm he maintains for the science we all pursue. He is also acknowledged for his sincere and meticulous counseling of my progress as his graduate student which has helped me to prepare and defend my thesis in a very timely manner. Professor Robert J. Charity, my second "unofficial" advisor, is acknowledged for his mentorship and also for the specific instance when he saved the data of this thesis by insisting that a certain set of thick and non-uniform Si absorbers be removed from the experimental apparatus. He is also acknowledged for spending many days of hard work making many adjustments and additions to his statistical model code GEMINI, which have been of great benefit to this work. Professor Ronald A. Lovett is acknowledged for his mentorship in all matters theoretical. He is also acknowledged for lending a computer to aid in the formatting of this thesis. Professors Demetrios Sarantites and Robert Yaris are also acknowledged for their mentorship. All of the individuals mentioned above are acknowledged for their contributions to the open and scholarly atmosphere which exists among the nuclear and theoretical chemists at Washington University. As my formal education culminates in this thesis, I must also acknowledge those people who have helped me develop my scientific interests before, during, and after my undergraduate education. I have been fortunate to have worked with many inspiring scientists from many institutions during my education. In chronological order, I would like to acknowledge Donald Pershing from Junipero

Serra High School in San Mateo CA (retired), Professor Emeritus Ruth Yaffe from San José State University, Dr. Peter A.J. Englert director of the Institute of Geological and Nuclear Sciences Ltd. in New Zealand, Dr. Carlos Castaneda from Crocker Nuclear Lab U.C. Davis, Dr. Darrell M. Drake from Los Alamos National Laboratory, Dr. Robert C. Reedy from Los Alamos National Laboratory, Dr. Roger Byrd from Los Alamos National Laboratory, and Dr. Johannes Brückner from the Max Planck Institut für Chemie in Mainz Germany.

Finally, I would like to acknowledge those people who have taken the time to help with seemingly minor issues. These issues have remained that way due to their intervention. Omar El-Ghazzawy is acknowledged for several years of expert computer assistance. Ed Hiss is acknowledged for the use of his ability to overcome all conceivable bureaucratic obstacles. Jon Elson is acknowledged for his expert technical assistance in many engineering related aspects of this work. Margaret Amstutz is acknowledged for (but definitely not responsible for) trying to help make this thesis grammatically correct.

James Francis Dempsey

Washington University in Saint Louis
May 1997

Chapter 1

Introduction

1.1 Background

The study of collision of heavy atomic nuclei with sufficient energy to disassemble them into their constituent neutrons and protons, provides us with a way to experimentally explore the dynamics of excited, strongly-interacting systems of mesoscopic size. These systems are in the “gray regions” of theoretical expectations, being of sufficient size to invoke many-bodied complexity yet not quite large enough to enjoy statistical simplifications applicable to macroscopic systems. While the energies involved are quite high and one might expect that a semi-classical treatment of the dynamics is sufficient, the partial conversion of kinetic energy into excitation and subsequent de-excitation born out by these systems requires a quantum treatment of the dynamics. Thus, the relevant science in these intermediate-energy heavy-ion collision experiments encompasses many aspects of quantum, statistical, and many-body physics, which positions this problem at the limits of our theoretical understanding and computational capabilities. Despite the availability of sufficient kinetic energy to disassemble the entire system in these collisions, it is found that a large portion of the more dissipative collisions result in the “multifragmentation” of the system. This fascinating and unexpected reaction mechanism has captured the attention of the nuclear chemistry and physics community, while eluding a satisfactory explanation.

Multifragmentation, the copious production of fragments with mass intermediate to that characteristic of light-particle evaporation and binary fission, has become the most distinguishing feature of intermediate-energy heavy-ion reactions[1]. The

production of these intermediate-mass fragments (IMFs), often experimentally defined as fragments with $Z \geq 3$ (due to the fact that it is easier to resolve charge than mass), has been observed in the decay of nuclear systems over the full accessible range of excitation, from ground-state nuclei[2, 3] to extremely excited systems in relativistic heavy-ion collisions[4]. It is not their mere existence in the debris of intermediate-energy ($\sim 20 - 1000\text{MeV}/A$) heavy-ion collisions that stimulates our interest in these IMFs; rather, it is the observation that their copious production is not simply governed by the available phase space of an excited nuclear system at saturation density. At lower bombarding energies, the yields of IMFs are extremely small relative to the yields of evaporated light-charged particles (LCPs) and can be predicted by standard statistical-model simulations of excited compound nuclei[5]. This indicates that the fragment production is largely due to statistical emission from an equilibrated saturation-density source. As the bombarding energy reaches several tens of MeV per nucleon, the onset of multifragmentation is observed. This copious production of IMFs reaches a maximum around 100 MeV per nucleon for mid-central collisions, and the apparent onset of near complete nuclear vaporization begins to diminish IMF production for the most central collisions[6]. In this intermediate-energy regime, the assumption that fragment production is largely due to statistical emission from an equilibrated saturation-density source, of either a compound nucleus or target-size and projectile-size sources, fails to account for IMF production.

The natural question this raises is: “What does the production of these IMFs indicate?” Initial attempts to answer this question looked to the equation of state (EOS) of warm nuclear matter at subsaturation densities. Due to the hard core and short range attractive features of the nucleon-nucleon interaction, the existence of a van der Waal’s-like liquid-gas phase transition is expected to exist for nuclear matter. The existence of such a phase transition in nuclear matter has been the subject of many theoretical investigations [7-19]. Following from the expected existence of such a phase transition, numerous models based on equilibrium thermodynamics (and the expected liquid-gas coexistence region for nuclear matter) have been proposed to explain the phenomenon of multifragmentation in intermediate-energy heavy-ion collisions[20-36]. Simply put, in these models multifragmentation is imagined to result from the isentropic expansion and cooling of a hot and dense system into an instability region in the liquid-gas phase diagram where the system fractures into high-density liquid and low-density vapor regions. Thus, multifragmentation

is imagined to indicate that the nuclear system is somehow probing the instability region of the liquid-gas phase diagram of infinite nuclear matter. While it is obviously questionable as to whether or not the equilibrium expectations of bulk nuclear matter can be extrapolated to finite charged drops of nuclear matter, these models have not been proven completely irrelevant. Several years ago, a case was made that the production of IMFs indicated that the excited nuclear system had expanded to a point where clusterization became probable[37]. This argument was based on the observation that while standard statistical models were unable to produce the observed number of IMFs per LCP, a statistical model which allowed for bulk thermal expansion could reproduce the IMF to LCP ratio[38]. This description, as with all statistical models, relies on the ability of the system or some sizable piece of it to reach thermal equilibrium. The object which reaches equilibrium is assumed to be a compound nucleus-like remnant of the initial collision dynamics and a statistical decay of this nucleus is modeled according to the Weisskopf detailed-balance procedure[39] with the added (nonstandard) feature that the probabilities are influenced by the changing density of the system.

Of course, IMF and LCP multiplicity ratios are not the only observables one can extract from these collisions. For example, the emission patterns of LCPs in velocity space, produced in heavy-ion collisions at intermediate energies, have demonstrated that a binary reaction mechanism exists for most of the reaction cross section[40]. In such a picture a projectile-like fragment (PLF) and a target-like fragment (TLF) and perhaps a center-of-mass or interaction-region fragment are formed during the collision for most of the reaction cross section. If one insists on retaining a statistical-emission picture like the one described above, the decay characteristics of all of these sources are necessary in principle to properly describe the observed number of IMFs and LCPs. Simply reproducing the IMF yields by considering a single source of low-density matter while ignoring other observables may miss the relevant physics. More recently, a study of IMF-PLF angular correlations has provided evidence that IMF production can be understood as a dynamic multiple neck rupture[41, 42] or proximity fission[43], akin to what is believed to occur with low probability in low-energy fission[44]. In this scenario the production of IMFs is attributed to a dynamic instability in a neck-like structure formed between the PLF and TLF, and the yield of fragments need not reflect any equilibrated statistical

distribution. This multiple neck-rupture argument, while it has been extensively developed for the case of low-energy fission[45], has been presented only heuristically in its application to intermediate-energy heavy-ion collisions, presumably due to the increased complexity of the problem. This mechanism for IMF production is obviously much more complicated due to the number of degrees of freedom which must be considered. At a minimum, one might guess that the single-particle phase-space distribution must be evolved in time in order to search theoretically for any evidence of this mechanism. Such simulations have been performed in the framework of the Boltzmann-Uehling-Uhlenbeck (BUU) transport equation and “neck” fragments have been observed[46, 47] in some cases, but the description is qualitative at best (see figure 1.1). These BUU simulations are presently considered to be the “state-of-the-art” in intermediate-energy dynamic-reaction models, and the fact that they display neck-forming scenarios is intriguing, but more sophisticated approaches are obviously necessary. Unfortunately, a theoretical (or more correctly, computational) breakthrough to provide a model that can decide the issue may take some time. In any case, the more complete our experimental observations of these heavy-ion collisions become, the greater our ability to understand the mechanism(s) responsible for the phenomenon of multifragmentation.

It is useful at this point to consider the similarities and differences which exist between the statistical and the dynamical multifragmentation scenarios. The common ingredients among these scenarios are that the probability of observing IMFs depends on the energetics of producing subsaturation (low-density) nuclear matter and the probability that the excited (primary) IMFs produced survive sequential-decay processes and retain their IMF status ($Z \geq 3$). Two significant differences exist between these scenarios: the dimensionality of the expansion(s) involved; and the requirement of the thermalization of the available energy. For the statistical description to be valid, the available energy must be thermalized among the various degrees of freedom in the system, while the dynamic description need only excite a few pertinent modes in the system. Analogously, the expansion involved in the statistical description above is a bulk thermal expansion and in the neck-rupture description the expansion is localized. A third and perhaps not so obvious difference between these models is that the dynamic multiple neck rupture scenario allows for fragments to be produced from material which is “surface-like” and thus possibly quite neutron rich compared to the bulk matter. A growing body of experimental evidence suggests

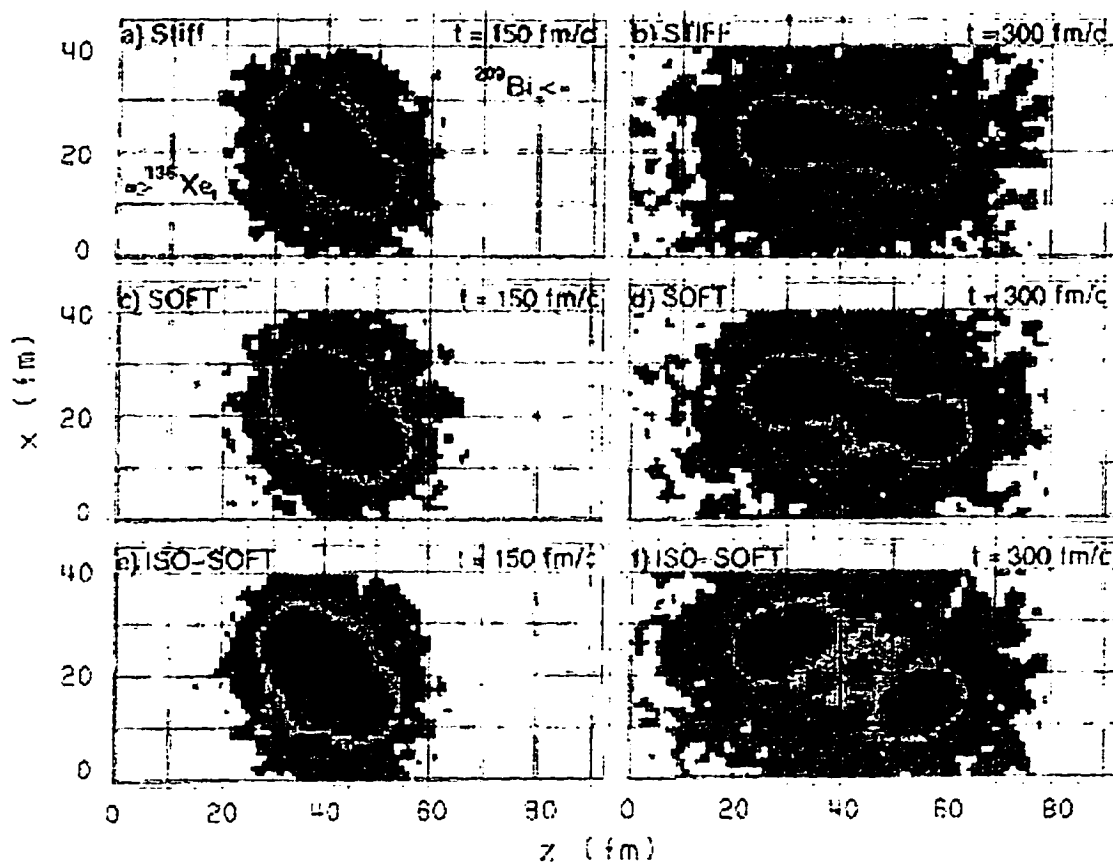


Figure 1.1: Density distributions projected on the reaction plane which result from BUU simulations of $^{136}\text{Xe} + ^{209}\text{Bi}$ collisions at 28 MeV/nucleon for three different equations of state. Notice that a PLF and TLF fragments are connected by a “neck”-like structure extended between them and that a neck fragment appears to have been formed in the lower right panel.

that these neutron skins, regions in the tail of the nuclear-matter density distribution where the ratio of neutron density to proton density is much greater than in the bulk may exist[48, 49]. Recently, Hartree-Fock calculations of light spherical nuclei have shown good agreement with these data[50]. If these skins do indeed exist, then the material of a neck region produced in a heavy-ion collision has the possibility of being extremely neutron rich due to its extended surface. Of course, the feasibility of such matter being produced in the time scale of a heavy-ion collisions must be born out by dynamical simulations.

In summary, the mechanism responsible for the phenomenon of multifragmentation in intermediate-energy heavy-ion collisions is still unknown. It has been found that the consideration of equilibrated low-density nuclear matter comes tantalizingly close to explaining the phenomenon, but proves inconsistent when a more complete experimental picture of the collision reaction mechanism is assembled. More recently proposed dynamic mechanisms that are more consistent with the experimental observations are considerably more complex and apparently beyond the scope of present theoretical reaction models. To move beyond this impasse even more descriptive experimental data are required to search for a set of observables that can further distinguish between these proposed scenarios.

1.2 Experimental Objective

The objective of this study was to differentiate between the scenarios given above for the phenomenon of multifragmentation. To this end, the influence of entrance-channel N/Z (neutron-to-proton ratio) on the multiplicity of IMFs produced, as well as the nature of the N/Z of the IMFs themselves was explored. The logic was that by influencing the N/Z of the projectile and target (changing N/Z by as much as 10%) the nature of the surface matter in the different systems might be influenced, possibly affecting the production of the IMFs. Furthermore, the observation of the N/Z of the IMFs produced was performed with the hope of better defining their characteristics and possibly uncovering a clue to their origin.

Definite progress toward realizing this objective was made by this study, although the influence of entrance-channel N/Z on the multiplicity of IMFs was found to be minor and in agreement with what would be expected from standard statistical-model simulations. It was found that the N/Z of LCPs and IMFs produced in all of

the collisions studied have a unique N/Z signature (neutron rich) in the mid-velocity region. This new observable provides a promising means to discern the relevance of models based on the framework of a liquid-gas phase transition in nuclear matter. This study also confirms the results of several other studies which have previously reported evidence for a neck-fragmentation mechanism[41, 42, 40].

1.3 Theoretical Objective

The observed neutron richness of LCPs and IMFs produced in the mid-velocity region of the collision gave rise to the question of what the equilibrium expectation is for the N/Z of different density phases in the phase-coexistence region of asymmetric nuclear matter. The theoretical objective of this study was then to attempt to understand the behavior of the N/Z degree of freedom at equilibrium in nuclear matter. While many previous studies of nuclear matter have considered the N/Z degree of freedom, all models known to this author which consider multifragmentation in the framework of a liquid-gas phase transition have completely ignored or artificially constrained the N/Z degree of freedom. A few studies have recently pointed out the importance of including this degrees of freedom when considering heavy-ion multifragmentation (heavy ions are, of course, asymmetric)[18, 19], but have not included Coulomb and finite-size effects in their considerations. In an effort to include the effect of finite-Coulomb interactions, the more important of these effects when considering N/Z observables, two simple models were developed which explore the influence of finite-Coulomb interactions on the N/Z of the different density phases in the coexistence region.

This objective was met only in part, but a promising new direction for study of multifragmentation both experimentally and theoretically has been identified. The results of these models demonstrate that at equilibrium a fractionation of neutron and proton concentrations among the different phases is expected at all but one value of asymmetry (an azeotrope) and that this result is strongly influenced by finite-Coulomb interactions. Comparison of the equilibrium N/Z expectations (from a more sophisticated model that can properly treat microscopic or mesoscopic cluster formation) with isotopically-resolved IMF yields may eventually provide a means to establish the relevance, or lack of relevance, of a liquid-gas phase transition in nuclear matter to the phenomenon of multifragmentation.

Chapter 2

Experimental Aspects

2.1 Experimental Layout

The experiment was performed at the National Superconducting Cyclotron Laboratory at Michigan State University. The accelerator provided beams of ^{136}Xe and ^{124}Xe at 55.0 MeV/A with a flux of 7.3×10^7 particles per second. The four reactions, $^{124,136}\text{Xe} + ^{112,124}\text{Sn}$ were studied using an experimental apparatus which is highly efficient for the detection of both charged particles and neutrons. Some of the relevant numbers for these systems, and the abbreviations used throughout this work are found in table 2.1. Figure 2.1 shows a schematic of the experimental layout. Detection of charged particles at the most forward angles, 2.2° to 4.5° , was provided by the Forward Array (FA), a highly-segmented annular silicon-strip detector backed by 16, 2-cm thick CsI(Tl) detectors. The FA provided unit-charge resolution for fragments with $3 \leq Z \leq 55$ (Z =atomic number) as well as excellent angular-position information. Detection of charged particles from 5.4° to 160.0° was provided by the Washington University/Michigan State University MINIWALL/MINIBALL multi-detector array. These devices identified elements with $Z \leq 10$ and through varying angular regions, isotopes for $Z \leq 4$. Neutron detection was provided by the University of Rochester SUPERBALL neutron-multiplicity meter. The Forward Array was constructed specifically for this experiment, while the MINIWALL/MINIBALL multi detector array and the University of Rochester SUPERBALL neutron multiplicity meter were existing devices available for use in approved experiments at the National Superconducting Cyclotron Laboratory at Michigan State University.

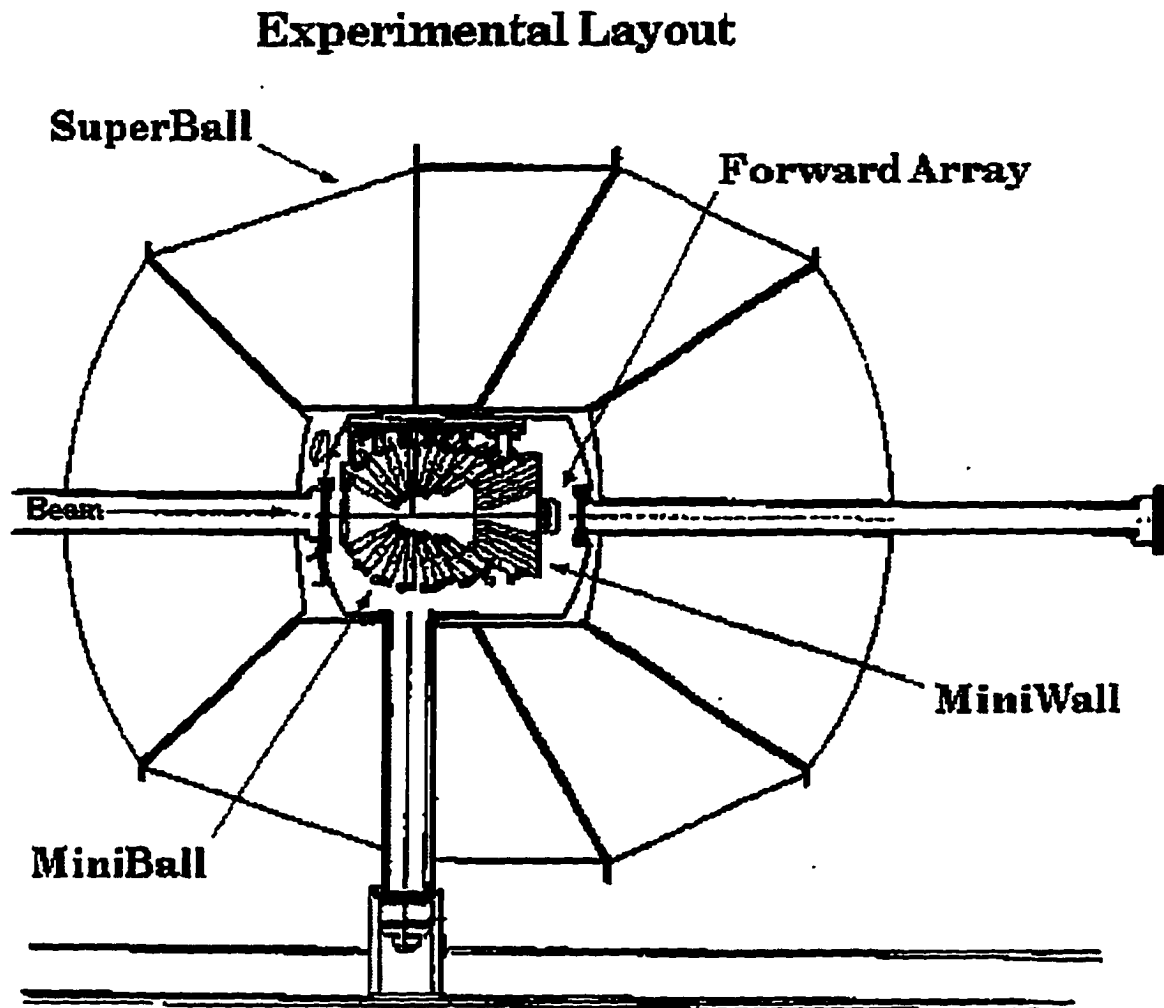


Figure 2.1: A layout of the experimental setup is shown. The devices described in the following section are labeled. The beam which enters from the left of the figure, is approximately 1.8 meters from the floor. A computer-controlled target ladder assembly, not shown, was used to select the target.

Table 2.1: 55 MeV*A $^{124,136}\text{Xe} + ^{112,124}\text{Sn}$

Label	System	N/Z			E_{cm} MeV	E_{cm}/A MeV	V_{cm} cm/ns
		projectile	target	total			
LL	$^{124}\text{Xe} + ^{112}\text{Sn}$	1.30	1.24	1.27	3237	13.72	5.42
LH	$^{124}\text{Xe} + ^{124}\text{Sn}$	1.30	1.48	1.38	3410	13.75	5.15
HL	$^{136}\text{Xe} + ^{112}\text{Sn}$	1.52	1.24	1.38	3378	13.62	5.65
HH	$^{136}\text{Xe} + ^{124}\text{Sn}$	1.52	1.48	1.50	3567	13.72	5.39

2.2 The Forward Array

2.2.1 Principle of Operation

The Forward Array (FA) is a highly-segmented charged-particle $E - \Delta E$ telescope detector array. The first element of the telescope (ΔE) consists of a $280 \mu\text{m}$ ($67.05 \frac{\text{mg}}{\text{cm}^2}$) thick annular silicon-strip detector cut from a single 10.16 cm diameter silicon wafer[51]. It was positioned such that it subtended angles from 2.2° to 4.5° in the lab. A photograph of the front and back of the device is displayed in figure 2.2. The back face of the detector (n-type side, facing downstream) is segmented into 16 azimuthal pie slices, while the front face is divided into quadrants, each subdivided into 16, 2.5 mm wide, polar-arc strips. The diode detector is reversed biased, and each strip or pie slice is read out independently. The second element of the telescope (E) is composed of 16, 2-cm thick, CsI(Tl) scintillators optically coupled to PIN silicon photodiodes via 2-cm thick UV-transmitting lucite light guides. These scintillators were geometrically similar to the azimuthal pie slices of the first element. The 16 azimuthal pie slices of the first element and the 16 two cm thick CsI(Tl) scintillators of the second element were aligned so that the device essentially acted as 16 independent telescopes. Each of these telescopes also provided polar-angle information as well, from the signal of the 64 polar-arc strips. A thin $5.0 \frac{\text{mg}}{\text{cm}^2}$ Sn-Pb (60% Sn, 40% Pb) foil was placed in front of the array to absorb electrons and x-rays emitted from the target. A schematic of a single telescope element of the FA is shown in figure 2.3.

An $E - \Delta E$ telescope, such as the FA, identifies the charge of an ion with the following simple principle. If a charged particle impinging on the first element has sufficient kinetic energy to pass through it (the silicon element) but not so much as

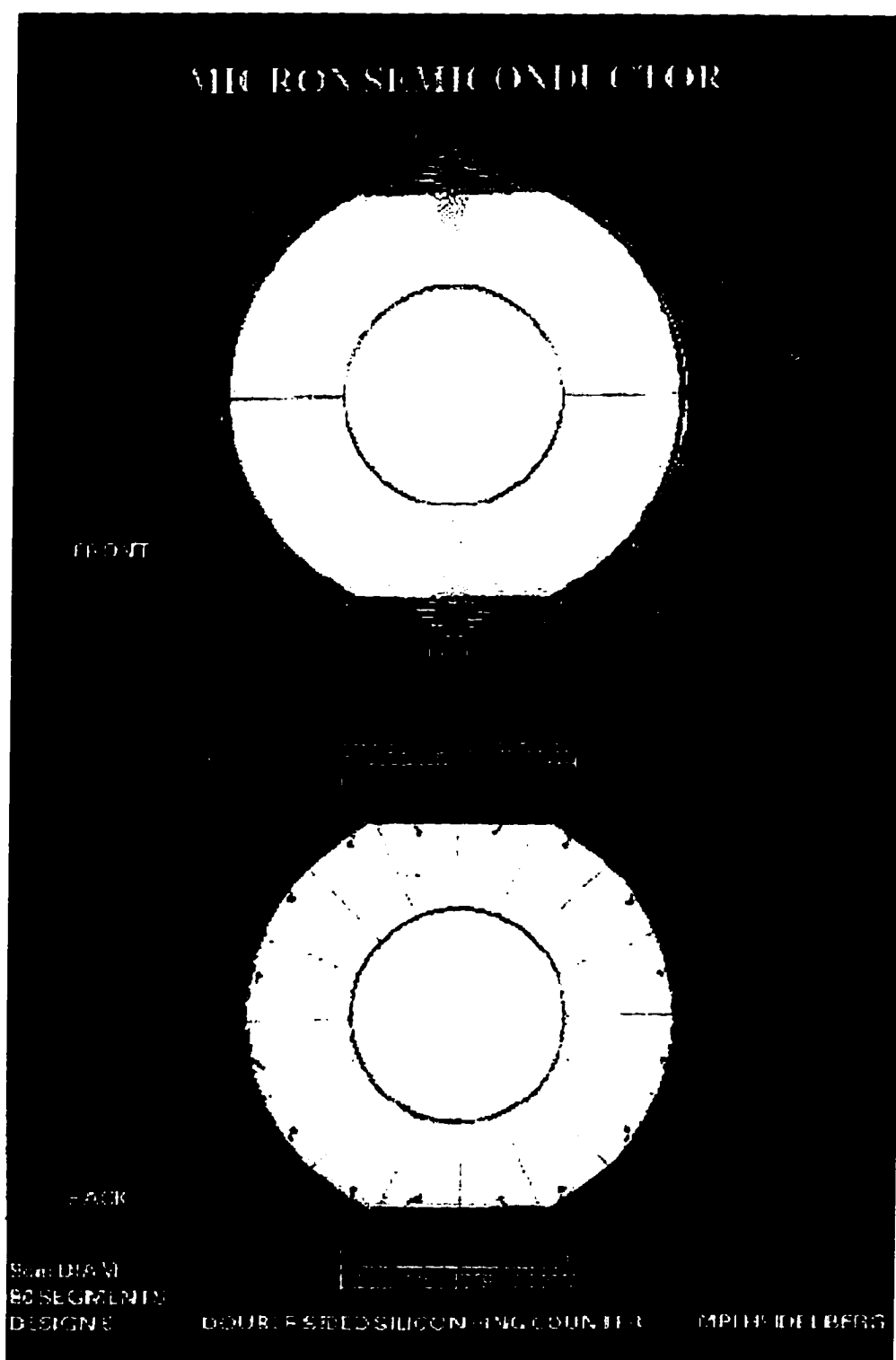


Figure 2.2: A Photograph of the front and back sides of the $280 \mu\text{m}$ ($67.05 \frac{\text{mg}}{\text{cm}^2}$) thick annular silicon strip detector used as the first element of the Forward Array.

Forward Array Schematic

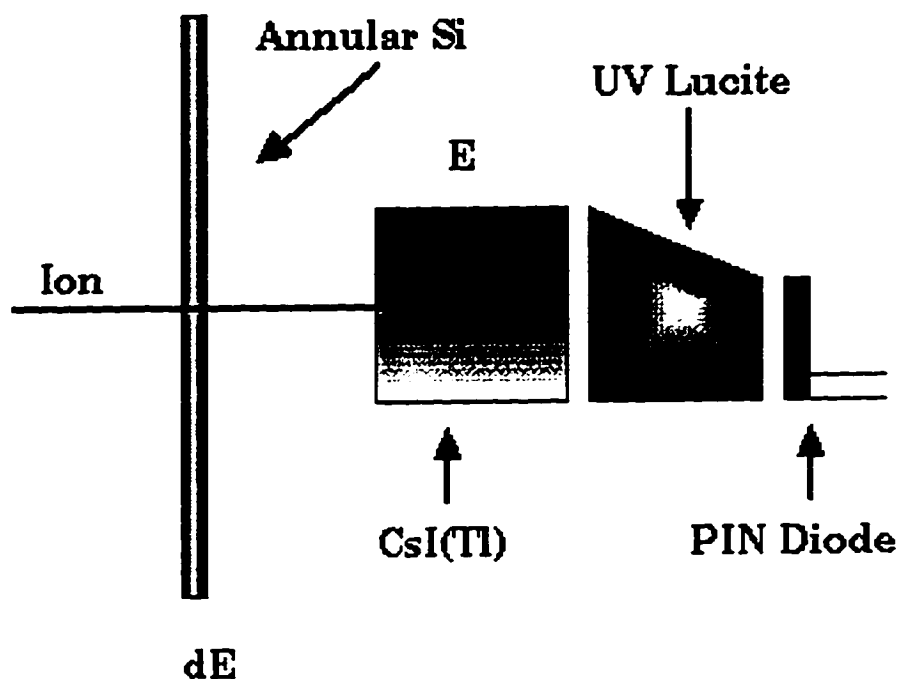


Figure 2.3: A schematic of a single element of the forward array is displayed. A ΔE signal is produced by charge collection in a pie-sector of the annular-silicon first element. An E signal is then produced in the corresponding CsI(Tl) crystal as luminescence which is collected via a light-pipe and converted to charge in the PIN diode. The CsI(Tl) crystal and light-pipe are wrapped in reflecting aluminized mylar to increase light collection.

to punch through the second element (the CsI(Tl) element), then a particle- Z identification is possible. For particles with energies above a few $\frac{\text{MeV}}{A}$ the approximation $dE/dx \simeq kAZ^2/E$ is valid, where dE/dx is the energy loss dE in a thickness dx , k is a proportionality constant, Z is the atomic number of the particle, and A is the mass of the particle. One can easily see that for a given dx , if A varies slowly with Z , then a plot of E verses dE will yield a family of contours $dE \propto 1/E$ offset by the integer values of Z . Figure 2.4 is a plot of the digitized pulse height of the light output from the second FA telescope element verses the digitized pulse height of the charge deposited in the first FA telescope element, calibrated to yield deposited energy in MeV. As the light output from the second element is roughly proportional to the total energy of the particle, E , (if little energy was deposited in the first element, a condition satisfied by most of the particles detected in the FA during this experiment) and the charge collected in the first element is roughly proportional to the energy loss dE in a thin absorber of thickness dx , we see the expected contours of $dE \propto 1/E$, offset for each chemical element by the integer values of the atomic number, Z . Thus the Forward array provides particle- Z identification for fragments with $3 \geq Z \geq 55$. The energies of these fragments are resolved to better than 3% for fragments with $6 \geq Z \geq 54$ (see calibration section below), and an angular resolution of the direction of emission of 0.21° in polar angle θ and 11.5° in azimuthal angle ϕ is provided by the segmentation of the Si detector.

2.2.2 Electronics

The electronics used to read out the 16 channels of the azimuthal pie-slice segments and the 64 channels of the polar-arc segments are similar, differing only in the mode of signal digitization for the various elements. A schematic of the electronics is found in figure 2.5. The preamplifiers used for all 96 individual channels of the first element of Forward Array (80 Si and 16 CsI(Tl)) were developed by Jon Elson, Lee Sobotka, and James Dempsey at Washington University, by adapting an amplifier designed by Michael Maier[52]. The 16 azimuthal pie sectors of the first element and the 16 PIN photodiodes of the second element of the FA were then amplified in a second stage slow-shaping amplifier and a fast timing-filter amplifier. The outputs of the fast amplifiers were sent to discriminator logic modules to produce logic signals for timing, gate generation, and trigger logic circuits. The outputs of the slow-shaping

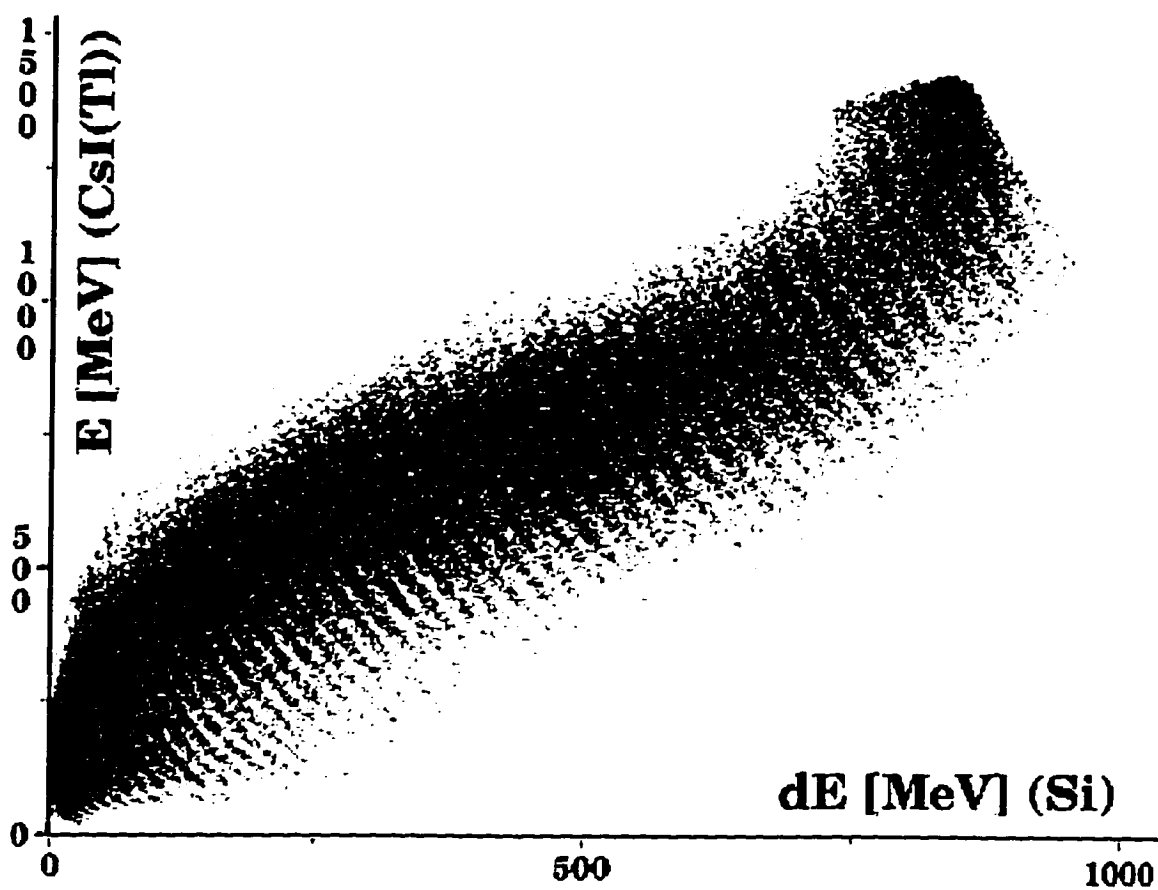


Figure 2.4: A two dimensional histogram of the calibrated output of the Forward Array is plotted such that the first element output (ΔE) is on the x-axis and the the second element output (E) is on the y-axis.

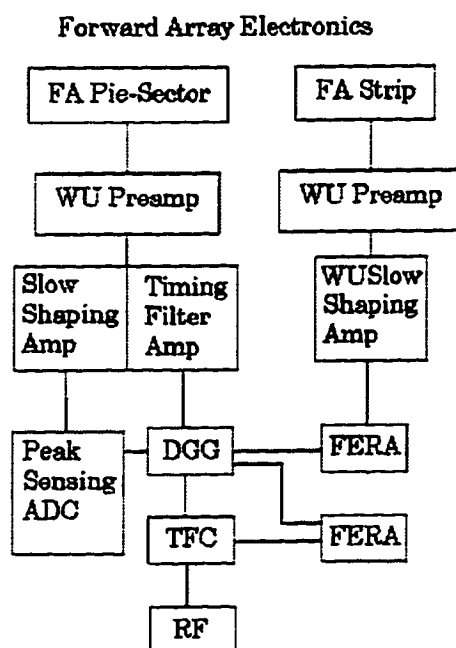


Figure 2.5: A block diagram describing the electronics used to read out the elements of the Forward Array.

Table 2.2: Ions Used in Calibration of Forward Array

Ion	E/A MeV/A	Ion	E/A MeV/A
^{136}Xe	55.0	^{60}Ni	22.0,40.1
^{84}Kr	22.0,40.1	^{56}Fe	22.0,40.1
^{80}Kr	22.0,40.1	^{52}Cr	22.0,40.1
^{68}Zn	22.0,40.1	^{18}O	22.0,40.1
^{64}Zn	22.0,40.1	^{12}C	22.0

amplifier were sent to 4V 4096-channel peak-sensing ADCs, where the pulse heights of the signals were digitized if the fast signal fired their discriminators. The 64 polar-arc segment strips were also amplified in a second stage with 4 computer-controlled 16-channel slow-shaping amplifiers that were developed at Washington University by Jon Elson and Lee Sobotka by adapting an amplifier designed by Michael Maier[53]. The outputs of these slow amplifiers were all digitized by a charge-integrating FERAs (Fast Readout and Encoding QDC) if any pie-sector fast signal fired a discriminator. Of these 64 arc segments, only those with a signal above the integration pedestal (integrated DC offset) were read out by the acquisition software. Times of the 16 pie-slice segments relative to the radio frequency (RF) of the cyclotron were digitized in a time-to-charge converter suitable for integration with a FERA (Time-to-FERA converter).

2.2.3 Calibration

The FA was calibrated with elastically-scattered beams of one or two of the following ions: ^{136}Xe , ^{84}Kr , ^{80}Kr , ^{68}Zn , ^{64}Zn , ^{60}Ni , ^{56}Fe , ^{52}Cr , ^{18}O , and ^{12}C (see table 2.2). The beam energies were corrected for energy losses in the target (thin targets of Bi or Ta), the Sn-Pb foil in front of the FA, and the annular silicon-strip ΔE detector (when considering the second element). The response of the annular silicon-strip ΔE detector was found to be a highly linear function of the energy deposited. A linear energy calibration of the 16-pie sector segments was good to better than 3%. Three of the ions used to calibrate this detector were of low enough energy such that they were stopped in the silicon, providing absolute calibration points. The CsI(Tl) light output of the second element is known to be highly non-linear and Z-dependent[54].

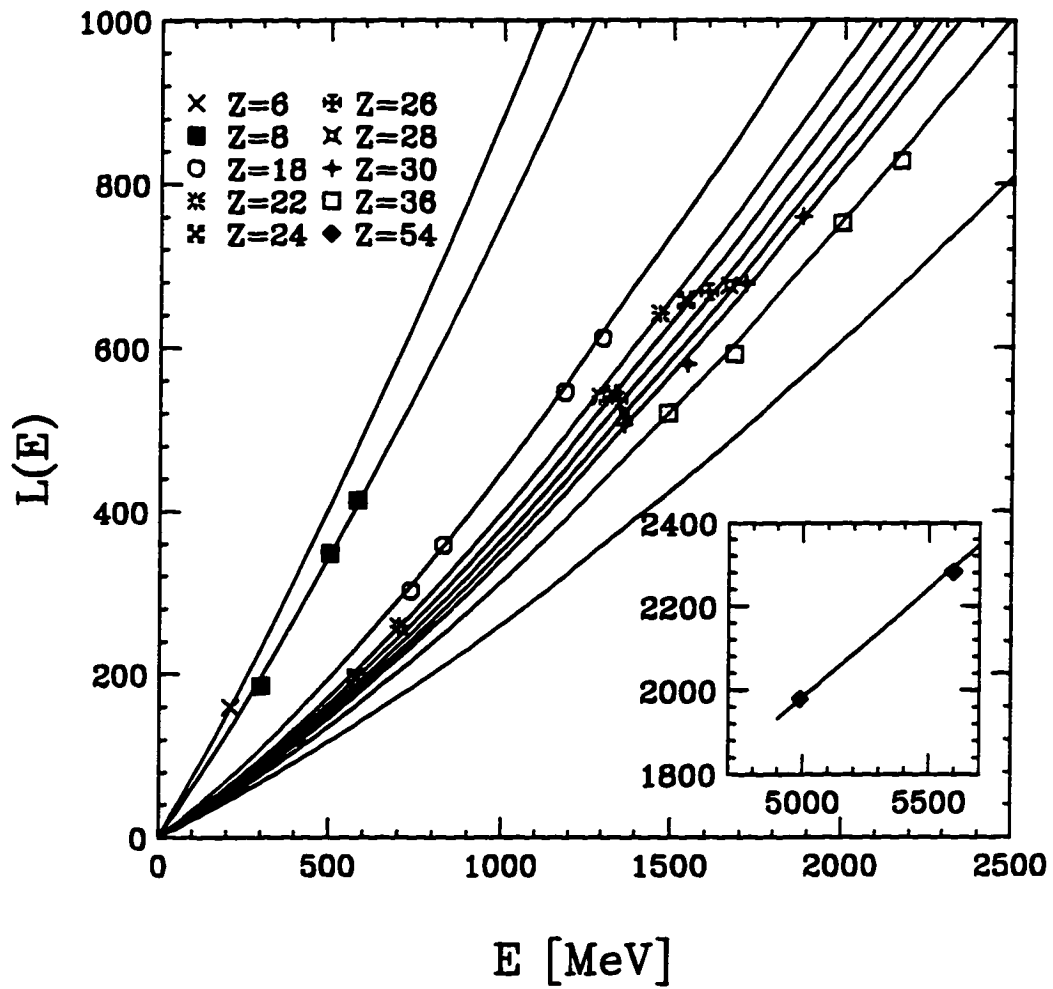


Figure 2.6: Fitted energy-calibration points for ions which traversed the pie-sector of the first element and stopped in the corresponding second element of the Forward Array.

A Z-dependent calibration was achieved by fitting the light output as a function of particle Z and energy E, $L(Z, E)$ with the nine parameter function given by

$$L(Z, E) = \gamma E + \beta(e^{\alpha E} - 1) \quad (2.1)$$

where

$$\gamma = \gamma_1 + \gamma_2 e^{\gamma_3 Z} \quad (2.2)$$

$$\beta = \beta_1 + \beta_2 e^{\beta_3 Z} \quad (2.3)$$

$$\alpha = \alpha_1 + \alpha_2 e^{\alpha_3 Z} \quad (2.4)$$

define the nine free parameters. The fits were performed with a code which utilized the Levenberg-Marquardt minimization technique (a variant of Newton's method) for fitting a model with non-linear coefficients[55]. This parameterization yielded an excellent fit to the data for all 16 elements of the FA, producing an energy calibration good to better than 3% for $6 \leq Z \leq 54$ (see figure 2.6).

2.3 The MINIWALL/BALL Array

2.3.1 Principle of Operation

The MINIWALL/BALL Array is a charged-particle detector array that subtends approximately 85% of the 4π solid angle from the target, with detectors at polar angles ranging from 5.4° to 160.0° in the laboratory. All of the 284 MINIWALL/BALL Array detectors consist of a thin fast plastic ($4 \frac{mg}{cm^2}$ for the BALL and $8 \frac{mg}{cm^2}$ for the WALL) and a thick CsI(Tl) (3 cm for the WALL 5.4° to 28.0° , 2 cm for the BALL 28.0° to 160.0°) phoswich scintillation detector read out by a single photomultiplier tube (PMT). This phoswich assembly is schematically displayed in figure 2.7. Schematic diagrams of the MINIWALL and MINIBALL are shown in figures 2.8 and 2.9 respectively. The detectors afford particle identification via the two pulse-integration techniques outlined below.

There are three distinct time components of the visible light output of these detectors. The fastest component, a rapidly rising and decaying "spike" with a decay time constant on the order of nanoseconds, results from energy deposited in the thin fast-plastic scintillator. Integration of the charge produced in this region of the pulse

MINIWALL/BALL DETECTOR PHOSWICH

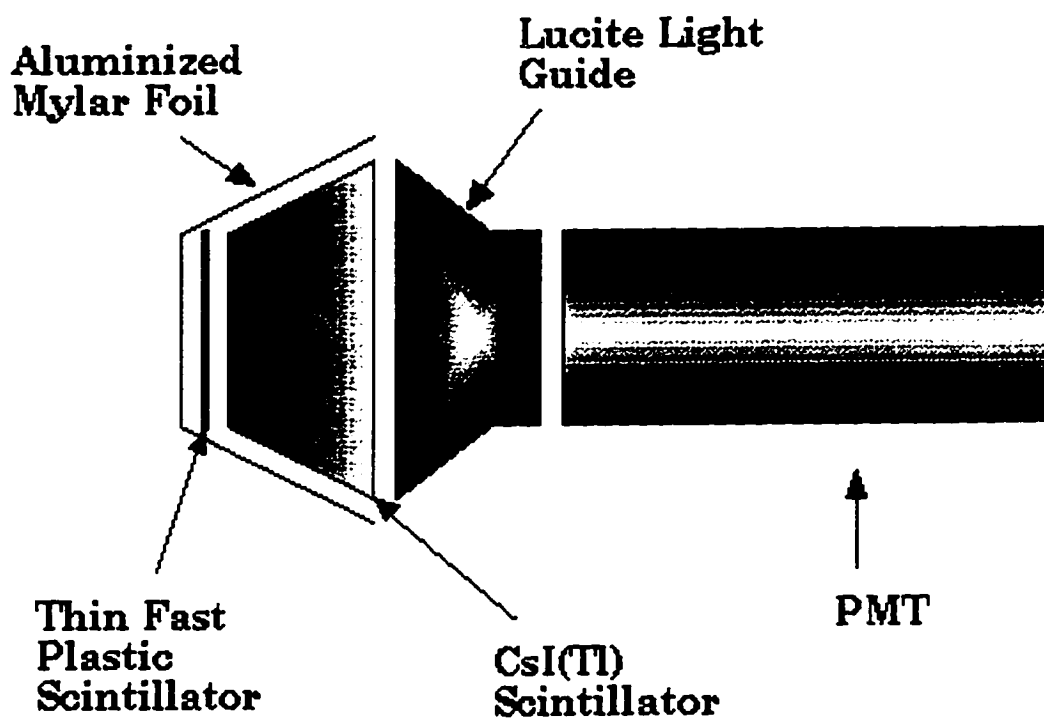


Figure 2.7: A schematic of the elements of the MINIWALL/BALL detectors.

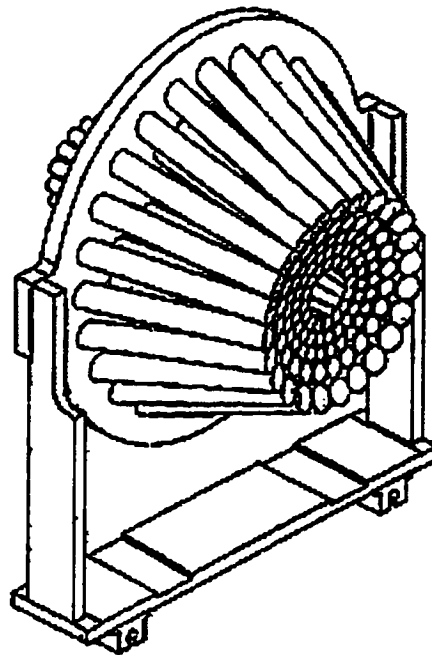
(FAST signal) yields a quantity proportional to the energy loss dE in a thin absorber of thickness dx (the fast plastic), similar in principle to the signal produced in the first element of the FA. The two remaining time components result from the CsI(Tl) scintillator, having similar rise times on the order of 100 ns and differing decay times. Of these two components, one is characteristic of the stopping power of the ion that traverses the crystal with a decay time ranging from 0.4 μ s to 0.7 μ s, while the other is independent of particle type with a decay constant of ~ 7 μ s[56]. Integration of a region about the peak of these slower components (SLOW signal) of the signal yields a quantity proportional to the energy E of the particle, while integration of a region of the exponentially-decaying tail of the light output (TAIL signal) yields a quantity which depends strongly on the Z and A of the particle for lighter ions [57].

With these three integrated regions two particle-identification techniques are possible (see figure 2.13). The first particle-identification technique is provided by plotting the integrated FAST signal versus the integrated SLOW signal and this is shown in figure 2.10. The observed contours allow for particle- Z identification along contour ridges; however, non-linearities in the scintillation light output show a dependence other than the expected contours of $dE \propto 1/E$ (FAST $\propto 1/\text{SLOW}$, notice that the E and ΔE axes are reversed compared to figure 2.4). The second particle-identification technique is provided by plotting the TAIL signal versus the SLOW signal, as shown in figure 2.11. In this case, isotopic particle identification is possible for particles with $Z \leq 4$. Successful integration of all of these regions relies on the ability to produce logic signals to gate the integration time windows which are sufficiently stable relative to the signal being integrated. Unfortunately, in this experiment, for reasons not completely understood, such a stability was not achieved for all detectors. Comparison of figure 2.11 with figure 2.12 will give the reader a feel for the range of particle-identification resolution. This instability mainly resulted in the loss of isotopic resolution in a large fraction of the detectors.

2.3.2 Electronics

The logic diagram for the electronics used to read out the 172 detectors of the MINIBALL (for a bank of 16 detectors) is shown in figure 2.14. The electronics used to read out the 112 detectors of the MINIWALL are quite similar. The difference between the systems lies in where and when the signals are amplified and split for integration.

MINIWALL ARRAY



Scale: 1-6

8-18-68
JTHood

Mated to MINIBALL

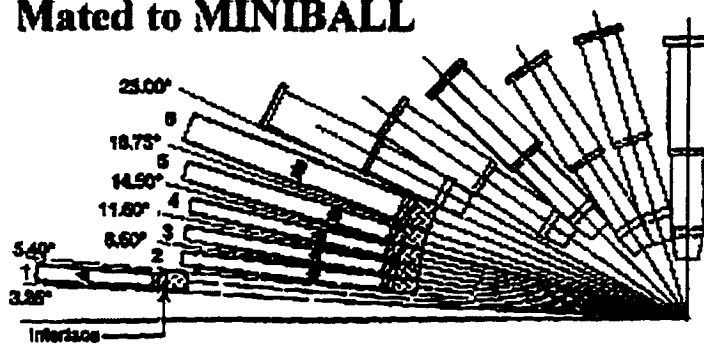


Figure 2.8: A schematic of the MINIWALL detector array.

MINIBALL ARRAY

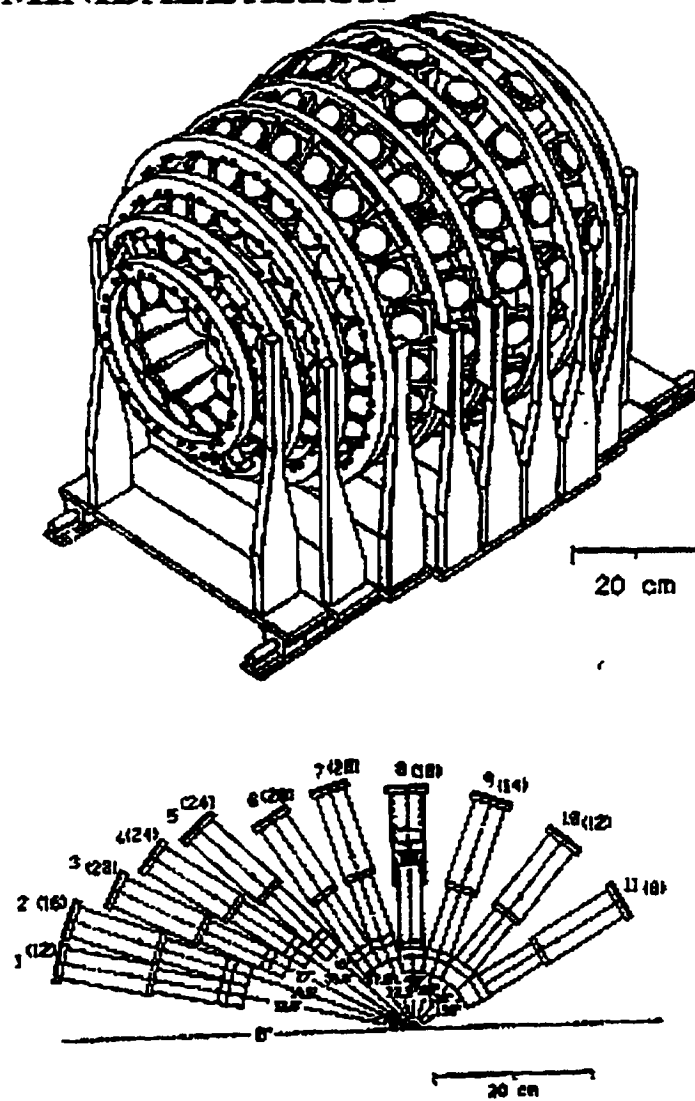


Figure 2.9: A schematic of the MINIBALL detector array.

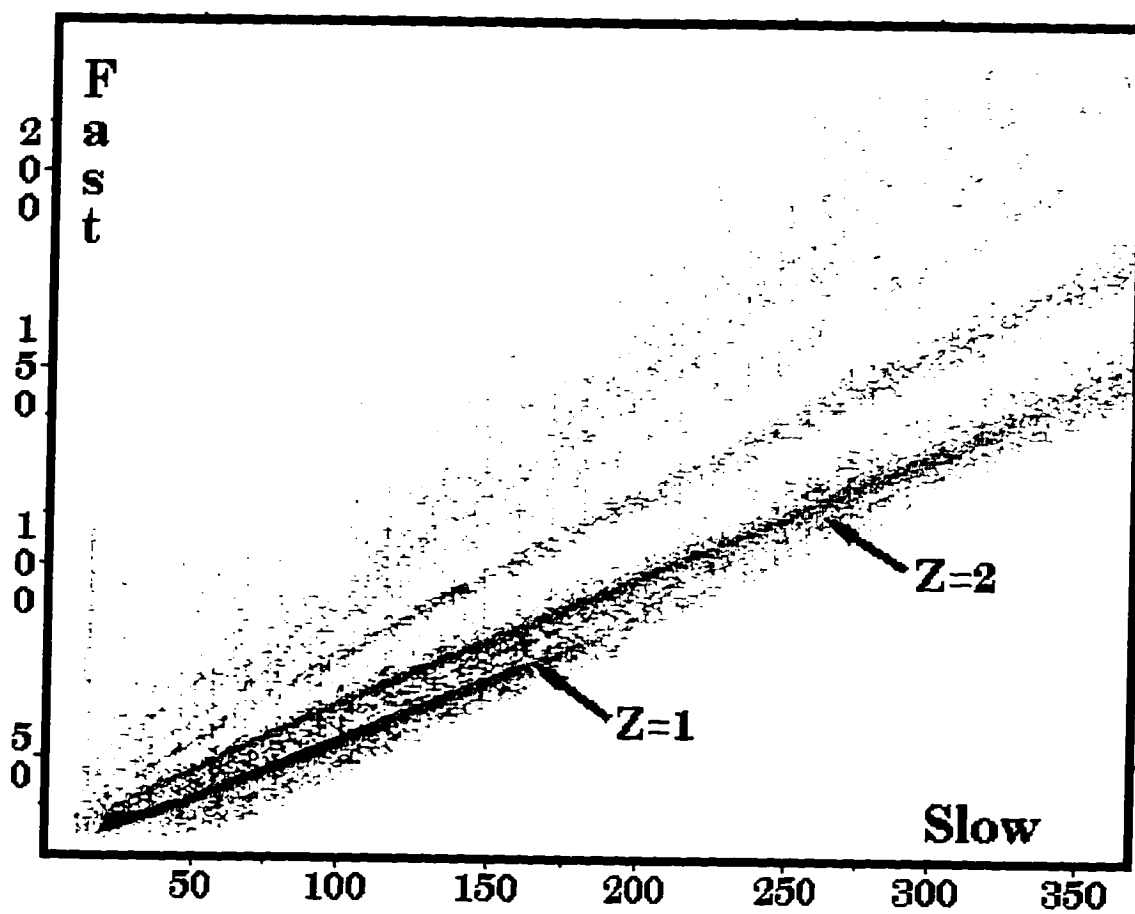


Figure 2.10: A two dimensional histogram of the digitized FAST and SLOW regions from a MINIWALL detector with poor resolution.

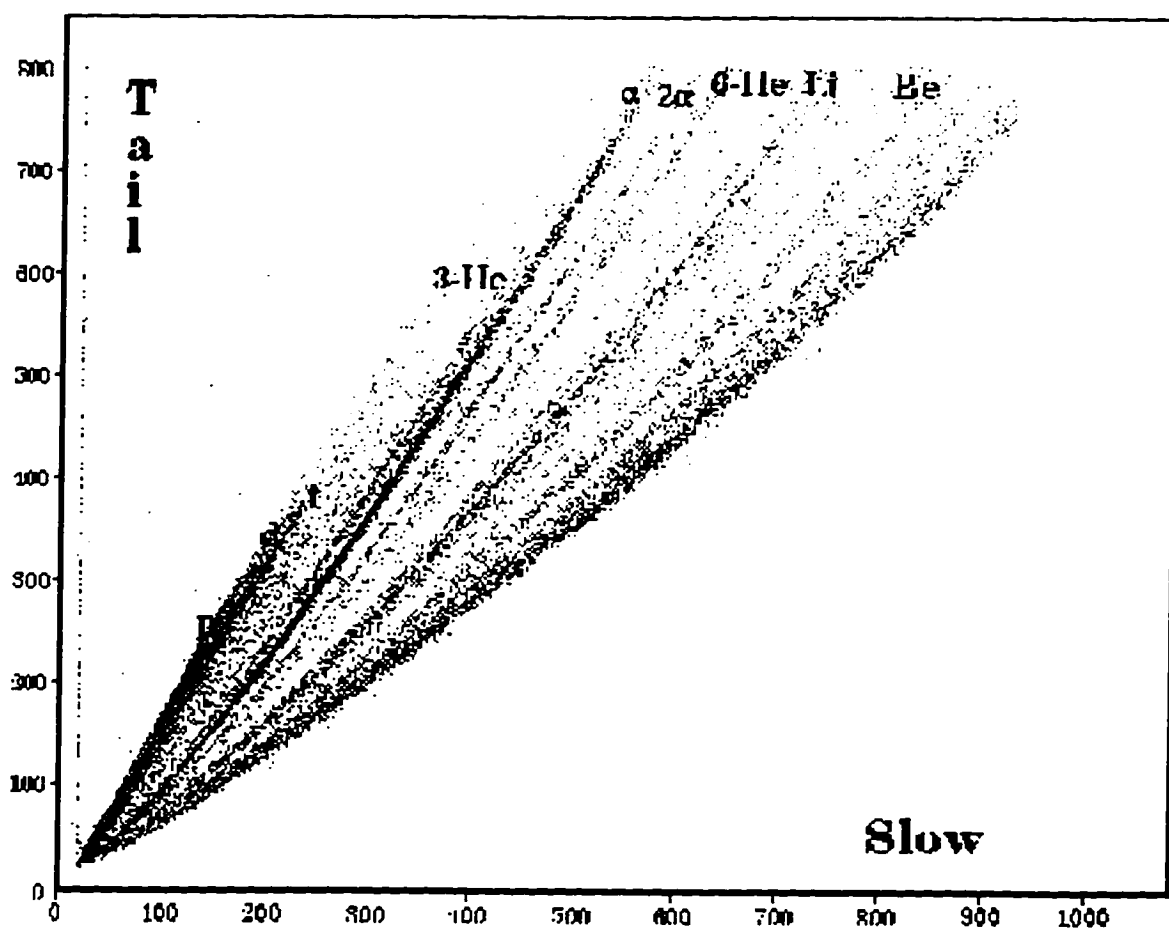


Figure 2.11: A two dimensional histogram of the digitized TAIL and SLOW regions from a MINIWALL detector with proper resolution.

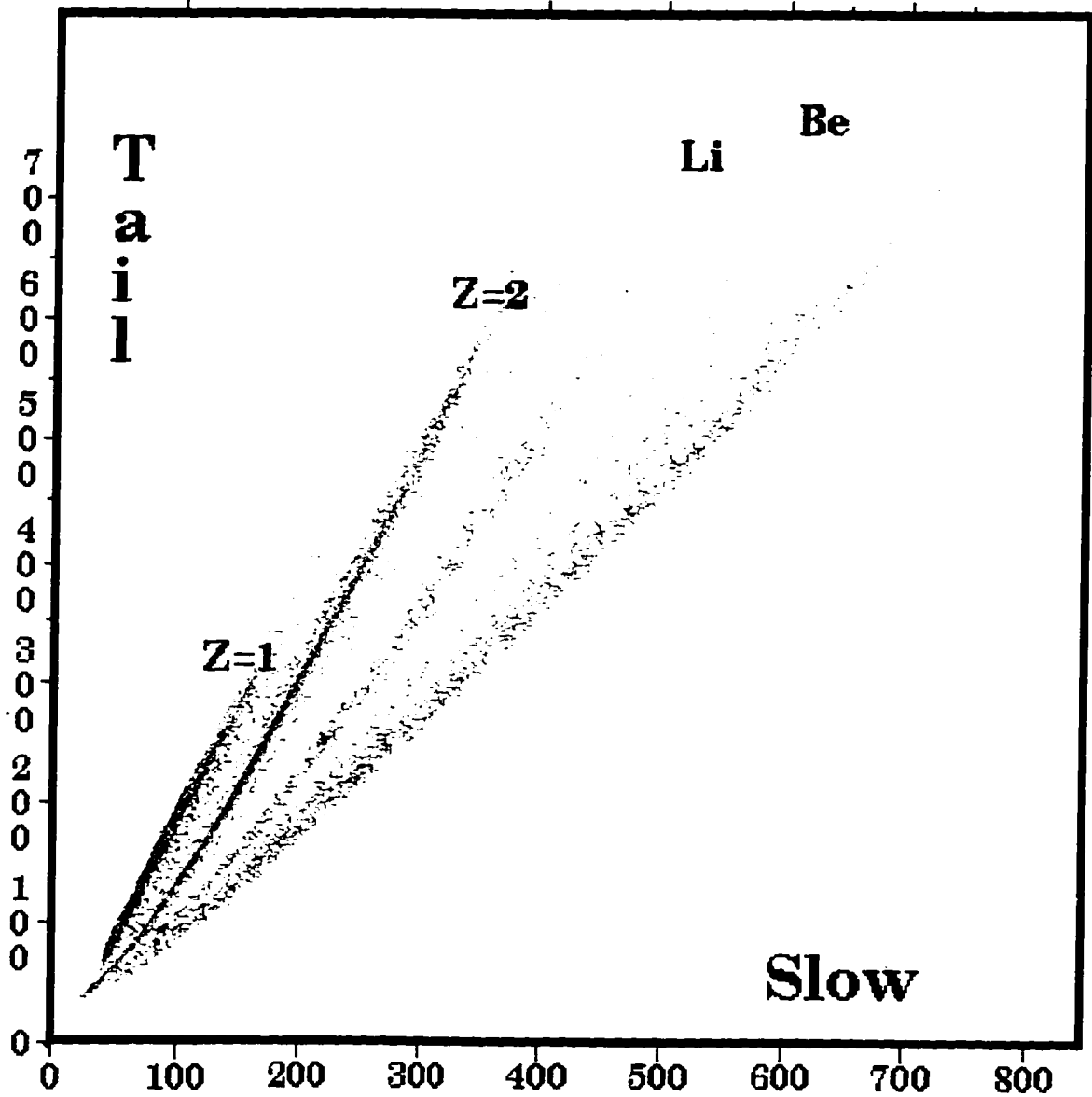


Figure 2.12: A two dimensional histogram of the digitized TAIL and SLOW regions from a MINIWALL detector with poor resolution. The loss of p.d.t resolution is evident.

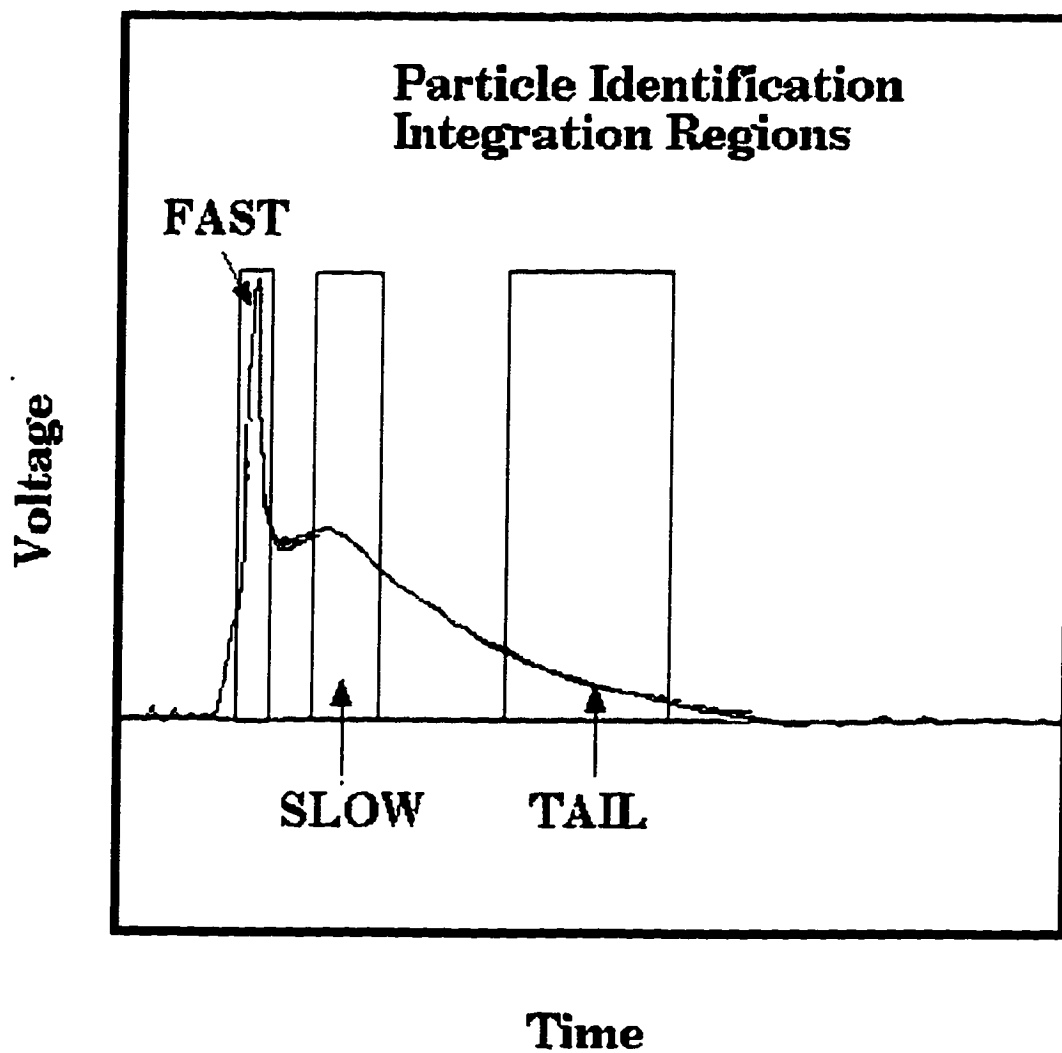


Figure 2.13: A schematic of the charge-integration regions used to perform particle identification on the response of the MINIWALL/BALL detectors

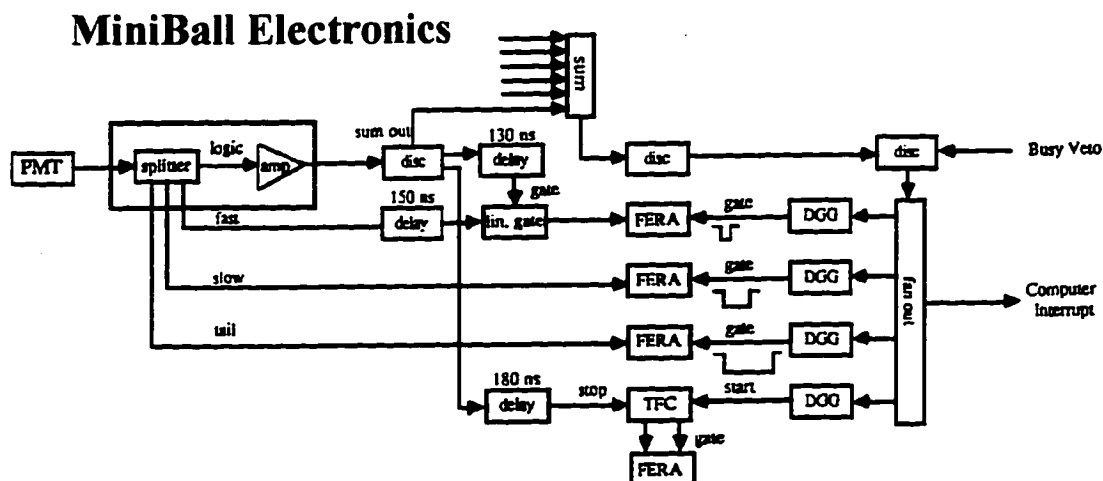


Figure 2.14: A block-diagram schematic of the electronics used to read out the MINI-BALL detectors. The electronics used to read out the MINIWALL detectors are the same in principle, with minor differences. Taken from R.T. deSouza et al.[59].

Both systems split the linear signal four ways to produce one signal for discriminating in the logic circuit and the other three signals for integration. Individual gates are produced for integrating the FAST region of the signal, while gates for integrating the TAIL and SLOW regions are produced for each bank of 16 detectors. The gates produced by each detector bank use the fastest detector in the array, from a logical OR of the signals, to generate the gate. This ensures that, of the detectors which are hit, the detector defining the time position of the gates has the largest signal and minimal time walk. The gates are generated and positioned by delay and gate generator (DGG) circuits. Time-to-FERA converters then convert time intervals between logical gates into charge outputs that are used in common-start individual-stop mode and integrated with FERA modules. Times of the fastest detector relative to the radio frequency (RF) of the cyclotron were also digitized in a time-to-digital converter (TDC). A linear sum of logical signals from the detectors was used as a multiplicity trigger (see Trigger Logic section below).

2.3.3 Calibration

A minimal set of calibration data for the MINIWALL/BALL was collected using elastic scattering of a 22.04 MeV*A molecular HeD beam on a ^{209}Bi target and from the

punch-through points for protons and alpha particles (energies where the particles have just enough energy to exit the CsI(Tl) scintillator without stopping in the crystal). Corrections were made for the energy lost in the target, the mylar foil encasing the detectors, and the thin fast-plastic scintillator (the SLOW-region integrations were calibrated). These data were then matched with a set compiled from previous MINIWALL/BALL experiments where the Z-dependent non-linearities of the devices had been determined[58].

2.3.4 Further Description

A detailed description of the MINIBALL detector array can be found in the work of R.T. deSouza et al.[59]. The logic and electronics used for the MINIWALL/MINIBALL array are similar to those used for the Dwarf Ball. A detailed description of the Dwarf Ball detector array can be found in the work of D.W. Stracener et al.[60].

2.4 The Superball Neutron Multiplicity Meter

2.4.1 Principle of Operation

The University of Rochester Superball Neutron Multiplicity Meter is a 4π , 1,600 liter Gd-loaded organic (trimethyl-benzene based) liquid-scintillation detector. The device is built from 5 segments and the scintillation light is detected by 52, 12.7-cm PMTs. This device provides neutron multiplicities on an event-by-event basis that can be associated with other reaction parameters. Figure 2.15 shows a perspective view of the Superball, while figure 2.1 shows a vertical cross section of the device with the MINIWALL/MINIBALL and FA mounted in the Superball's internal vacuum chamber. The Superball collects data when a prompt scintillation signal (created by primary γ -rays and secondary energetic charged particles produced by primary neutrons elastically scattering on hydrogen and elastically and inelastically scattering on carbon) is detected. Subsequent signals are then produced (primarily) when individual neutrons, after thermalization, are captured by the hydrogen and gadolinium components of the scintillator, producing γ -rays which interact in the bulk scintillator. Gadolinium isotopes have very large thermal neutron-capture cross sections (dominated by 2.55×10^5 barn capture cross section of ^{157}Gd) and contribute the most to the capture rate. Capture of the neutrons occurs with high probability after

Superball Neutron Multiplicity Meter

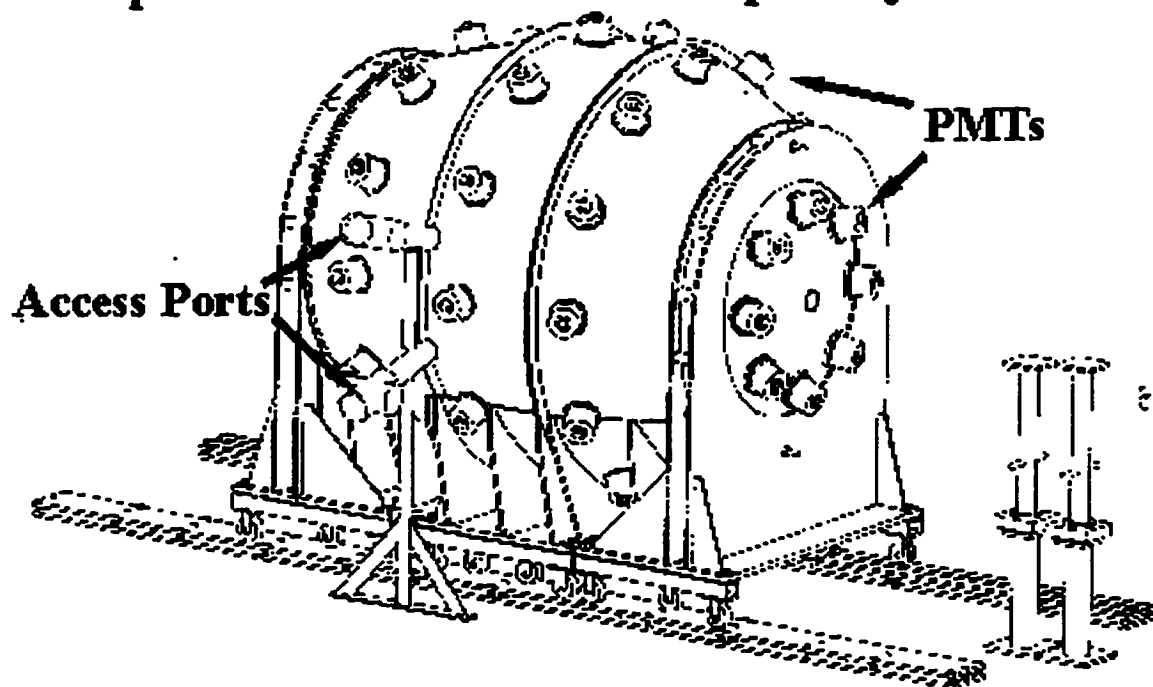


Figure 2.15: A perspective view of the Superball Neutron Multiplicity Meter.

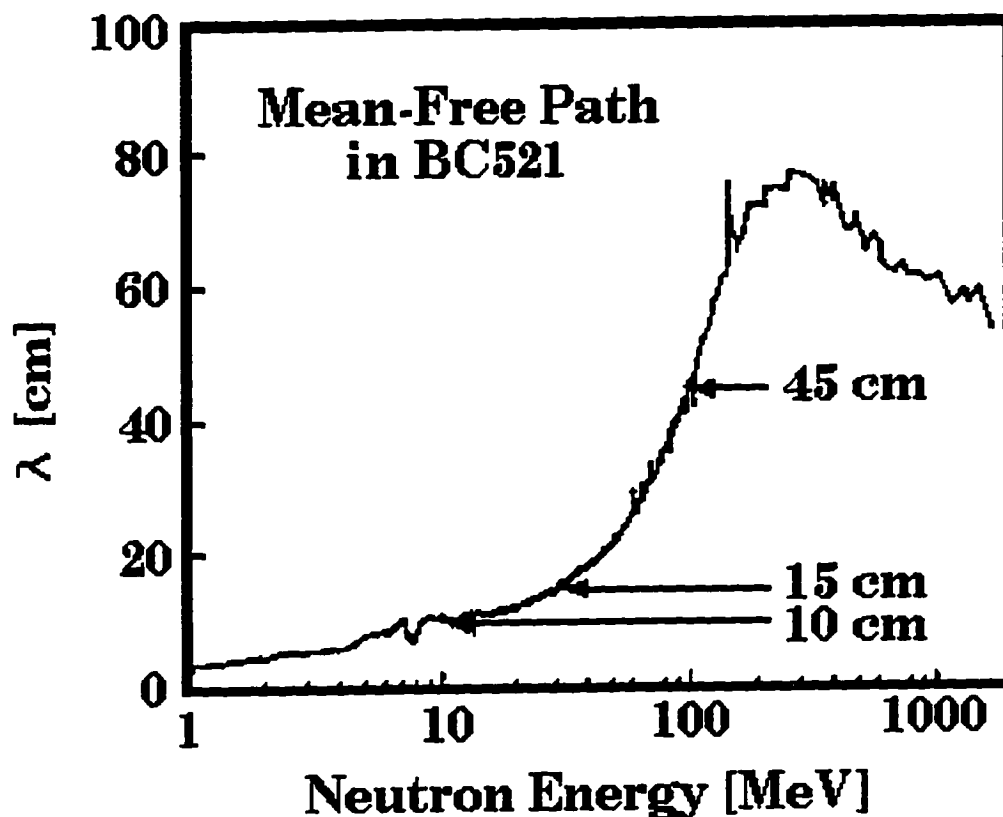


Figure 2.16: The mean-free path of neutrons as a function of energy in BC521, a commercially available Gd-loaded inorganic scintillator, that is very similar to the scintillator fluid used in the Superball.

significant moderation of the neutron energy. Thus, in order for the Superball to efficiently produce capture signals, its dimensions must be such that the neutrons must traverse a distance many times their mean free path in the scintillator. The mean-free path, λ , of neutrons in an organic scintillator, similar to the one used in the Superball, as a function of neutron kinetic energy is displayed in figure 2.16.

The bulk of the neutrons emitted from an intermediate-energy collision would lie approximately between 1 and 100 MeV, with λ 's between 1 and 40 cm respectively. The Superball presents a linear thickness of >1 meter to neutrons emitted from the target position, giving the device a reasonably large efficiency which depends on the source velocity (see calibration section). The simulated distribution of emission-to-capture times for neutrons captured in a Gadolinium-loaded organic scintillator is displayed in figure 2.17. This distribution peaks at $10 \mu\text{s}$, but is rather broad,

Neutron Capture Time Distribution

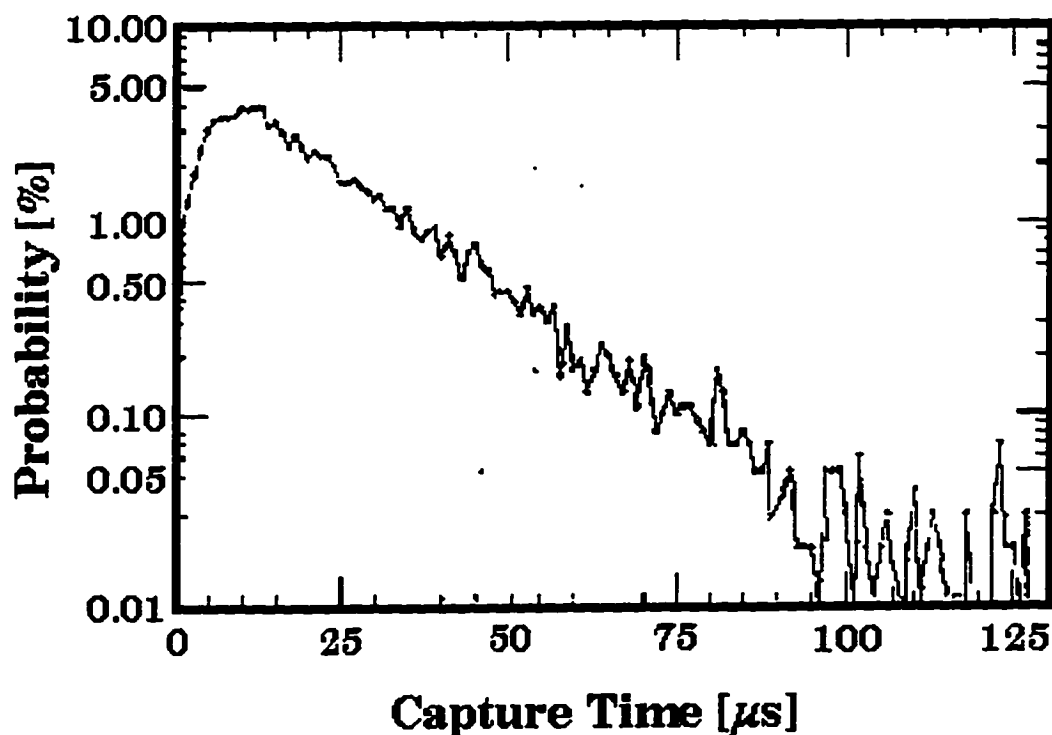


Figure 2.17: The results of a simulated distribution of capture times expected for neutrons with an initial energy of 1.0 MeV that are moderated in the Superball.

reflecting the time scale of this diffusive process. The 12.7-cm PMT's used to read out the Superball have 10 dynodes and a rise time of 10 ns. This allows for the discrimination among the statistically-delayed individual capture pulses, providing neutron multiplicities for each event.

2.4.2 Electronics

A schematic of the electronics used to process signals from the 52 photomultiplier tubes of the Superball is displayed in figure 2.18. The PMT bases have been modified to include a single-transistor preamplifier for the signal from the anode. These amplified anode signals are input directly into 16-channel (one module per tank, 8-12 PMTs) constant-fraction discriminators (CFD). The outputs from the CFDs are

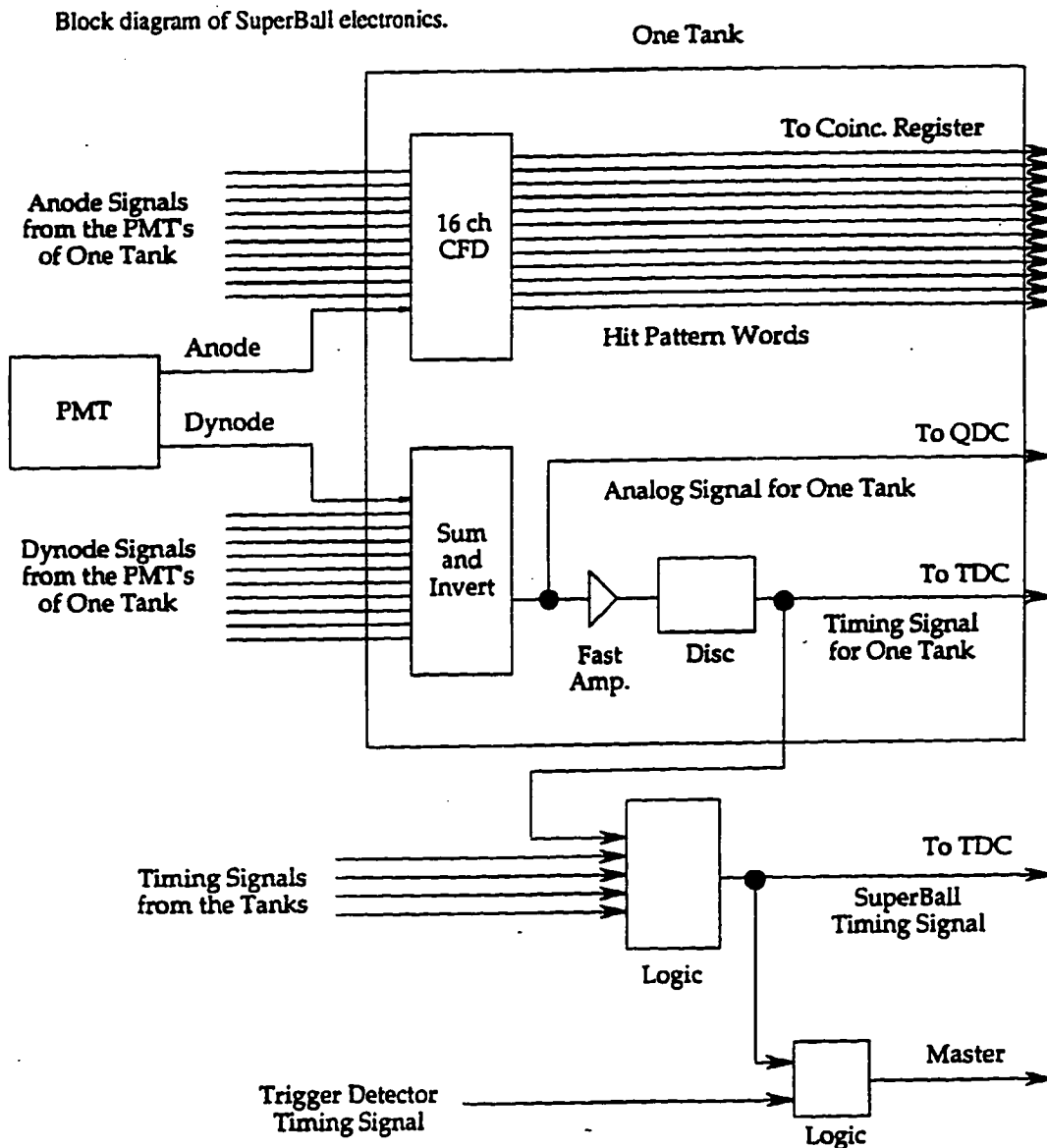


Figure 2.18: A block-diagram schematic of the electronics used to read out the Superball.

Time Sequence of SuperBall Logic Signals

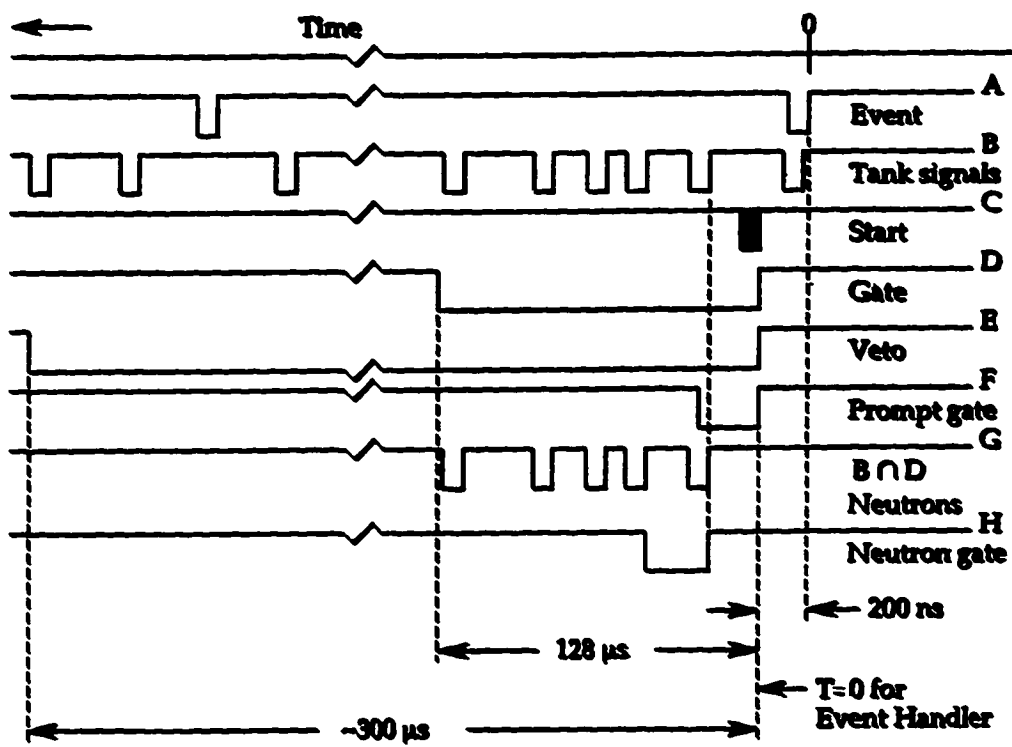


Figure 2.19: A time sequence of logical signals produced by the Superball.

sent to a coincidence register to provide an event hit pattern. Signals from the 10th dynode of the PMTs in a single tank are summed in a fast sum-and-invert module. This summed signal provides both the prompt and delayed light output for each tank. The prompt component is delayed and digitized in a charge-integrating QDC. Logic signals are created by the fast-amplifier discriminator circuit to produce timing, hit pattern, and the integration gate signals. Figure 2.19 displays the time sequence of logical signals produced in a triggered Superball event. The prompt-signal mark is produced at time zero (top line), and time flows forward to the left. If a trigger is in coincidence with the prompt signal, then 200 ns later logical signals are generated to act as: (D) a 128 μs window for capture signal acceptance; (E) a 300 μs veto signal to ensure second triggers do not occur; (F) a prompt integration gate; (G) accepted capture pulses; and (H) an integration gate for capture pulses to monitor capture signals. The 300 μs veto signal produces a significant dead time, making the Superball the rate limiting device in this experiment. The 128 μs acceptance window is necessary to allow time for the energetic neutrons to be moderated (see figure 2.16).

2.4.3 Calibration

As the Superball is used as a multiplicity meter in this experiment, the calibration of the device entails determining the efficiency of neutron detection. Despite our rather low beam current (7.3×10^7 particles per second, as low as possible without sacrificing the charged particle data) and thin target thicknesses ($5.0 \frac{\text{mg}}{\text{cm}^2}$) during the experiment, event pile-up appears to have plagued the effectiveness of the device. This effect limited our use of the data provided by the Superball to simple multiplicity correlations in order to avoid instrumental artifacts. Even without event pile-up problems, the Superball efficiency depends strongly on the velocity of the source or sources from which the neutrons are emitted. The evolution of these sources with the impact parameter of the collision can be estimated from Galilean-invariant cross-section maps of LCPs, see section 3.2. Monte-Carlo simulations of this device have been performed with various sources and multiplicities assigned to these sources in order to estimate neutron efficiencies. Estimates of the efficiency for neutron detection from projectile, target, and center-of-mass sources for these reactions are roughly 33%, 78%, and 80% respectively [61]. Unfortunately, the uncertainties of these efficiencies

are large and a truly quantitative measurement of the efficiency of this device is beyond the scope of this work (due to pile-up problems).

2.4.4 Further Description

A more detailed description of the Superball Neutron Multiplicity Meter can be found in the unpublished report, W.U. Schröder, University of Rochester Report DOE-ER-79048-1[62].

2.5 Trigger Logic

The prime requirement for a valid event was a detected multiplicity of two or greater in the MINIWALL/MINIBALL array. Such an event was identified by the presence of a logical signal produced by a discriminator firing on the linear sum of the logical signals produced by the MINIWALL/MINIBALL array. These logical signals have a standard amplitude of $50 \frac{mV}{hit}$, and the discriminator threshold was set to select the desired multiplicity. This primary trigger was used to preferentially select collision events with sufficient kinetic-energy dissipation to produce IMFs. Elastic and very peripheral collisions have a considerable cross section, and triggering on them would introduce an unacceptable dead time without adding useful data to our study of IMF production.

Secondary triggers were also produced for self-triggered Forward Array events, self-triggered Superball events, Superball random background events, and ^{252}Cf -source triggered Superball events. Self-triggering Forward Array events were produced whenever a logical signal was produced for any of the 16 azimuthal pie-slice segments of the first element. As these triggers include the abundant very peripheral collisions that are biased against with primary trigger, they are scaled down by a factor of 1 in 400 to decrease dead time. Self-triggered Forward Array events provided a means for beam monitoring and calibration via recorded elastic collisions. These events are produced whenever a prompt tank signal produced a logical pulse from the fast-amplifier discriminator circuit. These triggers exclude truly elastic collisions but include events where the dissipation of kinetic energy is insufficient to evaporate charged particles, yet sufficient to evaporate neutrons and produce high-energy γ rays. These events were also scaled down due to their large cross section. While these data may contain

some interesting features, their analysis was beyond the scope of this study. Superball random background events and ^{252}Cf -source triggered Superball events were produced to determine the background of the Superball and monitor the threshold of the Superball by recording fission neutrons in coincidence with an additional Silicon detector attached to a low-activity ^{252}Cf fission source. These events were vetoed using the signal from the Silicon detector attached to the ^{252}Cf fission source when in coincidence with a primary trigger and were used to determine the background and stability of the Superball during the experimental run. The creation of any of these logical triggers during an event was recorded in a Bit-Register module. This signal initiated the read out of the scaling and digitization modules.

2.6 Acquisition Code and Data Format

The digitizing and scaling electronics modules are designed to work with the CAMAC standard computer controlled data acquisition system. A standard acquisition code was modified to read out the digitizing and scaling electronics modules in the format described in table 2. Data blocks were then written out on low-density 8-mm magnetic tapes (2.2 Giga bytes per tape, 36 tapes in total).

The calibrations discussed above were applied to the data and new 8 mm magnetic tapes were written out recording particle-identification (element and when possible isotope), energy, and direction information for all detected particles on an event-by-event basis. These "physics" tapes were then sorted to produce the spectra which are analyzed in the next chapter.

Chapter 3

Data Analysis

3.1 Multiplicity Correlations

3.1.1 Motivation

The multiplicity of reaction products in a heavy-ion collision can provide an observable which grows monotonically with decreasing collision impact parameter, b . This is expected to be the case if the damped relative kinetic energy between the initial projectile and target grows monotonically with decreasing b and is thermalized throughout the system. For peripheral collisions (large b) where little energy is damped, neutral particles are emitted preferentially as they do not have to overcome a Coulomb barrier to be emitted. As b decreases and more energy is damped, neutral and charged decay products begin to compete. For the more violent collisions IMF production rises rapidly, the signature of multifragmentation. Correlations among IMF multiplicities and other reaction product multiplicities can provide information on the evolution of IMF production with decreasing b and increased relative kinetic energy damping. The comparison of multiplicity correlations among the four systems studied can illuminate any presence of entrance-channel N/Z influence on the probability of producing IMFs.

3.1.2 Neutron and Charged Particle Correlations

Figure 3.1 shows the correlation between the number of detected charged particles (N_c) and the number of detected neutrons (N_n) for all four systems. These events

required the primary reaction trigger, resulting in a lack of data below $N_c = 3$. The dependence of the average value of N_n , $\langle N_n \rangle$, along the ridges in these correlations are shown in figure 3.2. The correlations exhibit the same general shape for all four systems, with N_n rising rapidly for small values of N_c , then leveling off. The salient differences are an increase in $\langle N_n \rangle$ of about 6 to 12 neutrons in going from the neutron-deficient projectile and target system LL to the mixed systems LH and HL, and another 6 to 12 neutron increase in going from these systems to the neutron-rich projectile and target system HH. Closer inspection of figure 3.2 shows that the increase in $\langle N_n \rangle$ is not constant with increasing N_c .

The maximum total offset, between LL and HH, occurs at moderately low values of $N_c \approx 10$ and reaches 22 neutrons while for the upper half of the N_c distribution, the offset is only 12 units. While this difference is certainly physical, it does not necessarily mean that different mechanisms of energy dissipation occur in the systems at the same excitation energy or b . Rather, it seems more likely that due to the differences in initial N/Z for the projectile and target of each system, the multiplicities (e.g. N_c) are incomplete measures of excitation energies and hence sample different b 's.

To understand this, consider the statistical de-excitation of the neutron-rich projectile ^{136}Xe and the neutron-poor projectile ^{124}Xe , where they produce the same number of charged particles. The ^{136}Xe has to have more initial excitation energy than the ^{124}Xe in order to evaporate its neutron excess and yet reach the same charged particle multiplicity. In this case, it is more instructive to view the differences between these curves when horizontal shifts are applied to these data, roughly producing an excitation energy axis. For example, the difference between the values of $\langle N_n \rangle$ for LL and HH is almost constant (at about 12 units) with N_c if the LL data are shifted on the abscissa by about 4-5 units. The implication of this logic when applied to figure 3.2 for both N_c and $\langle N_n \rangle$ is that with the exception of the lowest values of N_c , the incremental neutron-to-charged-particle emission ratios are independent of system. Attempts to reproduce the dependence of $\langle N_n \rangle$ on N_c with statistical model calculations are discussed in section 4.1 along with the insight derived from this effort.

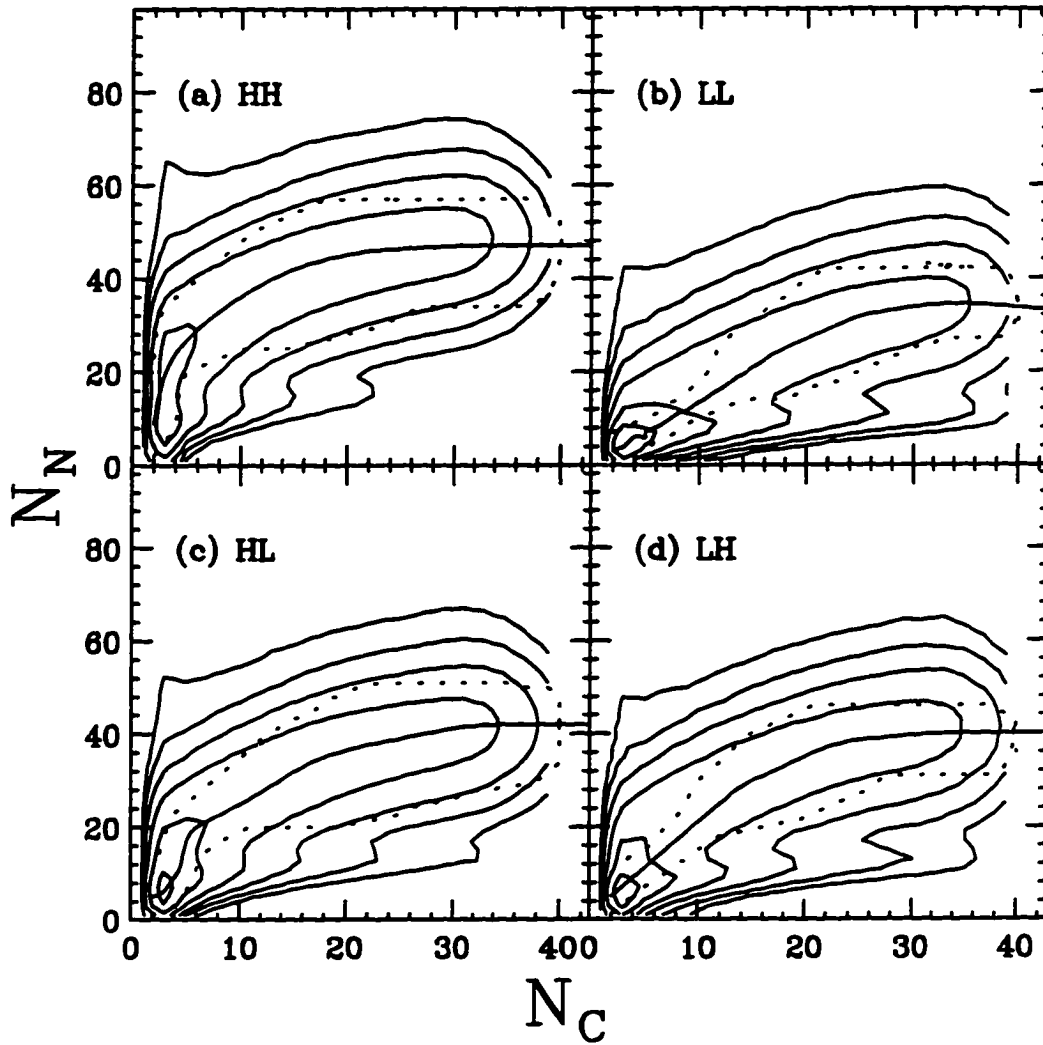


Figure 3.1: Correlations between the number of detected charged particles (N_c) and the number of detected neutrons (N_n) for all 4 systems. The solid lines depict the ridges of the correlations (most probable value of N_n for each value of N_c). The dashed lines bracket the ridge and define the region used for generating mean values. The small second ridge at low values of N_n is due to instrumental effects.

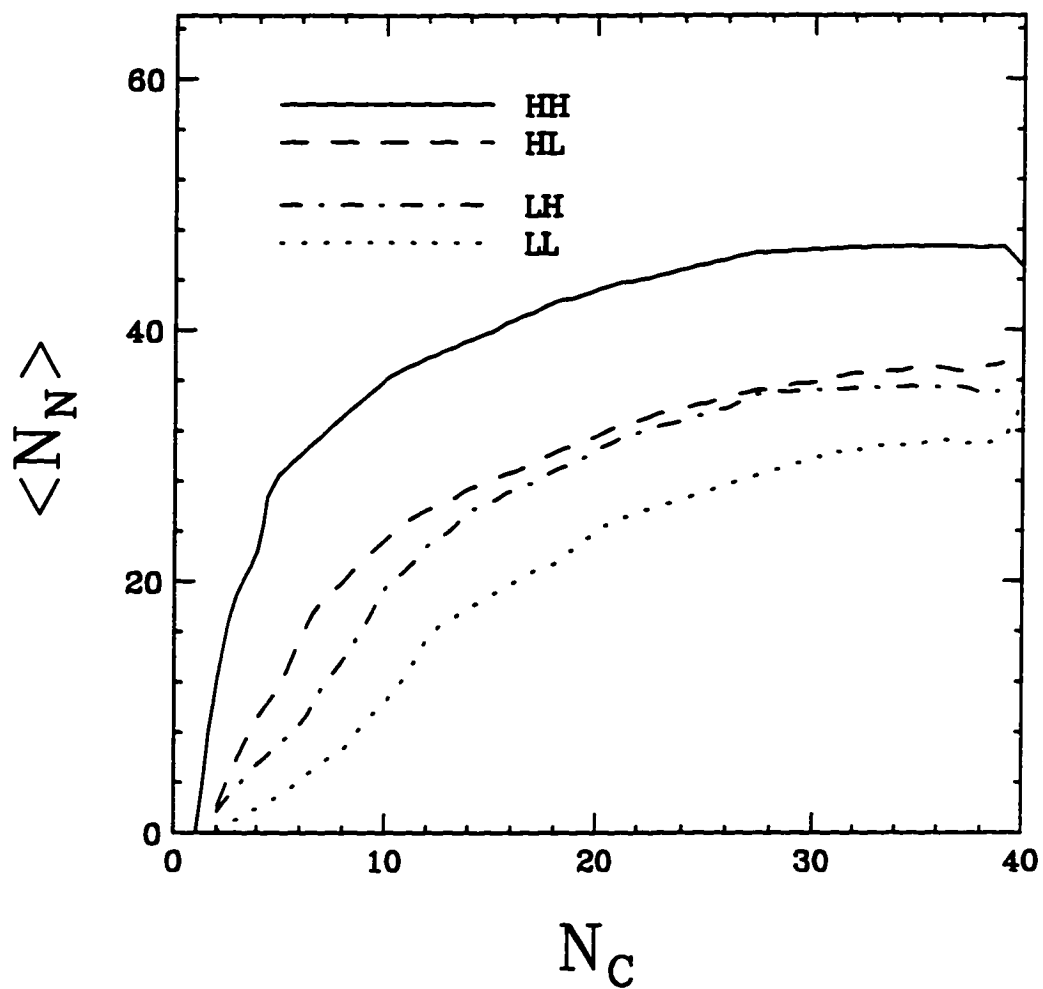


Figure 3.2: Average value of N_n for each value of N_c for the 4 systems. The averages are calculated from the data inside the bracketed region (dotted lines) in figure 20. These data have been corrected for background but not efficiency.

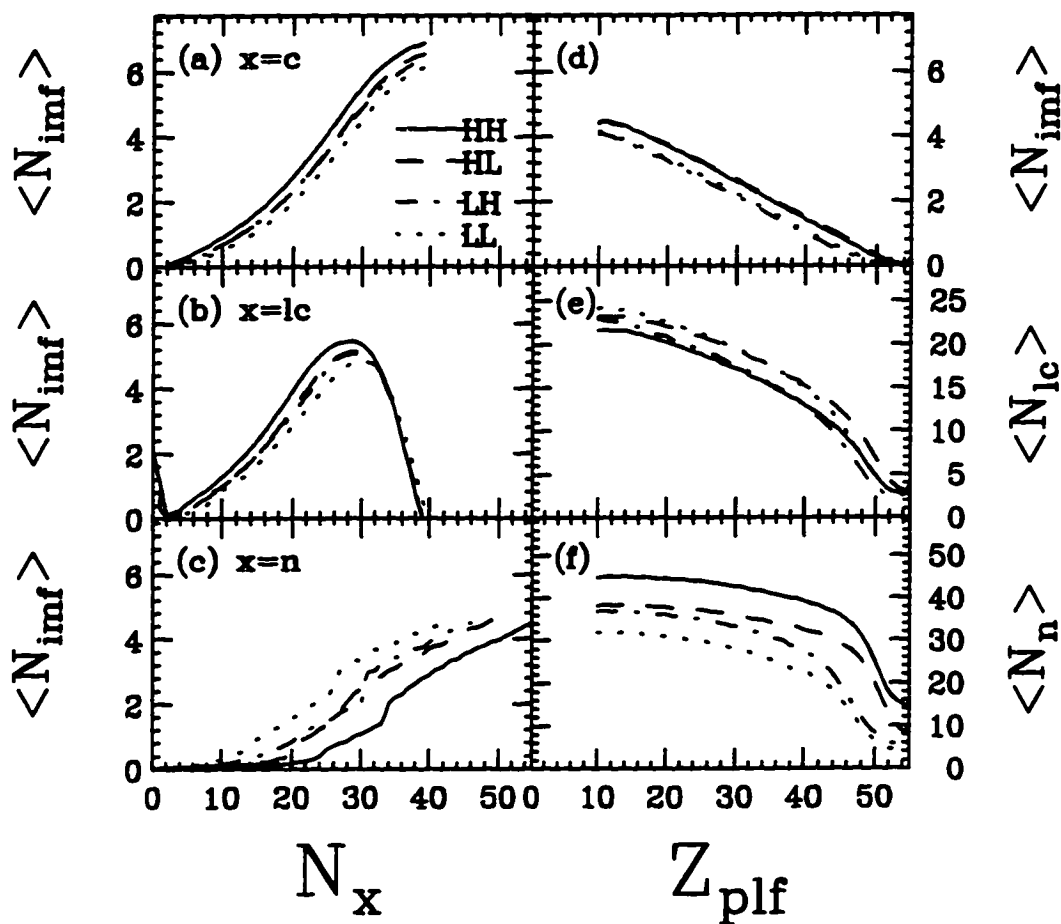


Figure 3.3: The dependences of the average number of detected IMFs ($\langle N_{imf} \rangle$) on (a) the number of detected charged particles (N_c), (b) the number of detected light-charged particles (N_{lc}), and (c) the number of detected neutrons (N_n) are shown on the left-hand side. On the right-hand side, the dependences of (d) N_{imf} , (e) N_{lc} , and (f) N_n on the charge of the projectile-like fragment (Z_{plf}) are shown. Each panel shows the dependences for all four systems. The same key is used throughout.

3.1.3 IMF and Z_{plf} Correlations

The dependences of the average number of detected IMFs ($\langle N_{imf} \rangle$) on the total detected number of charged particles (N_c), the number of detected light charged particles (N_{lc}) and the number of detected neutrons (N_n), are shown in figure 3.3 (sections a,b, and c, respectively) for all four systems. The values of $\langle N_{imf} \rangle$ increase with increasing N_c , N_{lc} , and N_n , with the exception of the largest values of N_{lc} where charge conservation requires an anti-correlation between N_{imf} and N_{lc} . In addition to these trends, which are exhibited by all of the systems, the values of $\langle N_{imf} \rangle$ increase with increasing neutron richness of the system for fixed values of N_c (a) and N_{lc} (b). Conversely, $\langle N_{imf} \rangle$ decreases with increasing neutron richness of the system at fixed values of N_n (c). As was the case with figure 3.2, a more insightful way to view the curves shown on the left-hand side of figure 3.3 comes with the realization that the curves in each panel are almost identical to one another aside from a shift of the abscissa. As discussed above, the shifts are what one would expect if the various multiplicities represent incomplete measures of excitation energy due to differences in initial N/Z . A consistent shifting of these abscissae relative to the HH system is shown in figure 3.4 (sections a,b, and c, respectively). The shifts are listed in Table 3. Displayed versus these shifted abscissae, the $\langle N_{imf} \rangle$ appears to be independent of system except for the largest values of $\langle N_{imf} \rangle$. For the largest values of $\langle N_{imf} \rangle$, the values increase with increasing N/Z of the system. This point is significant in that it reflects, in great measure, on the survivability of the primary IMFs produced and perhaps on differences in primary IMF yields in central collisions.

One of the most striking trends of these data is the dependence of $\langle N_{imf} \rangle$ on the charge of the projectile-like fragment, Z_{imf} , detected in the Forward Array. This is shown in figure 3.3 (d). Here one sees that the number of detected IMFs increases by one for every 10 charges lost from the projectile. This rate is independent of the system, however, there is an offset which depends only on the projectile. The systems with the neutron-rich projectile produce, on the average, 0.4 more intermediate-mass fragments for the same charge loss or alternatively, the systems with the neutron-deficient projectile must lose, on the average, 4 additional charge units before IMF production proceeds at the rate mentioned above. This offset is removed by shifting the abscissae of the LH and LL systems by 4 N_c relative to the HH and HL systems.

The bias imposed by the detection of a PLF ($Z > 10$ detected in the Forward Array) reduces the maximum value of $\langle N_{imf} \rangle$ by about 2 units (1 if you count the

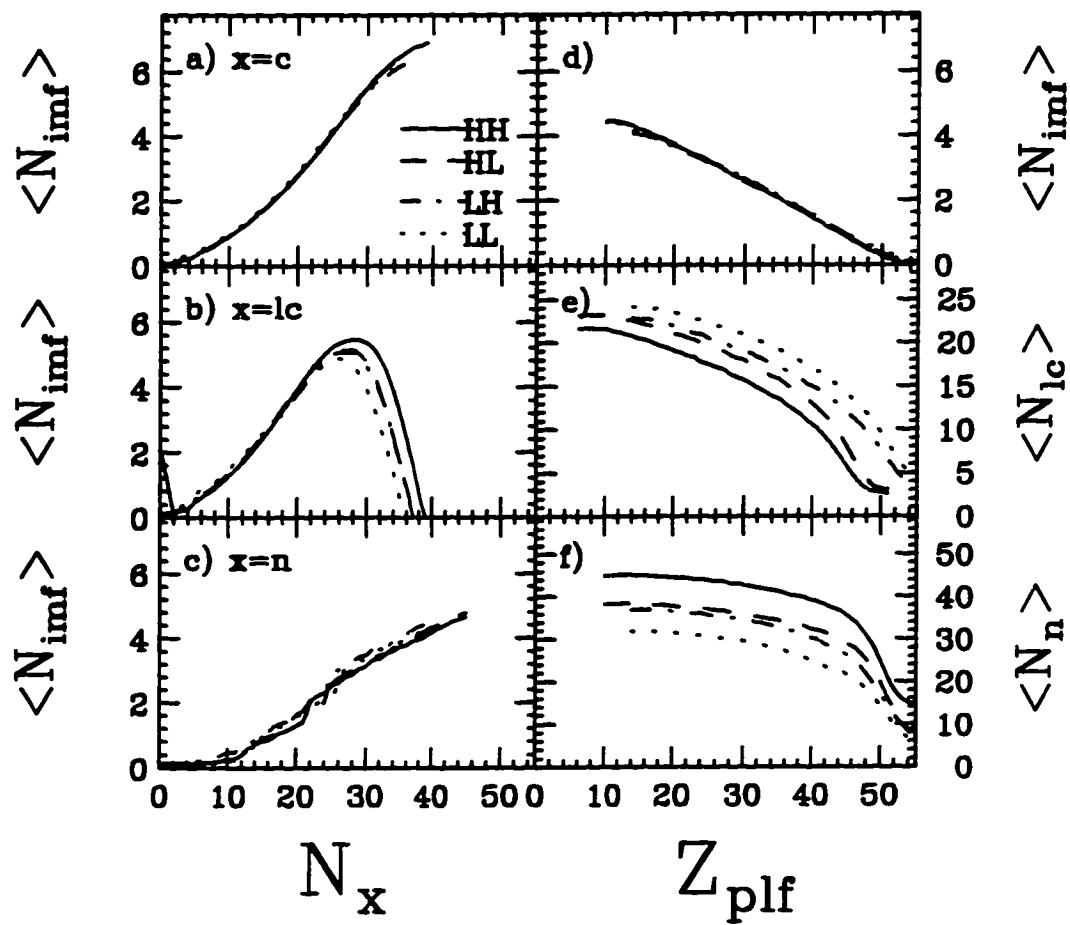


Figure 3.4: The same as figure 22 but with the multiplicity shifts indicated in table 3.1 applied to the data.

Table 3.1: Multiplicity Shifts

System	δN_n	δN_c	δN_{lc}	δZ_{plf}
LL	0	4	4	4
LH	6	2	2	4
HL	6	2	2	0
HH	12	0	0	0

detected PLF as an IMF). The lost fraction of the IMF distribution amounts to about 10% which corresponds to an upper limit of the *lost* cross section (upper limit due to the loss of peripheral collisions omitted by the primary trigger) of about 0.4 b. The other multiplicities, N_{lc} (e) and N_n (f), are not as simply associated with Z_{plf} and the projectile charge-to-mass ratio as is N_{imf} . The trend in the values of N_{lc} show the necessarily complementary, charge-conserving trend to that observed for N_{imf} . Here, there is a kinematical bias for the largest values of Z_{plf} which favors the HL system and suppresses the LH system. This bias is more evident for the LCPs than for IMFs because the former are much more characteristic of emission from the target-like and projectile-like fragments while the latter are more focused in the mid-velocity region ($V_{par} \approx 0$ in the center-of-mass frame). As will be seen in Section 3.2., the MINIWALL/MINIBALL array threshold is centered around the target-velocity frame (corresponding to small velocities in the laboratory rest frame) and leads to this kinematical bias for LCPs. The values of $\langle N_n \rangle$ evolve from ones which depend on the charge-to-mass ratio of the projectile, when Z_{plf} is near to that of the projectile, to plateau values which depend on the total number of neutrons in the system for the smallest values of Z_{plf} . The difference observed at large values of Z_{plf} is due to the offset described above (the systems with the light projectile damp less energy to produce the same value of Z_{plf} .) The convergence of the HL and LH data sets, when Z_{plf} gets very small, is expected from the approximate symmetry of the systems and the relatively high efficiency of the Superball for neutron detection from the center-of-mass frame which is to likely dominate the emissions in this limit. These data do not imply that charge-to-mass equilibration between the target and projectile is approached when Z_{plf} is small. As we shall see later in section 3.3.2 this equilibration process is incomplete even in this limit.

3.1.4 Summary

Accounting for the effects of different entrance-channel projectile and target N/Z , the data indicate that both the incremental neutron-to-charged-particle emission ratios and the production of IMFs are nearly identical for all four systems when viewed as functions of excitation energy. Slight differences remain in the maximum value of $\langle N_{imf} \rangle$ observed, with the values increasing with increasing N/Z of the system. These differences point to either a variation in the survivability of the IMFs produced or in the primary IMF production probabilities. Further discussion of this point, in light of statistical-model calculations, is pursued in Section 4.1.

3.2 Emission Patterns in Velocity Space

3.2.1 Motivation

The emission patterns of LCPs and IMFs in velocity space are important observables when attempting to determine the origin of these fragments. Fragment-source characteristics can be determined from these emission patterns and used to guide our physical understanding of fragment production mechanisms. Features such as ridges of Coulomb-boosted fragments surrounding a region of minimal yield or “Coulomb hole” can reveal the presence of large highly charged fragment sources. The position of these sources along the velocity component parallel to the beam axis (\vec{V}_{par}) can identify the emissions as originating from sources that are characteristic of the projectile, the target, or the center-of-mass frames. Emission patterns of IMFs in particular are of interest due to the theoretical difficulties involved in explaining their copious yields.

The emission patterns of PLFs in velocity space have also been important observables when attempting to characterize the dominant reaction mechanism observed in systems similar to the ones studied in this work[40, 63, 64]. The damping of PLF velocity from the initial beam velocity is an observable that can be directly compared with the dynamical predictions of reaction models. As seen in figure 3.3 (d), the charge of the PLF remnant is linearly related to the value of $\langle N_{imf} \rangle$, suggesting a strong correlation between the excitation of and mass loss from the PLF and IMF production. Further correlation of these quantities with the velocity of the PLF can provide a more complete picture of IMF production.

3.2.2 Z_{plf} Emission Patterns

The influence of IMF production on the degree of kinetic-energy damping (and velocity damping as $v \propto KE^{1/2}$) is shown in figure 3.5 for the LL system. In order to construct this plot we have used the post-evaporative mass relation given by Charity et al. [65].

$$\langle A_{plf} \rangle = 2.08 \cdot \langle Z_{plf} \rangle + 0.0029 \cdot \langle Z_{plf} \rangle^2 \quad (3.1)$$

This relation is a correlation between the average Z and A of evaporation residues predicted by standard statistical-model calculations. These average masses should be accurate to within a few units except for charges near the projectile, when the available excitation energy is very small. However for the LL system shown, this error should be less than 10%. All of the systems exhibit these same features and the maps gated on N_{imf} are similar to those gated on Z_{plf} . In the latter case (as was demonstrated previously) gating on progressively increasing values of N_{imf} is equivalent to gating on progressively decreasing values of Z_{plf} .

As discussed above, there is a close tracking of the mean value of Z_{plf} with the number of IMFs. The plots of the other three systems are similar. In addition, this plot illustrates two other important features of these reactions. Firstly, the extent of velocity damping is very small (at most 10% of the total relative velocity) and secondly, the average damping is independent of the size of the remnant while the variation in damping grows with decreasing remnant size.

The small degree of damping in slightly lower-energy collisions of very heavy nuclei has been discussed before [40, 64] and is a fundamental feature of these reactions which is not reproduced by mean-field calculations. Here (at 55 MeV*A) the disagreement with model calculations also exists and is discussed in Section 4.2. The important features mentioned above are collected in one-dimensional plots (using mean values) in figure 3.6. This figure illustrates that: a) The degree of kinetic energy damping is small and, to a very large extent, independent of system. b) More charge is lost per detected IMF when the projectile is neutron poor. c) Overall, more IMFs are detected when the projectile is neutron rich.

3.2.3 IMF and LCP Emission Patterns

Figure 3.7 shows the Galilean-invariant cross-section maps for α -particles, ${}^6\text{He}$, and Li fragments for four different gates on Z_{plf} for the HH system. The Galilean-invariant

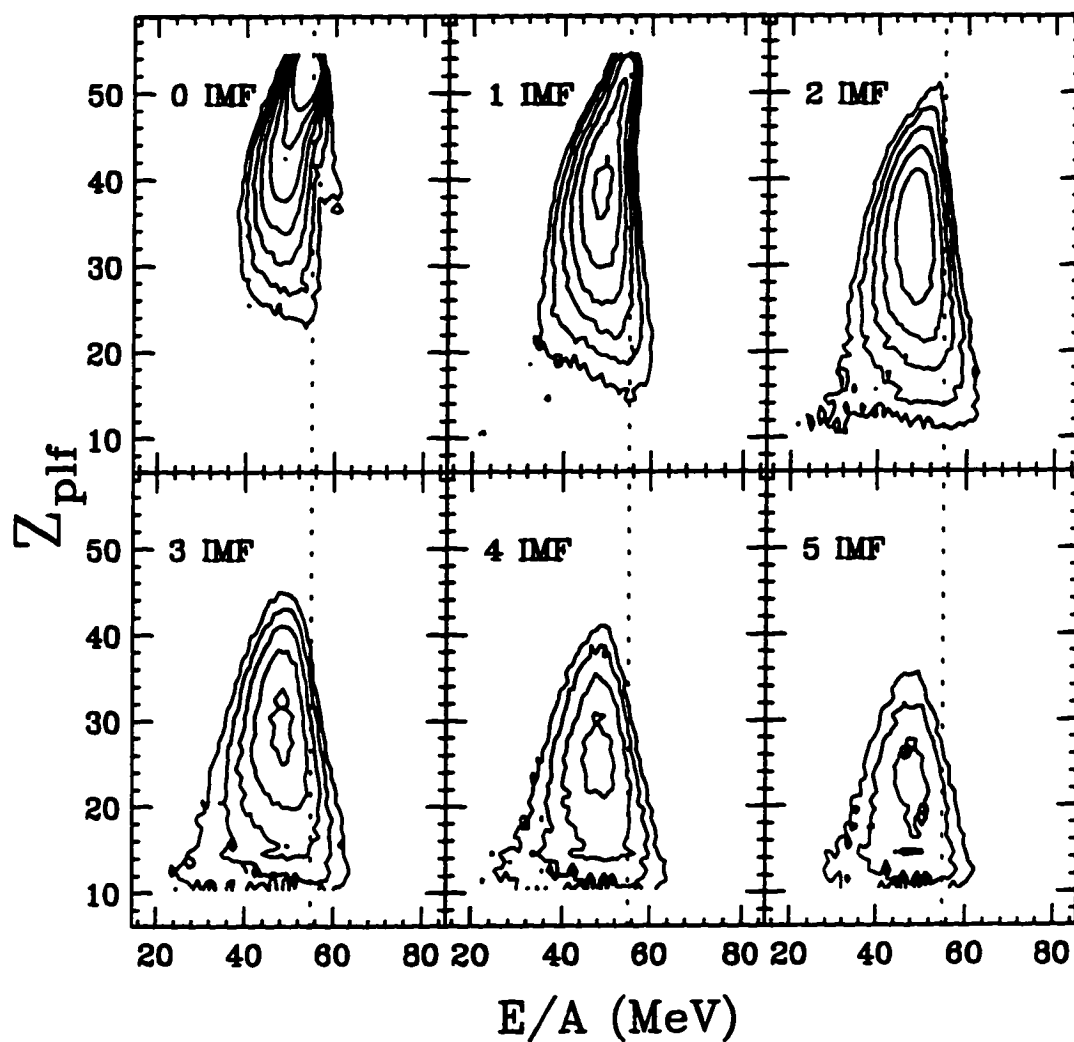


Figure 3.5: Contour plots showing the variation of cross section with the the charge of the projectile-like fragment Z_{plf} and the energy per nucleon E/A for different numbers of coincident intermediate-mass fragments. The data from the LL system is displayed here. The dotted line is at the projectile energy 55 MeV/A. The data for the other systems look very similar.

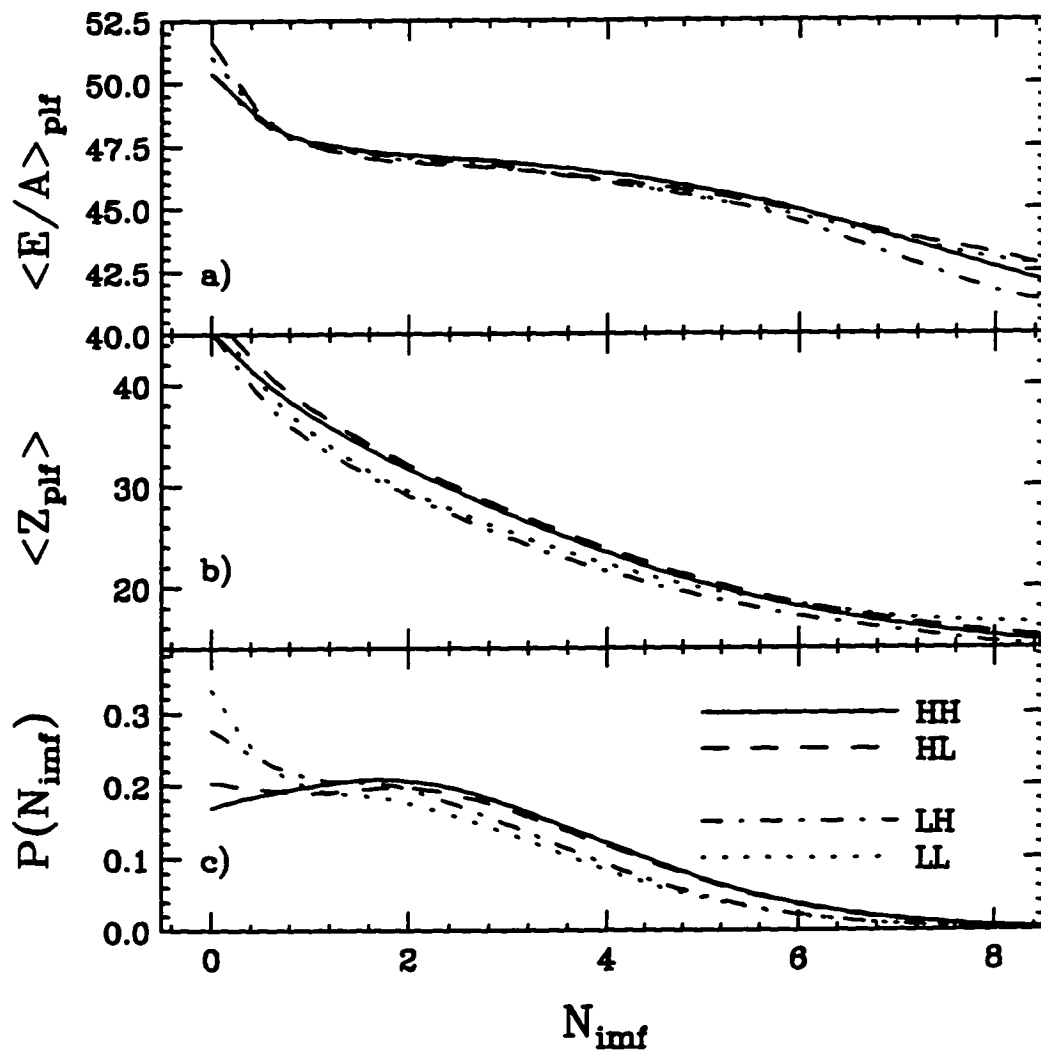


Figure 3.6: The variation of $\langle E/A_{\text{plf}} \rangle$ (a), $\langle Z_{\text{plf}} \rangle$ (b), and the fractional yield or normalized probability of detecting a given number of IMFs (c), are shown as a function of the number of detected IMFs for all four systems.

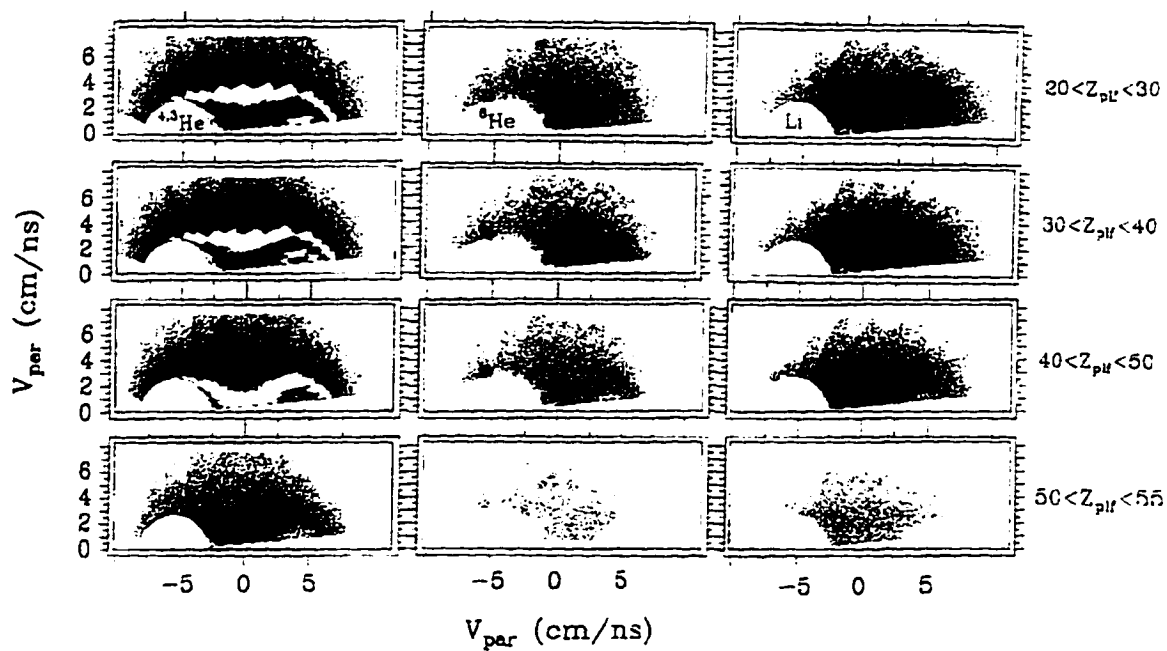


Figure 3.7: Galilean invariant cross section maps for α -particles (left hand side), ${}^6\text{He}$ fragments (center), and Li fragments (right hand side) for four different gates on the charge of the projectile remnant, Z_{plf} (as indicated) for the HH system. These plots are boosted into the center-of-mass system and use a logarithmic color scale. The projectile velocity is ~ 5.0 cm/ns.

cross-section ($\propto \frac{\delta^3\sigma}{\delta v_x \delta v_y \delta v_z}$) maps are plotted as a function of velocity parallel to the beam velocity (V_{par}) on the abscissa and velocity perpendicular to the beam velocity on the ordinate (V_{per}), such that zero is at rest in the center-of-mass frame. Cross-section maps for the other three systems are similar. The velocity maps for α particles exhibit a strong projectile-like component, characterized by a “Coulomb hole” centered on the projectile velocity ($\approx 4.8 \frac{cm}{ns}$), when Z_{plf} is large. The “Coulomb hole” resulting from target-like emission is masked by the detection thresholds (hole centered about $V_{par} = -5.0 \frac{cm}{ns}$) but part of its forward ridge is visible. While the prominence of this component fades with decreasing Z_{plf} , it is always present and its center moves only slightly with Z_{plf} (consistent with the small amount of velocity damping observed for PLFs). A quite different trend is seen for ${}^6\text{He}$ fragments which, independent of Z_{plf} , exhibit an eccentric cross-section distribution, peaked at the center of mass, stretched along the beam direction, and with almost no indication of a projectile “Coulomb-hole”. To a large extent the emission characteristics for Li are similar to those for ${}^6\text{He}$. Here, however, there is more evidence for a projectile “Coulomb-hole” (when $Z_{plf} > 30$). More interesting than the presence of this weak “Coulomb-hole” is its asymmetry in the projectile frame. The backward portion is substantially more intense than the forward part. This emission pattern has been noticed before [41, 43] and is inconsistent with either emission from a single source at rest in the center of mass or sequential emission from target-like and projectile-like sources.

3.2.4 IMF- Z_{plf} and LCP- Z_{plf} Azimuthal Correlations

The azimuthal correlations between the PLF and either LCP’s or IMFs, as discussed in the introduction, have also helped in distinguishing between fragment-emission mechanisms. PLF-IMF correlations, cut on Z_{plf} and V_{par} , are shown for PLF-Li pairs in figure 3.8. The PLF- α and PLF- ${}^6\text{He}$ correlations are similar to those shown. The correlations in the mid-velocity region are found to evolve from being flat or uncorrelated when gated on small values of Z_{plf} (small b) to functions which are peaked at 180° for larger values of Z_{plf} (large b). The correlations in the projectile-velocity region on the other hand, are found to be strongly peaked at 180° when gated on all values of Z_{plf} , with the functions becoming more severely peaked at 180° for larger values of Z_{plf} . 180° correlations are expected for the case of asymmetric fission of the PLF or binary-sequential decay of the PLF, due to Coulomb repulsion between

the two separating fragments. This 180° correlation is expected to diminish with an increase in the excitation (a combination of a weakening of the Coulomb influence and an increase in the number of recoil kicks suffered by the PLF) and thus increase in the average velocity of the emitted particles. It is also expected to diminish due to the influence of fragments other than the correlated pair. The 180° correlations are strong for the bulk of the α -particle yield, as most emissions are from the projectile-velocity region. However, the bulk of the IMF yield is found in the mid-velocity region and in more central collisions where there is less azimuthal correlation with the PLF. Due to the flat azimuthal correlations found there, that this decay is not obviously of a binary sequential nature and may be influenced by the presence of a TLF fragment (as would be expected in a neck rupture scenario). Unfortunately, the lack of correlation may just be the result of increased excitation in the mid-velocity region, as it is surely the cause of the decrease of the 180° correlations in the projectile-velocity regions.

3.2.5 Summary

The extent of velocity damping for PLFs is very small (at most 10% of the total relative velocity) and the average damping is independent of the size of the remnant while the variation in damping grows with decreasing remnant size. These observations provide an important set of observables for testing current dynamical reaction models. IMFs and LCPs display markedly different emission patterns. The LCP emissions patterns indicate mainly sequential decay from a TLF or PLF source, while the IMF emission patterns emanate mainly from the center of mass with patterns that may be inconsistent with simple sequential decay. These emission patterns along with the observation that Li fragments exhibit a partial Coulomb ridge (between center-of-mass and PLF frames) is consistent with the observations of previous studies of similarly heavy systems at intermediate energy which attribute such features to a neck -fragmentation or proximity-fission mechanism.

3.3 Isotope Ratios

3.3.1 Motivation

The invariant cross-section maps shown in the previous section illustrate that ${}^6\text{He}$ and ${}^4\text{He}$ have quite different emission patterns. This suggests that the N/Z of emitted

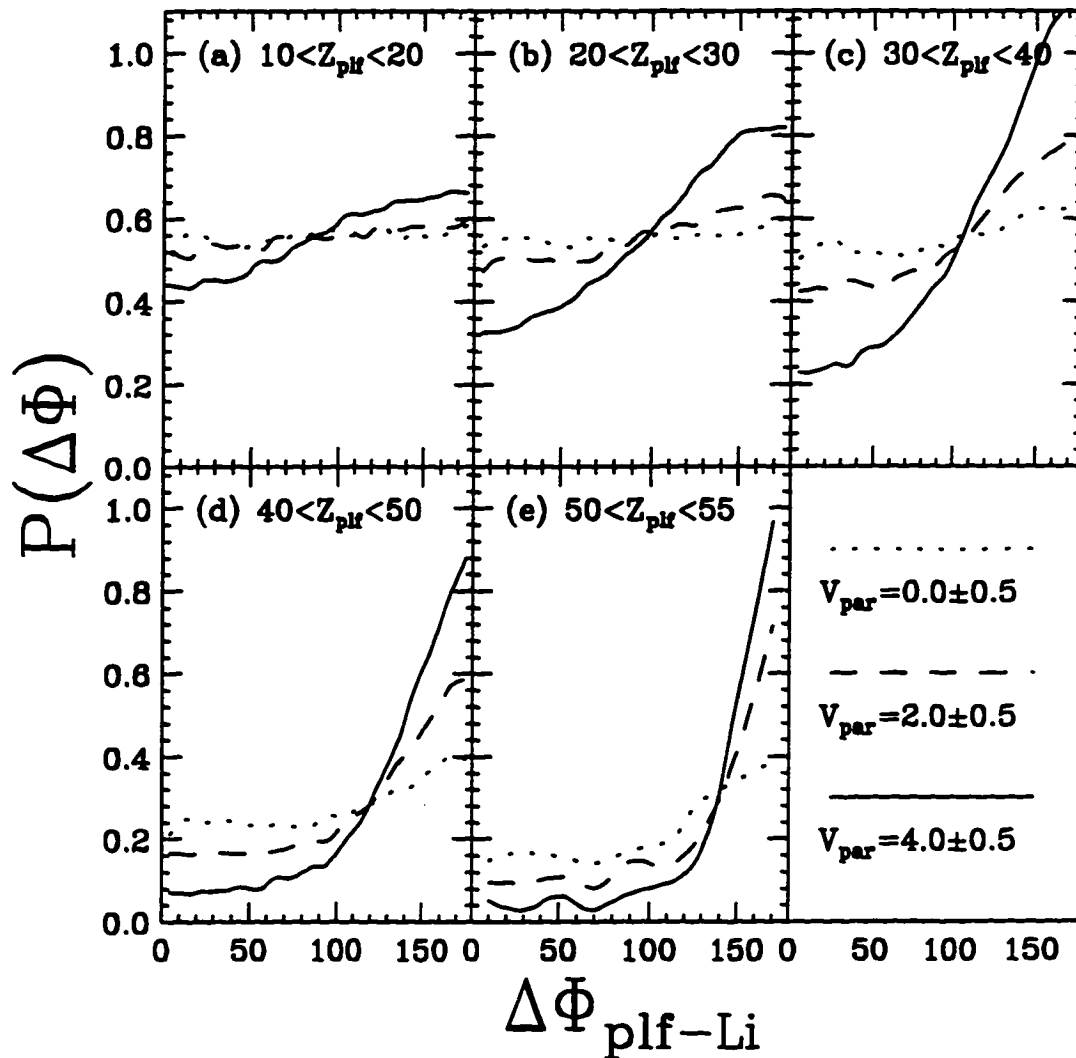


Figure 3.8: Azimuthal distributions of Li fragments relative to the PLFs for 5 bins in Z_{plf} and three cuts in velocity parallel to the beam velocity V_{par} (in the center-of-mass system) for the HH system. Because the PLFs and the Li fragments are detected in different arrays (FA and MINIWALL/BALL, respectively), the detection method does not impose an auto-correlation. The angle, $\Delta\Phi$ is defined relative to the PLF direction.

fragments may vary strongly as a function of either V_{par} or Z_{plf} . The N/Z signature of the emitted IMFs are new observables investigated by this work. As experimentalists, we hope to provide the most complete picture of the physical system of interest such that attempts at a theoretical description of the system are adequately constrained. The N/Z ratios of these fragments can provide essential clues to their origin, hopefully limiting the scope of possible production mechanisms. These ratios can also track the evolution of charge equilibration or neutralization.

3.3.2 Charge Neutralization

The dependence of the ${}^6\text{He}/{}^4,{}^3\text{He}$ ($R_{6/4}$) isotopic ratio, together with the ${}^6\text{He}/\text{Li}$ ($R_{6/\text{Li}}$), and $t/{}^3\text{He}$ ($R_{3/3}$) “isobaric” ratios on V_{par} and Z_{plf} are shown in figures 3.9 and 3.10 respectively. Due to incomplete isotope resolution throughout the entire angular range, some isotopes have been mixed in order to create ratios in which one can have confidence. Therefore the $R_{6/\text{Li}}$ ratio, which uses all particle-bound Li isotopes, is only approximately isobaric. The variation of these ratios, which all have the yield of the more neutron-rich species in the numerator, with V_{par} and Z_{plf} are among the most important experimental observations of this work.

An obvious feature of both of the figures is the diminution of the difference between the cross-over systems (HL and LH) as the value of Z_{plf} decreases or V_{par} approaches zero (this is most clearly seen in the $R_{6/4}$ ratio). As the cross systems have the same composite N/Z , charge equilibration would produce equivalent ratios for the most violent collisions. A considerable amount of entrance-channel memory should be expected in these systems, however, in light of the multiplicity correlations discussed in section 3.1. There it was found that an offset is necessary in the Z_{plf} abscissae for systems with different projectile N/Z , independent of the N/Z of target, to compare similar excitation energy events. This indicates that the PLF remnant is not greatly influenced by the N/Z of the target.

The fact that the cross systems approach, in the limit of very small values of Z_{plf} or V_{par} , but never actually match each other is thus expected. Studies of heavy-ion reactions just above the Coulomb barrier[66] have found that charge-to-mass equilibration does not occur sufficiently rapidly to be completed within the interaction time for a large fraction of the damped reaction cross section. The possibility of equilibration becomes even less likely at the higher bombarding energies of

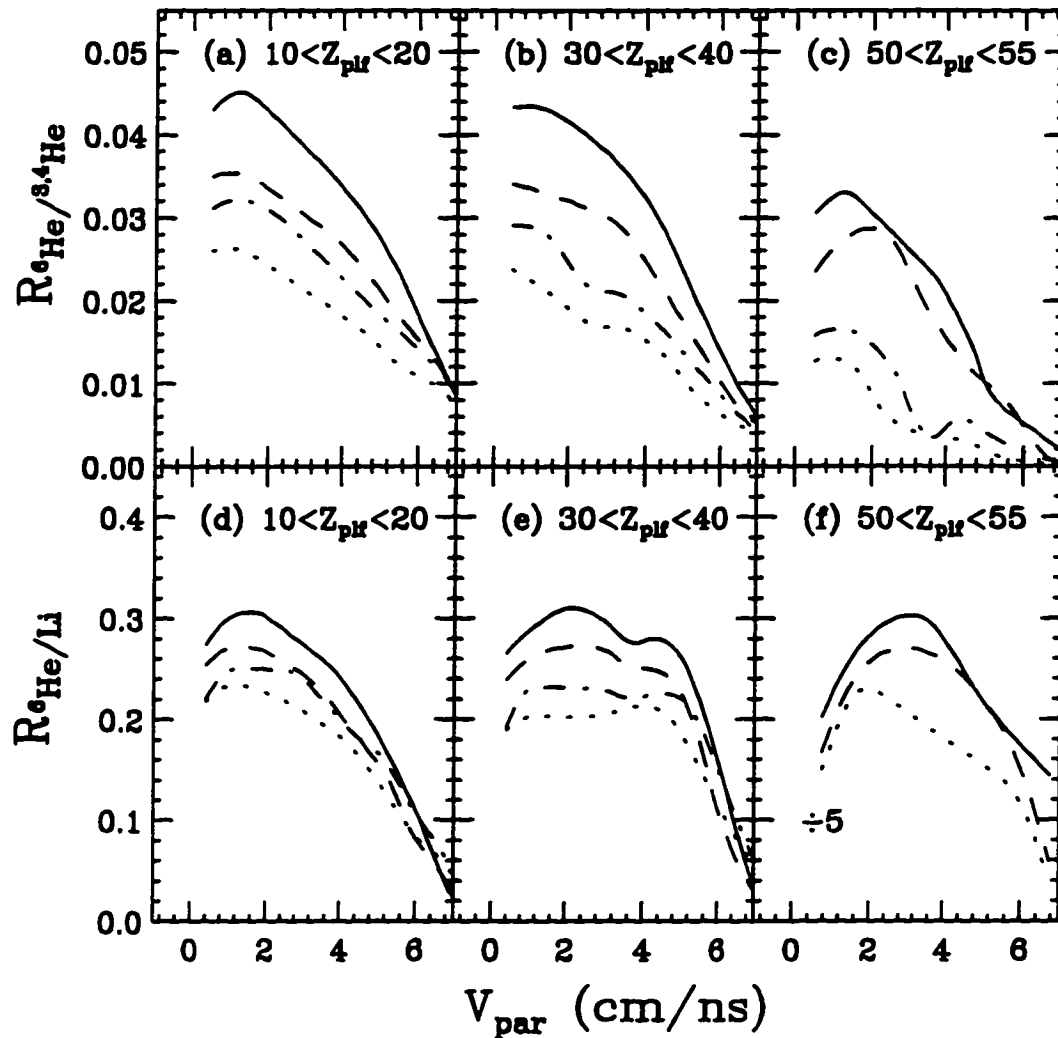


Figure 3.9: The relative yield of ${}^6\text{He}$ to ${}^{3,4}\text{He}$ (a)-(c) and ${}^6\text{He}$ to Li (d)-(f) are shown as a function of V_{par} (in the center-of-mass system) for several gates on Z_{plf} . The key for the lines is the same as that used in the previous figures. For clarity, the data points themselves are suppressed. The statistical uncertainties are generally less than 5% with the exception of the LH system when Z_{plf} is large, in which case the statistical uncertainties are (when these data are shown) less than 15%. The ratios in (f) have been multiplied by a factor of 5 for display purposes.

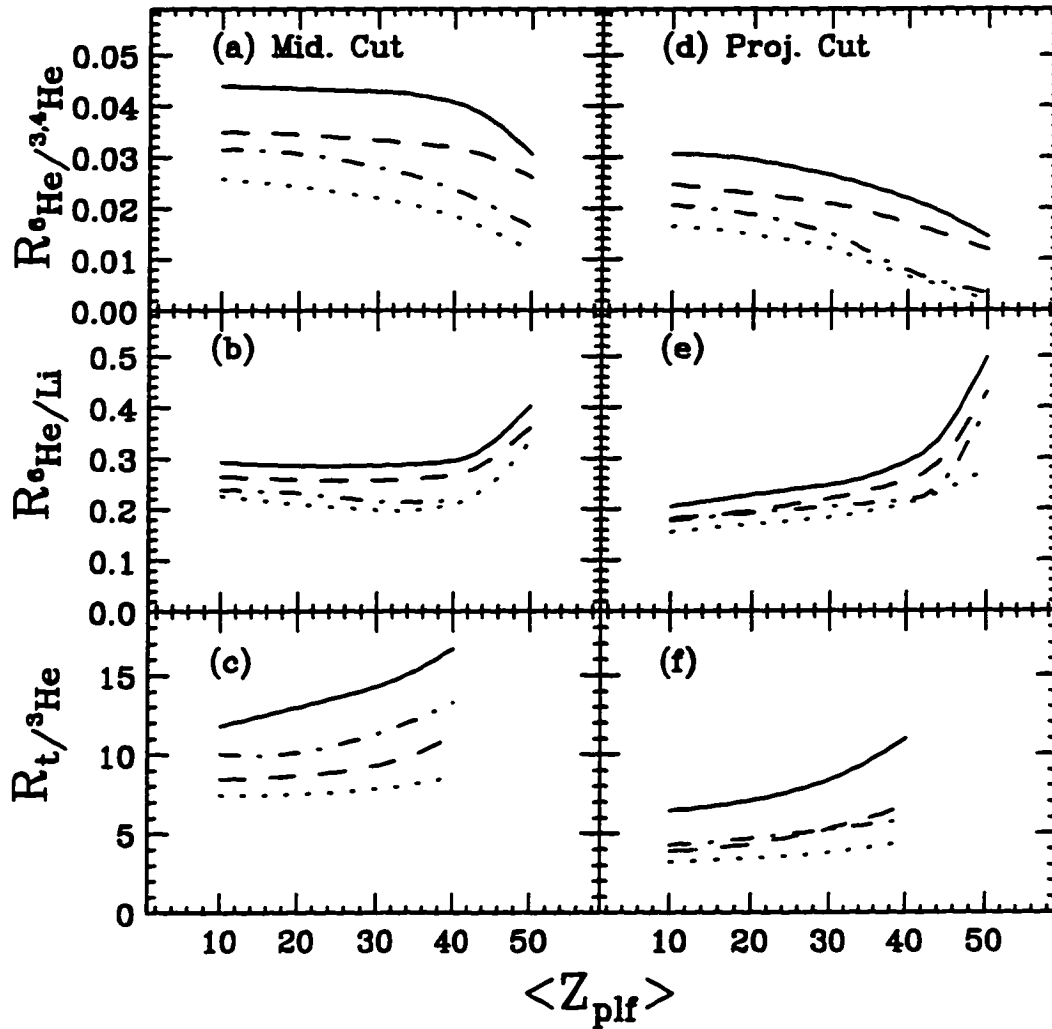


Figure 3.10: The relative yield of ${}^6\text{He}$ to ${}^{3,4}\text{He}$, ${}^6\text{He}$ to Li , and t to ${}^3\text{He}$ are shown for the four systems for several gates on Z_{plf} . Sections (a), (b), and (c) display the ratios for the mid-velocity region, $0 \text{ cm/ns} < V_{par}(\text{centerofmass}) < 2.0 \text{ cm/ns}$, while sections (d), (e), and (f) display the ratios for the projectile region, $3.0 \text{ cm/ns} < V_{par}(\text{centerofmass}) < 7.0 \text{ cm/ns}$ for sections (d) and (e) and 4 cm/ns for section f). (The range had to be reduced for the last ratio due to the limitations imposed by the rather low t punch-through energy.)

the collisions studied in this work due to shorter PLF-TLF interaction times and the observed dominance of a binary reaction mechanism. The confirmation that charge-to-mass neutralization (neutralization is a less stringent condition than equilibration) does not generally occur in intermediate-energy heavy-ion reactions has been made prior to the present study by the work of Yennello et al.[67].

3.3.3 The N/Z Signature of IMFs and LCPs

From figures 3.9 and 3.10 we now note the following trends: a) all ratios increase as the neutron excess of the system increases from LL to LH and HL to HH, b) the fragments in the mid-velocity region are more neutron rich than are the fragments in the projectile region, and c) the isotopic ratio decreases as the value of Z_{plf} is increased while the isobaric ratios display the opposite trend. The trends with the value of Z_{plf} mentioned above is expected if the values of Z_{plf} are inversely related to the damped excitation energy. The observation that the fragments from the mid-velocity region are more neutron rich than they are in the projectile-velocity region seems to suggest that the mid-velocity source itself is more neutron rich than either the target or projectile sources. Noting that the bulk of the IMF yield is found in the mid-velocity region we find that multifragmentation has an “ N/Z signature”, i.e. the IMFs associated with multifragmentation are neutron rich relative to IMFs produced from PLF and TLF evaporation.

3.3.4 Summary

The N/Z of the emitted IMFs as functions of Z_{plf} or V_{par} are new observables investigated by this work. These new observables are a significant step toward a more complete description of the phenomenon of multifragmentation and provide new constraints to guide theoretical descriptions of the process. They confirm the expected lack of charge equilibration or neutralization for intermediate-energy collisions. The N/Z signature of IMFs (and LCPs) emitted from the center of mass is that they are significantly neutron rich as compared to fragments emitted from the projectile frame. The existence of a neutron-rich mid-velocity source itself is not the only possible explanation for this signature, a fact which will become apparent in light of statistical-model calculations, a subject to which we now turn our attention.

Chapter 4

Theoretical Models and Simulations

4.1 Statistical-Model Simulations

4.1.1 Standard Statistical Models: GEMINI

A standard statistical-model, in the language of the heavy-ion nuclear chemist or physicist, refers to a model which treats the decay of an equilibrated nucleus by a sequence of independent emissions. These models make the statistical assumption of the equipartition of states, and hence the probability of a particular decay occurring is inversely proportional to the total number of decays possible. Decay probabilities are then further governed by kinetic factors such as angular-momentum conservation and Coulomb-barrier penetration probabilities. Experimental measures of these governing quantities are incorporated in these models with the further assumption of detailed balance and the use of cross-section data for the corresponding inverse processes to the decays (fusion is taken to be the inverse process of emission, this is not obviously correct for complex fragments due to the existence of direct-reaction channels). Auxiliary models of nuclear properties are also incorporated into statistical de-excitation models in order to provide the density of states as a function of nucleon number, excitation, and spin.

The application of statistical models and concepts to describe excited nuclear systems is nearly as old as nuclear science itself and was first formulated by Weisskopf in 1937 [39]. The appropriateness of using statistical models follows from the fact that

(heavy) nuclei are complex many-body systems which have a large density of states at even the most modest excitations that can be produced experimentally in nuclear reactions. This is evidenced by the fact that even the excitation due to the capture of a low-energy neutron by an intermediate-mass nucleus ($A \approx 100$) leads to state densities on the order of 10^6 per MeV. Of course, the density of states is rapidly rising with excitation energy and the state densities found in intermediate-energy heavy-ion collisions are many orders of magnitude greater than this. Thus, we see that a statistical description of the de-excitation of heavy nuclei is not only appropriate, but necessary. While the assumption of equal probabilities for the occupation of states, aside from weighting factors, follows quite simply from a picture where the constituents of the nucleus comprise a closed and equilibrated system, the assumption of detailed-balance is not so easily understood. The problem lies in the fact that the decay processes are actually irreversible, a situation that renders the detailed balance condition questionable. Alexander et al.[68] have argued, however, that the assumption of detailed balance yields a result that is equivalent to a transit-state logic, if the detail balance is assumed to be between "decision-point" configurations (those points where a daughter nucleus and various fragments are formed) and the rest of the configuration space for the nuclear system. In this argument the density of states accessible is defined by the decision-point configurations. Despite any reservations one may have toward the underlying assumptions of these models, they are viable models in that they have enjoyed large success in describing the de-excitation of compound nuclei formed in low-energy heavy-ion collisions.

When such models are applied to describing nuclear reactions products, the validity of the approach (and sometimes its success) relies on the ability of the experimentalist to deduce not only the presence of a source nucleus, but its excitation, spin, and composition as well. It is not surprising, then that these models have found their greatest success in predicting reaction products from lower-energy compound nucleus fusion-fission reactions. In the intermediate-energy regime, where the relative kinetic energy between the projectile and target is sufficient to disintegrate the entire system into its constituent nucleons and fusion residues are not observed for $\geq 90\%$ of the reaction cross section, applying these models becomes more of a challenge. As mentioned in the introduction, fragment production which is driven by dynamic processes need not reflect a statistical distribution at all. In light of these considerations, statistical models were used mainly to provide qualitative trends that

could illuminate which properties of an equilibrated source would be necessary to reproduce the experimental observations recorded in this study.

The statistical-model code GEMINI[69] uses a Monte-Carlo procedure to determine the decay sequence of an excited nucleus via the Hauser-Feshbach formalism[70] for light-ion emission and a variant of the Bohr-Wheeler[71] transition-state formalism for fission. For this study, the code was modified by its author (R.J. Charity) to include all known states for fragments with $Z \leq 4$, $A \leq 11$, and decay width $\Gamma \leq 1.5$ MeV in the Hauser-Feshbach decay formalism. This treatment included particle unbound fragments such as ${}^5\text{Li}$ and ${}^7\text{He}$. Fragment formation via the Bohr-Wheeler formalism was not implemented in the present study. In the Hauser-Feshbach formalism, an ensemble of equilibrated nuclei with initial excitation energy $E_i + \delta E_i$ and spin J_i is considered. The partial decay width for emitting a particle in state q with energy ϵ and spin s to produce daughter nuclei with excitation energy $E_f + \delta E_f$ and spin J_f is given by;

$$\Gamma_{\text{partial}}^{\epsilon,s} = \sum_{j=|J_i-J_f|}^{J_i+J_f} \sum_{l=|j-s|}^{j+s} \int_{-\infty}^{+\infty} d\chi g(\chi) T_l(E_i - E_f - B - \chi) \frac{\rho(E_f, J_f)}{\rho(E_i, J_i)}, \quad (4.1)$$

where j is the channel angular momentum, $g(\chi)$ is the line shape of the state of the emitted fragment, $T_l(\epsilon)$ is the ingoing-wave boundary-condition (IWBC) model transmission coefficient as a function of emitted particle energy $\epsilon = E_i - E_f - B - \chi$, $\rho(E_i, J_i)$ is the density of states of the initial nucleus as a function of excitation energy and spin, $\rho(E_f, J_f)$ is the density of states of the final nucleus, B is the separation energy of the particle q , and l is the decay-channel orbital angular momentum. The total decay width for emitting particle q is then,

$$\Gamma_{\text{total}}^q = \sum_{J_f} \int dE_f \Gamma_{\text{partial}}^{\epsilon,s}, \quad (4.2)$$

where the summation is over all allowed J_f . The total rate of emission from all decay channels is found by summing over all decay channels q .

$$R = \frac{\hbar}{\sum_q \Gamma_{\text{total}}^q} \quad (4.3)$$

Finally the probability of emitting a particle q with energy ϵ is given by the expression

$$P(q, \epsilon) = \frac{\Gamma_{\text{partial}}^{\epsilon, s}}{\sum_q \Gamma_{\text{total}}^q}. \quad (4.4)$$

Random probabilities are then generated to determine the evolution of a single excited nucleus, calculating new emission probabilities after each decay, until the initial excitation and angular momenta are exhausted to the point where particle emission is no longer probable. This process is repeated thousands of times so that the average properties of the decaying nucleus and its emitted fragments are determined.

The physically important ingredients for this model are the IWBC transmission coefficients ($T_l(\epsilon)$) and the density of states ($\rho(E_i, J_i)$) as a function of excitation energy, spin, and nucleon number.

The IWBC transmission coefficients ($T_l(\epsilon)$, defined as a function of particle energy for a given l -wave) give kinetic scaling factors which weigh the emission (absorption) probability of a given fragment from a given parent (daughter) nucleus. These factors are derived for each particle type considered for emission from all possible daughter nuclei. The IWBC transmission coefficients used in GEMINI are calculated with the prescription of Landowne and Pieper[72]. In these calculations, effective interaction potentials are taken as the real part of Optical-Model potentials. The Optical-Model potential has the following form

$$U(r) = V_c - Vf(x_0) + \left(\frac{\hbar}{m\pi c}\right) V_{so}(\sigma \cdot l) \frac{1}{r} \frac{d}{dr} f(x_{so}) - i \left[Wf(x_w) - 4W_D \frac{d}{dx_D} f(x_D) \right], \quad (4.5)$$

where

$$V_c = \begin{cases} \frac{Z_1 Z_2 e^2}{r} & r \geq R_c \\ (Z_1 Z_2 e^2 / 2R_c) (3 - r^2/R_c^2) & r \leq R_c \end{cases}, \quad (4.6)$$

$$R_c = r_c (A_1^{1/3} + A_2^{1/3}), \quad (4.7)$$

and

$$f(x_i) = (1 + e^{x_i})^{-1}, \quad (4.8)$$

with

$$x_i = (r - r_i (A_1^{1/3} + A_2^{1/3})) / a_i. \quad (4.9)$$

The parameters V , r_0 , a_0 , V_{so} , r_{so} , a_{so} , W , r_W , a_W , W_D , r_D , and a_D are found with global fits to elastic scattering data for nuclei of masses A_i and charges Z_i [73]. The spin-orbit term is only included for spin $\frac{1}{2}$ particles (n,p,t, ^3He) and then only an average transmission coefficient, defined by

$$T_l^{ave}(\epsilon) = \frac{(l+1)T_l^{up}(\epsilon) + lT_l^{down}(\epsilon)}{2l+1}, \quad (4.10)$$

is stored for use in the simulation. For heavier fragments for which no fits exist the parameters are taken to be those of Li. The imaginary terms, $i \left[W f(x_w) - 4W_D \frac{d}{dx_D} f(x_D) \right]$, which are used in the Optical Model to account for loss of particle flux due to reactions, are then dropped and the real part of the potential is used to calculate the transmission. The wave function of the emitted (absorbed) particle is represented as a sum of angular-momentum eigenfunctions,

$$\Psi(r, \theta) = \sum_{l=0}^{\infty} \frac{u_l(r)}{r} P_l(\cos \theta) \quad (4.11)$$

where $P_l(x)$ is an l th order Legendre polynomial. The transmission is then calculated as a function of momentum k for a single l -wave channel, $T_l(\epsilon)$, via integration of Schrödinger's equation,

$$\frac{\partial^2 u_l(r)}{\partial r^2} + \left\{ k^2 - \frac{2\mu}{\hbar^2} U(r) - \frac{l(l+1)}{r^2} \right\} u_l(r) = 0, \quad (4.12)$$

starting from a point near the origin, well inside the attractive part of the potential, taken to be R_b . The boundary condition imposed on the solution near this point is given by the semi-classical relation (considered to be valid near R_b)

$$u_l(r) \propto \frac{1}{\sqrt{q_l(r')}} \exp \left[-i \int_{R_b}^r q_l(r') dr' \right] \quad (4.13)$$

where

$$q_l(r') = \left(k^2 - \frac{2\mu}{\hbar^2} U(r) - \frac{l(l+1)}{r^2} \right)^{1/2}. \quad (4.14)$$

This boundary condition ensures that there is only an incoming wave at R_b and there is no unwanted interference from reflected waves in the attractive part of the potential.

The partial wave is then propagated out through the the barrier. Due to the boundary condition in the interior of the internuclear potential the wave function which penetrates the barrier is exactly that part which is absorbed of an incoming wave. The ratio of the absorbed and reflected-wave amplitudes can then be determined, η_l , and is related to the phase shift, δ_l by $\eta_l = |\exp(2i\delta_l)|$.

The second main ingredient is a model for the density of states as a function of excitation energy, spin, and nucleon number. It is common practice in nuclear science to parameterize the state density of a nucleus $\rho(E, A, J)$ (as a function of excitation E , mass A , and spin J) in terms of the Fermi-gas state-density formula derived by Bethe in 1937[74] for a gas of noninteracting Fermions in a spherical potential well.

$$\rho(E) = \frac{e^{2\sqrt{aE}}}{12a^{1/4}E^{5/4}} \quad (4.15)$$

The parameter a is known as the “level-density parameter” and, for a gas of noninteracting Fermions in a spherical potential well, is given by

$$a = \frac{\pi^2}{6}g(\epsilon_F) \quad (4.16)$$

where $g(\epsilon_F)$ is a sum of the neutron and proton single-particle level densities evaluated at their respective Fermi energies. A similar functional form for the state density which includes angular momentum and is utilized in GEMINI can be found in Bohr and Mottelson [75],

$$\rho(E, J) = \frac{2J+1}{12} \sqrt{a} \left(\frac{\hbar^2}{2I}\right)^{3/2} \frac{\exp\left(2a\left(E - \frac{\hbar^2 J(J+1)}{2I}\right)\right)}{\left(E - \frac{\hbar^2 J(J+1)}{2I}\right)^2}, \quad (4.17)$$

where J is the spin and $I = \frac{2}{5}mR^2$ is the moment of inertia of a rigid sphere with radius R given by the empirical relation $R = r_o A^{1/3}$ (r_o taken as 1.2 fm). Inclusion of the influence of nuclear structure, quantal fluctuations, and thermal fluctuations on the state density is achieved by introducing a phenomenological mass and temperature dependence in the level density parameter a . The mass (A) dependence predicted for a Fermi gas in a spherical well is $a = A/15$, but is empirically found to be in the range of $A/8$ to $A/11$. In this study, the temperature-dependent parameterization of Ormand et al.[76] is utilized. In this scheme, a takes on values of $A/8$ at low

excitation and smoothly decreases to a value of $A/11$. This decrease of the level-density parameter is attributed to a decrease in low-lying collective shape vibrations with increasing excitation.

4.1.2 Expanding Evaporating Source Model

The Expanding Evaporating Source Model (EES) is a simplistic statistical model which describes the time evolution of an ensemble average of excited nuclear systems as they statistically emit particles. This model was included in this study due to its ability to consider many more decay channels than the otherwise more sophisticated statistical model GEMINI. Despite the fact that this model is only appropriate for systems with $J = 0$, EES includes the emission of all (75) ground-state and excited-state fragments with $Z \leq 10$, $A \leq 18$, and decay widths $\Gamma \leq 1.5$ MeV. These states were either included explicitly or, if the expected multiplicity was small, they were accounted for in an subsequent code which scaled excited state multiplicities to the ground state multiplicity by a Boltzmann weighting factor (omission of exotic fragments with multiplicities far less the total multiplicity has little effect on the evolution of the decaying nucleus). This model also includes the effects of thermal expansion and subsequent compression of the excited nucleus by altering the nucleon density of the evaporating nucleus[38], but this feature was not considered important to this work due to the large amounts of excitation required for thermal expansion to influence fragment multiplicities in the model (more than 7 MeV/A initial excitation energy).

The model is built about the double differential quantity $\frac{d^2 N_q}{dt dE}$ [77], which expresses the instantaneous rate of emission of a particle of type q with kinetic energy between E and $E + dE$. According to the Weisskopf detailed-balance procedure[39], this quantity is given by

$$\frac{d^2 N_q}{dt dE} = \frac{2s + 1}{\pi^2 \hbar^2} EM \sigma_q^f \frac{\rho(E_f)}{\rho(E_i)} \quad (4.18)$$

where s , M , and σ_q^f refer to the spin, mass, and the cross section for fusion of the particle q with the daughter of the decaying nucleus. The quantity $\rho(E)$ is the density of states as a function of excitation only, taken to have the precise form of equation 4.15. The ingredients of the right hand side of equation 4.18 are the physically

important parameters of the model. The cross sections for fusion are taken to be geometrical for neutrons

$$\sigma_n^f = \pi R^2 \quad (4.19)$$

and are modified by Coulomb repulsion for charged particles

$$\sigma_n^f = \pi R^2 \frac{E - V_c}{E} \theta(E - V_c), \quad (4.20)$$

where θ is the unit step function and V_c is the Coulomb-barrier height for touching charged spheres. This is equivalent to having angular-momentum independent transmission coefficients that linearly rise from zero at the Coulomb-barrier energy V_c to unity at $2V_c$. The expression $\frac{\rho(E_f)}{\rho(E_i)}$ is the ratio of the density of states in the final compound nucleus to the density of states in the initial compound nucleus (just as it was in equation 4.1). In this model, the level density and the level-density parameter a are taken to be the exact forms derived for an ideal Fermi gas (see equations 4.15 and 4.16). This expression for $\frac{d^2 N_q}{dt dE}$ is then integrated over energy to obtain the emission rates $\frac{dN_q}{dt}$ as a function of compound nucleus excitation. An instantaneous cooling rate $\frac{dT}{dt}$ then is determined by the ensemble averaged expression of the conservation of energy

$$\frac{dE_i}{dt} + \sum_q \left[\frac{dN_q}{dt} \right] B_q(A_i, Z) + \sum_q \frac{d(E_k)_b}{dt} = 0, \quad (4.21)$$

where $\frac{d(E_k)_b}{dt}$ is the average rate of change of kinetic energy carried away by the emitted fragment q and the daughter nucleus (note that $T = \sqrt{E^*/a}$, where E^* is the excitation energy). A discrete approximation of this equation is then evolved in time, calculating new values for $\frac{d^2 N_q}{dt dE}$ at small time intervals that account for the average loss of excitation energy and mass, until the initial excitation energy is depleted to the point where particle emission is no longer probable. Integration of the quantity $\frac{d^2 N_q}{dt dE}$ with respect to energy and time can then yield the energy spectrum $\frac{dN_q}{dE}$, emission rate $\frac{dN_q}{dt}$, and multiplicity N_q of the particle q .

EES was mainly used to evaluate the surviving fraction of primary IMFs for systems of different initial N/Z where the inclusion of particle-unbound states for heavier fragments was important. The results of this model were found to be in fair agreement with the results of GEMINI except for very large initial excitation energies per nucleon (≥ 7.5 MeV/A).

4.1.3 Comparison of Statistical Models and Data

Figure 4.1 shows values of the ratios $R_{6/4}$, $R_{6/Li}$, and $R_{3/3}$ calculated by GEMINI and EES. The left hand side of this figure (a, b, and c) shows the ratios as a function of the initial excitation energy per nucleon for ^{136}Xe and ^{124}Xe sources while the right hand side (d, e, and f) shows the dependence of these ratios on fragment size ($\eta = A_{source}/A_{total}$) with a fixed N/Z ratio, taken to be that of ^{136}Xe . Both codes treat the formation and sequential decay of all isotopes of H, He, Li, and Be. The results of these two codes agree with one another reasonably well and the calculated values of $R_{3/3}$ approach the value expected for coalescence, at the largest excitation energies. Despite this agreement, it would be a mistake to believe that these statistical expectations are robust in the accurate prediction of the yields of loosely bound particles. Previous work on the statistical emission of d's and t's indicates that both direct reaction data and fusion data are needed to accurately calculate transmission coefficients[78]. Not surprisingly these calculations do not provide a quantitative explanation of the experimental data presented in the previous chapter. On the other hand, the calculations do account for some trends seen in the data and, in doing so, provide considerable insight into the sources of these fragments. As expected, the calculated trend of the isotopic ratio with excitation energy is opposite to that of the isobaric ratios. The explanation of both trends is that the barrier or separation energy determines the yield at low excitation energy and the influence of these quantities diminishes as the excitation energy is increased. The observed trends with Z_{plf} (figure 3.10) are then readily explained as long as one accepts that the thermalized energy increases as the value of Z_{plf} decreases, a reasonable contention supported by the fragment multiplicities (see figure 3.3).

Less obvious than the explanation of the trends with Z_{plf} is the explanation for the observed increase in the yield of neutron-rich fragments as V_{par} is decreased from the projectile-velocity region to that of the center-of-mass region. This observation has been made previously for the isotopes of H, and is reminiscent of the charged particles which accompany low-energy fission. After α -particles, t's are the most prevalent light charged particle which accompanies fission.[44] If one tries to explain the observed trends utilizing statistically emitting sources of the same size and charge-to-mass ratios in the mid-velocity and projectile-velocity regions, then the isobaric ratios imply that the mid-velocity source has a lower excitation energy/nucleon than the projectile-like source. This explanation is inconsistent with all reasonable

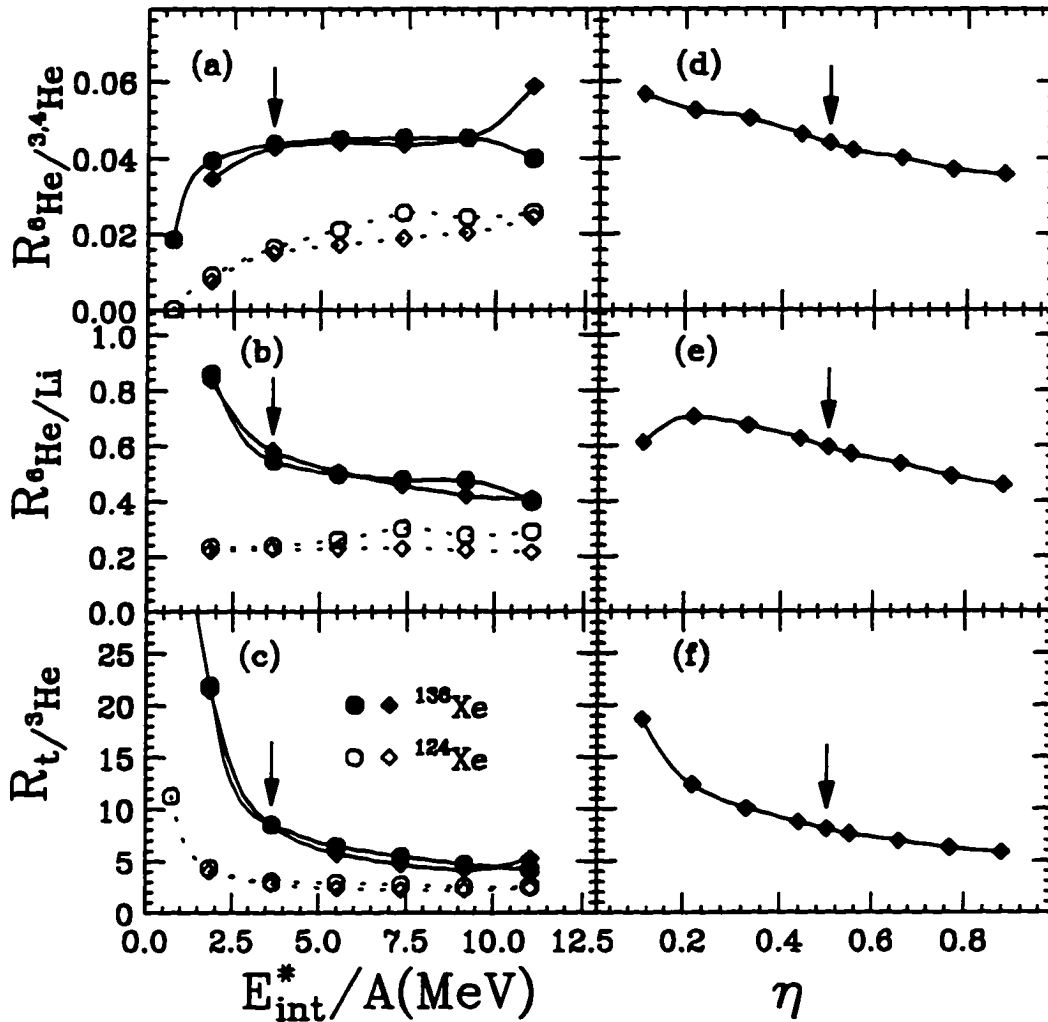


Figure 4.1: The results of statistical-model calculations for the decay of excited ^{136}Xe and ^{124}Xe projectiles as a function of the initial excitation energy per nucleon (a), (b), and (c) and fragment size $\eta = A_{source}/A_{total}$ at fixed charge-to-mass ratio (d), (e), and (f). In the latter case, the charge-to-mass ratio is that of the H projectile, ^{136}Xe , and the initial excitation energy per nucleon is 3.68 (arrow on left.) The circles are the results from GEMINI calculations and the diamonds are the results from EES. The key for the lines is the same as that used in the previous figures.

reaction models and with kinetic “temperatures” (extracted from the transverse energy spectra) which are larger in the mid-velocity region (~ 20 MeV) than in the region of velocity around that of the projectile (~ 10 MeV). Differences in source angular momentum were also considered by adding $50\hbar$ of initial angular momentum to the Xe fragments. This was found to have little to no effect on the ratios as the first emitted IMF was likely to carry away much of this angular momentum as orbital angular momentum.

Two possibilities remain to explain these observations. The first, and obvious one, is that the isotope ratios in the mid-velocity region are enriched in neutron-rich isotopes because the source material is neutron rich relative to the source matter which is represented by the emissions in the projectile region (in either the HH or LL systems). A second possibility is investigated on the right-hand side of figure 4.1, which displays EES predictions for the various ratios under study as a function of $\eta = A_{source}/A_{total}$, for a fixed charge-to-mass equal to that of ^{136}Xe . The ratios increase as η decreases thus providing an argument that the mid-velocity sources can have the same charge-to-mass ratio as the overall system as long as these sources are always smaller than the source in the projectile-velocity region. In this case the mid-velocity sources are not neutron rich relative to the bulk matter but they are neutron rich relative to the valley of β -stability, which moves toward symmetry as the size of the system is diminished. Needless to say, this case argues against a single large mid-velocity source, just as the elongated emission patterns in the Galilean-invariant plots do.

A more elementary testing ground for model calculations than these isotopic and isobaric ratios are the values of N_n/N_c as a function of Z_{plf} or the dependence of $\langle N_n \rangle$ on N_c as shown in figure 3.2. Statistical-model calculations have been performed assuming three source regions (with the target, center-of-mass, and projectile velocities) in which we have fixed the total mass in each region by partitioning the mass of the total system as indicated by the Galilean-invariant cross-section maps. These calculations were corrected for both the neutron tank efficiency and MINIWALL/MINIBALL thresholds. These calculations reproduce the general trend of $\langle N_n \rangle$ with N_c (with both values increasing with increasing excitation energy per nucleon) however the results are sensitive to the prescription for the level-density constant a and the number of sources contributing to each region. Including variation of these quantities, the exercise of reproducing the dependence of $\langle N_n \rangle$ on N_c is under

determined. For example using a small level-density parameter, a , suppresses neutron emission and enhances the production of particles with large separation energies. Likewise, a variation of a with a temperature-dependent prescription for reducing a from $A/8$ to $A/11$ via the smooth temperature-dependent prescription suggested by Ormand et al.[76] reduces the neutron yield by about 20% from the yield expected for $a = A/8$. Furthermore decreasing the source size (from $\eta = 1$ to 0.25), and thus increasing the number of sources, increases the $\langle N_n \rangle$ to N_c ratio (for the same reason that the isotope and isobaric ratios increased with decreasing η). These calculations indicate that while there is not a unique prescription to reproduce the experimental data, multiple sources are needed to produce enough free neutrons if the level-density parameter a is either small ($A/11$) or temperature dependent.

These statistical-model calculations can also be used to investigate the significance of the observation made in the previous chapter, that the maximum values of $\langle N_{imf} \rangle$ increase with neutron excess. This might very well be only the result of the improved survivability (retention of IMF status) of the more neutron-rich primary fragments which will result from the sequential decay of the neutron-rich systems. However, if the differential survivability can not explain the entire difference it is possible that this difference, in some measure, reflects the relative cost of density reduction in matter of different charge-to-mass ratios. To address this issue the IMF “survivability” is calculated. The IMF “survivability” is defined as the percentage of primary IMF’s produced which retain their IMF status, $Z > 2$, after sequential decay. The results from EES using sources of ^{136}Xe and ^{124}Xe are presented in figure 4.2. The production and sequential decay of elements with $Z \geq 5$ are treated in less detail than those with $Z \leq 4$, however with increasing Z and A the survivability, retention of IMF status, is quite high. This fact coupled with the decreasing yield with increasing Z_{imf} make the detailed treatment of the heavier fragments not relevant to the survivability question. In this representative calculation the difference in the surviving fraction (long dashed line) is predicted to be in the range of 30% to 10% of the total fraction of surviving IMF’s. This is a substantial difference, not dissimilar to the difference in the data, and thus we must conclude that most, if not all, of the observed difference results from the action of sequential decay.

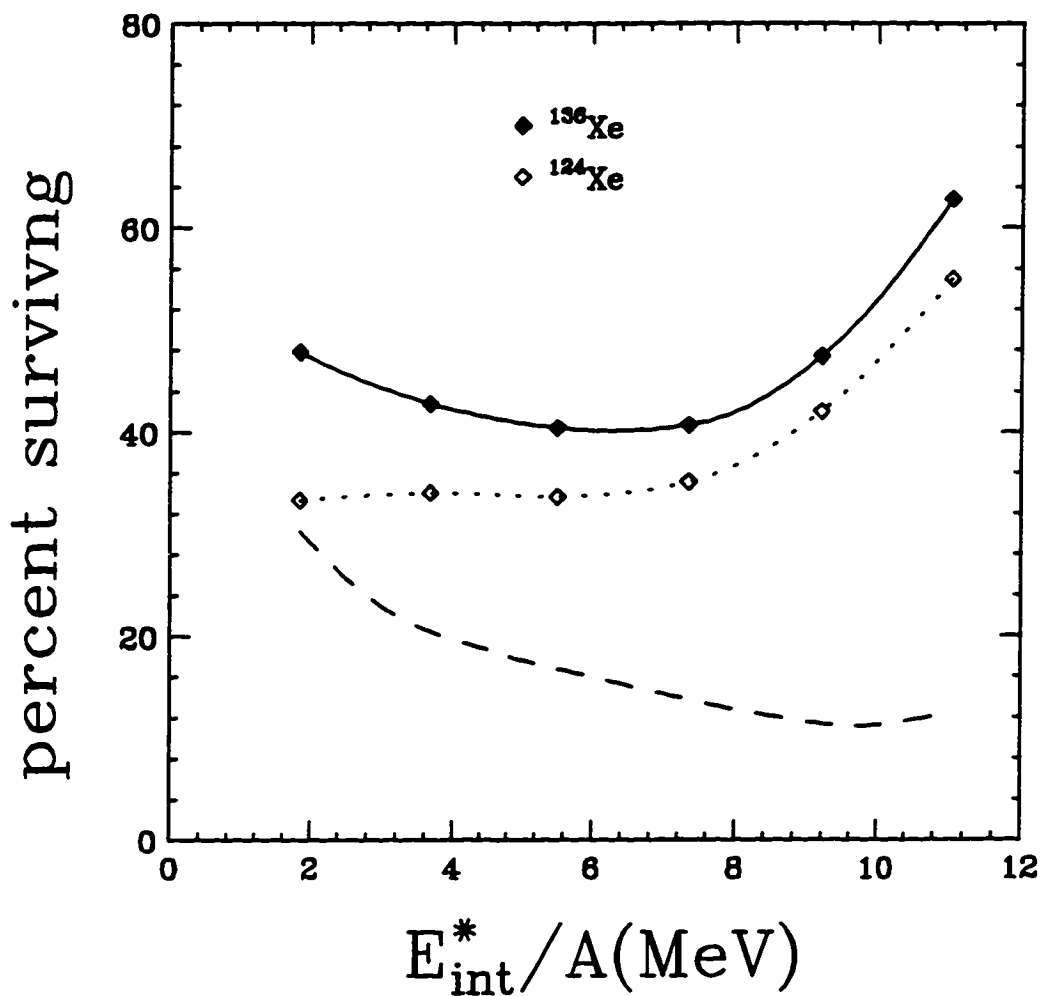


Figure 4.2: Statistical-model predictions (EES) of the percentage of IMFs which survive sequential decay and retain their IMF status as a function of the initial excitation energy per nucleon in the system (E_{int}^*/A [MeV]). The solid line connects results for a ^{136}Xe source while the dotted line connects the results for a ^{124}Xe source. The dashed line is the percentage difference in the survivability between the ^{136}Xe source and the ^{124}Xe source.

4.1.4 Summary

Possible explanations for the neutron enrichment of IMFs and LCPs that are emitted in the mid-velocity region have been explored by considering the conditions under which statistically emitting sources could qualitatively reproduce the trend. It has been shown that differences in initial excitation or angular momentum can not explain the observed neutron richness of fragments found in the mid-velocity region. It was found, however, that the existence of sources that are smaller (or have extended surface area) in the mid-velocity region than the source(s) in the projectile-velocity region could qualitatively explain the trend. The production of small elongated sources is also observed in solutions of the BUU transport equation (see figure 1.1). This observation shows that the prediction of N/Z observables by statistical models are quite sensitive to the geometry of the excited matter. These statistical-model simulations have provided some valuable insight into this new N/Z observable but a truly satisfactory explanation will have to be found elsewhere.

An attempt to reproduce the values of N_n/N_c as a function of Z_{plf} or the dependence of $\langle N_n \rangle$ on N_c with statistical-model calculations was performed. The exercise of reproducing the dependence of these quantities was found to be very sensitive to the prescription of the level-density parameter a and hence under determined.

The differences observed in the increasing maximum value of $\langle N_{imf} \rangle$ with increasing N/Z of the system were also studied within the framework of the statistical model. It was found that this trend can be completely explained by differences in the survivability of the primary IMFs. This difference in the survivability can be understood as a consequence of the increase probability for neutron-rich IMFs to be produced from a neutron-rich system coupled with the increased probability that these IMFs will emit neutrons during sequential decay and thus preserve their IMF status, $Z \geq 3$.

4.2 Dynamical Reaction Simulations

4.2.1 The BUU Transport Equation

The ultimate goal for the dynamical description of intermediate-energy heavy-ion collisions is the solution of the many-body Schrödinger equation. The nature of the Hamiltonian necessary to reproduce the measured observables from these collisions

could then illuminate the relevant physics. Unfortunately, finding a solution of this equation is presently an intractable problem. To develop a more tractable model, one can take a statistical approach and consider the time evolution of the n-body phase-space distribution $f^n(\vec{r}_1, \dots, \vec{r}_n, \vec{p}_1, \dots, \vec{p}_n, t)$, which describes the probability of finding the system at a given phase point $\{\vec{r}_1, \dots, \vec{r}_n, \vec{p}_1, \dots, \vec{p}_n\}$ at a time t . This problem, however, has a complexity that rivals the complexity of the Schrödinger equation so that further simplification must be made. Enormous simplification can be made by assuming,

$$f^n(\vec{r}_1, \dots, \vec{r}_n, \vec{p}_1, \dots, \vec{p}_n, t) = \prod_{i=1}^n f(\vec{r}_i, \vec{p}_i, t),$$

which approximates the n-body phase-space distribution, $f^n(\vec{r}_1, \dots, \vec{r}_n, \vec{p}_1, \dots, \vec{p}_n, t)$, as a product of single-particle phase-space distributions, $f(\vec{r}, \vec{p}, t)$. With this assumption one needs only to evolve the single-particle phase-space distribution, which is a tractable problem when treated semi-classically. While such a description necessarily neglects the many-body and quantal features of the system, it can provide a useful qualitative description of intermediate-energy heavy-ion collisions.

The Boltzmann-Uehling-Uhlenbeck (BUU) transport equation, is an integro-differential equation for the time evolution of the classical one-body phase-space distribution function $f(\vec{r}, \vec{p}, t)$, corresponding to the classical limit of the Wigner function. The equation is derived from the fact that the single-particle phase-space distribution $f(\vec{r}, \vec{p}, t)$ obeys the following equation of continuity,

$$\frac{\partial f}{\partial t} + \frac{\vec{p}}{m} \frac{\partial f}{\partial \vec{r}} + \vec{F} \frac{\partial f}{\partial \vec{p}} = 0. \quad (4.22)$$

The force \vec{F} which appears in this equation is logically divided into two components

$$\vec{F} = \vec{F}_{ext} + \vec{F}_{2-body}, \quad (4.23)$$

where \vec{F}_{ext} is an "external" force derived from a mean field $U(\vec{r})$ and is replaced by the expression $\vec{F}_{ext} = -\frac{\partial U(\vec{r})}{\partial \vec{r}}$ while \vec{F}_{2-body} is a force associated solely with two-body collisions and is replaced by the Boltzmann ansatz with the modification provided by

Uehling and Uhlenbeck[79]

$$\begin{aligned} \vec{F}_{2\text{-body}} \frac{\partial f}{\partial \vec{p}} = & \int \frac{d^3 \vec{p}_2 d^3 \vec{p}_1 d^3 \vec{p}_2'}{(2\pi)^6} \frac{|\vec{p}_1 - \vec{p}_2|}{m} \sigma(\vec{p}, \vec{p}_2 \leftrightarrow \vec{p}_1, \vec{p}_2') \\ & \times \{ f(\vec{r}, \vec{p}, t) f(\vec{r}, \vec{p}_2, t) (1 - f(\vec{r}, \vec{p}_1, t)) (1 - f(\vec{r}, \vec{p}_2', t)) \\ & - f(\vec{r}, \vec{p}_1, t) f(\vec{r}, \vec{p}_2', t) (1 - f(\vec{r}, \vec{p}, t)) (1 - f(\vec{r}, \vec{p}_2, t)) \} \\ & \times \delta^3(\vec{p} + \vec{p}_2 - \vec{p}_1 - \vec{p}_2') \end{aligned} \quad (4.24)$$

The important ingredients in this model are the mean field $U(\vec{r})$ and the scattering cross section $\sigma(\vec{p}, \vec{p}_2 \leftrightarrow \vec{p}_1, \vec{p}_2')$. The mean field is commonly parameterized as a density functional

$$U(\rho(\vec{r})) = \alpha \left(\frac{\rho(\vec{r})}{\rho_o} \right) + \beta \left(\frac{\rho(\vec{r})}{\rho_o} \right)^\gamma, \quad (4.25)$$

where α , β , and γ are determined by fixing the nuclear compressibility, $\kappa = 9\rho^2 \left(\frac{\partial^2 E/A}{\partial \rho^2} \right)$, the volume binding energy per nucleon of symmetric nuclear matter $E/A = -15.75 \text{ MeV}$, and the condition that the binding energy is a minimum, $\partial(E/A)/\partial \rho = 0$, at $\rho = \rho_o$ (this will be discussed in more detail in section 4.3). Popular choices of α , β , and γ are given in table 4. The only physically important difference between these parameter sets is the chosen value of the nuclear compressibility, κ (SOFT: $\kappa = 200$, MEDIUM: $\kappa = 235$, HARD: $\kappa = 380$). An isospin-dependent mean field which produces neutron skins, was recently proposed by Sobotka[47],

$$U_n = 8a \frac{\rho_n}{\rho_o} + 4ab \frac{\rho_p}{\rho_o} + 8c \frac{\rho_n \rho_p}{\rho_o} + 4c \left(\frac{\rho_p}{\rho_o} \right)^2 \quad (4.26)$$

and

$$U_p = 8a \frac{\rho_p}{\rho_o} + 4ab \frac{\rho_n}{\rho_o} + 8c \frac{\rho_n \rho_p}{\rho_o} + 4c \left(\frac{\rho_n}{\rho_o} \right)^2, \quad (4.27)$$

where U_n is the mean field experienced by neutrons, U_p is the mean field experienced by protons, ρ_o is the saturation nuclear density, ρ_n is the neutron density, and ρ_p is the proton density. This mean field is parameterized such that it reduces to the STIFF mean field for symmetric nuclear matter and is termed the ISOSTIFF mean field. The asymmetry-dependent term of this mean field was also added to the SOFT mean field to produce another mean field that reduces to the SOFT mean field for symmetric matter and is termed the ISOSOFT mean field. The scattering cross

section $\sigma(\vec{p}, \vec{p}_2 \leftrightarrow \vec{p}_1, \vec{p}_2)$ is normally taken as the free-space nucleon-nucleon cross section, σ_{NN}^{free} .

The numerical implementation of the simulation used in this work[80] employs the “test-particle method”[81]. The simulated phase space is divided into N small cells which obey the semiclassical equations of motion:

$$\frac{\partial \vec{p}_i}{\partial t} = -\vec{\nabla}_{\vec{r}} U(\vec{r}_i) + \sum_{j \neq i} \frac{q_i q_j}{(\vec{r}_i - \vec{r}_j)^2} \quad (4.28)$$

and

$$\frac{\partial \vec{r}_i}{\partial t} = \frac{\vec{p}_i}{\sqrt{m_i^2 + p_i^2}} \quad (4.29)$$

where

$$i = 1, \dots, (A_t + A_p) \sim N \quad (4.30)$$

$q_{i,j}$ is the charge of the i th or j th particle, m_i is the mass of the nucleon, A_t is the mass of the target, A_p is the mass of the projectile, and N is the total number of test particles in a single simulated event. The solution of these equations of motion provides a time-evolving distribution of “test particles” which are then related to the single-particle phase-space distribution by

$$f(\vec{r}, \vec{p}, t) = \sum_{\text{events}} \sum_{i=1}^N \delta(\vec{r}_i - \vec{r}) \delta(\vec{p}_i - \vec{p}), \quad (4.31)$$

where the summation over events indicates that the system may be evolved with many sets of randomly-chosen initial “test-particle” distributions. The collision integral on the right hand side of equation 4.24 is included in the following way. Two “test particles” are considered to have the opportunity to collide if their minimum distance is found to be less than $R_{min} = \sqrt{\frac{\sigma(\vec{p}, \vec{p}_2 \leftrightarrow \vec{p}_1, \vec{p}_2)}{\pi}}$. Two such “test particles” are then considered to stochastically scatter with new momenta (which are energy and momentum conserving) being chosen at random. Then the “Pauli blocking factors” of equation 4.24, $(1 - f(\vec{r}, \vec{p}_1, t))(1 - f(\vec{r}, \vec{p}_2, t))$ and $(1 - f(\vec{r}, \vec{p}, t))(1 - f(\vec{r}, \vec{p}_2, t))$ are evaluated in a Monte-Carlo fashion. Random probabilities are generated to determine if the four phase-space cells of the colliding particles are occupied. If the phase-space cells are found unoccupied the collision is allowed to occur, otherwise the system evolves as if no interaction had taken place.

Table 4.1: Commonly Used EOS Parameters for BUU Simulations

EOS	α MeV	β MeV	γ	κ MeV
SOFT	-358.7	304.6	7/6	200
MEDIUM	-218.2	164.0	4/3	235
HARD	-124.4	70.3	2	380

4.2.2 Comparison of Dynamical Models and Data

The results of the statistical-model simulations of the last section compared with the experimental observations made a qualitative argument for a reaction picture which produces a string of small emitters with intermediate velocities. It has already been mentioned there that solutions to the BUU transport equation produce intermediate-velocity (“neck-like”) sources[46]. As a point of interest it should be noted that TDHF calculations[82] and macroscopic dynamical models[83] can also produce “neck” fragments and exhibit similar scenarios, although the BUU simulations are generally considered more appropriate to the energy region of the present study due to their treatment of two-body collisions. BUU simulations have therefore been performed for the systems studied in the present work.

The striking feature of these calculations, in comparison to the experimental data, is the excessive amount of the velocity damping, compare figure 3.6 a) with figure 4.3 a). The data have a negligible cross section (less than 100 mb) for the production of PLFs with values of E/A less than 40 MeV while the calculations predict large cross sections (as much as 1 b) in this energy region. This discrepancy is largest if a STIFF equation of state is used ($\kappa = 380$ MeV), smaller with a SOFT equation of state ($\kappa = 200$ MeV), and still smaller if the N/Z degree of freedom is modelled in a fashion which allows for stable neutron skins (ISOSPIN-SOFT). The decreased damping (in going from STIFF to SOFT for example) is accompanied by an increase in the mass contained in fragments with velocities intermediate between the projectile and the target. This is shown in figure 4.3 (b). It is also accompanied by a general increase in the multiplicity of fragments from the neck region.

Unfortunately, this trend must be considered qualitative because this fragmentation has much to do with the numerical implementation of the BUU equation. The

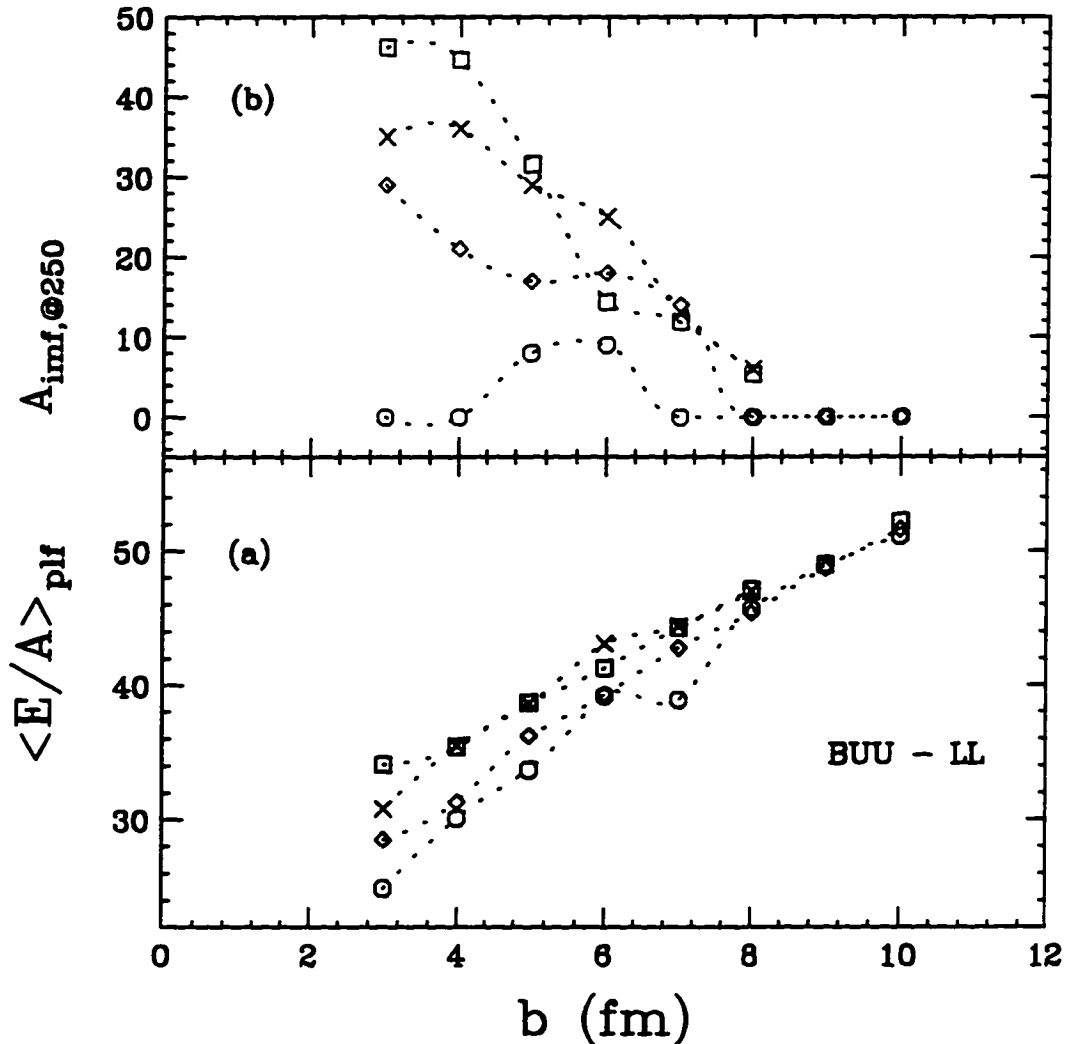


Figure 4.3: The results of BUU calculations for (a) the exit channel value of E/A for the projectile-like fragment and (b) the mass contained in mid-velocity IMFs at 250 fm/c. The circles show the results for a stiff ($\kappa = 380$ MeV) equation of state, the diamonds show the results for a soft ($\kappa = 200$ MeV) equation of state, the X's show the results for the ISO-SOFT equation of state which has an improved treatment of the isospin (N/Z) degree of freedom, and the squares show the results for the iso-soft equation of state when the scattering cross sections have a density-dependent reduction.

simulation provides a single-particle phase-space distribution that evolves with time and the inference of clusters in this distribution is not rigorous. It is therefore concluded that calculations of this sort come closer to reproducing the experimental data when the cost of creating reduced-density material is reduced. (This holds for SOFT versus STIFF and ISOSPIN-SOFT versus SOFT.) Reduction in the velocity damping can also be accomplished by reducing the nucleon-nucleon cross section. However, even with a density-dependent reduction which reduces the cross sections by 20%[84] at the saturation density and the isospin-dependent Soft equation of state, the damping is still excessive, as is seen in figure 4.3 (A further decrease in the nucleon-nucleon cross sections would further diminish this discrepancy).

Perhaps more germane than the equation of state or the in-medium cross section is the neglect of quantal effects and fluctuations in these simulations. The implementation of BUU utilizing the test-particle method has been shown to produce a phase-space distribution of particles which is a linear combination of Fermi and Maxwell distributions, indicating that the Pauli-Blocking mechanism of the model falls short of its aim[85]. The single-particle nature of the BUU model may also be a limitation that may be remedied by the inclusion of a stochastic term in the mean field. It is possible that the failure cited above results from one or both of these omissions, a possibility which must be tested with improved models. We have verified that momentum-dependent potentials have little affect on the observables presented above at the energy of the present study. Furthermore, it should be mentioned that the results for the LL system were chosen for display because the mass uncertainty for experimental data is smallest there. If the experimental masses (for a given charge) are less than assumed, then the experimental E/A values would be even larger (implying even less velocity dissipation) than those shown in figure 3.6 (a.).

4.2.3 Inclusion of Light-Cluster Degrees of Freedom

Although there are problems associated with the prediction of fragment formation in the framework of BUU transport simulations, basically looking for correlations in a single-particle model, some progress has been made toward the inclusion of light-cluster degrees of freedom in the dynamics. A transport model recently developed by Danielewicz and Bertsch[86, 87] includes explicit deuteron and $A = 3$ -cluster degrees

of freedom and is based on non-equilibrium many-body theory in the quasiparticle limit. The resulting transport equations for nucleons and clusters have a Vlasov-like left-hand side, like the BUU equation, but have a modified collision term on the right-hand side which contains production and absorption rate terms which take into account the Boson or Fermion character of the given cluster. Another refinement in this model is that the “Pauli-Blocking” of collisions between nuclei is isospin dependent (only particles with the same isospin projection block each other). Furthermore, the production of a composite particle (d,t,or ^3He) is suppressed if the average nucleon occupation over a volume in momentum space corresponding to the composite wavefunction exceeds a phenomenological cutoff (0.3). This produces a suppression of cluster formation due to the effect of Pauli Exclusion.

In principle a BUU-like transport simulation with an isospin-dependent potential might have the proper physics to qualitatively explain the N/Z signature of multifragmentation. To explore this possibility, the transport model of Danielewicz and Bertsch was implemented for collisions of ^{136}Xe and ^{124}Xe at 55 MeV/nucleon. The simulation was first run with an isospin-dependent equation of state (linear potential dependence), with and without Coulomb interactions, ignoring the light-cluster degrees of freedom. While the formation of “neck”-like structures were observed, there was no significant enhancement in the neutron richness of the mid-velocity region. In the next section, it will be shown that at equilibrium a large enhancement of neutron matter would be expected in the low-density regions of the neck. That this is not realized here is not surprising considering that the collisions take place in less than 150 fm/c or 4.5×10^{-21} s. When the light-cluster degrees of freedom were considered, it was found again that no associated enhancement in the neutron richness of the mid-velocity region was produced, however if one considered only nucleons that were *not* bound in light clusters then a significant enhancement was produced. This trend is displayed in figure 4.4 where 3 snap shots of the total, neutron, and proton densities are displayed along with N/Z ratios for both free and total (free and clustered) nucleons along the separation axis of the PLF and TLF. This effect is due to a predominant clustering of deuterons in the low-density regions of the colliding system. The far left panels display the N/Z ratios and it is easily seen that the neck and surface regions are rich in unbound neutrons.

In order to pursue this scenario any further toward explaining the neutron richness of fragments in the mid-velocity region one must step outside the model and

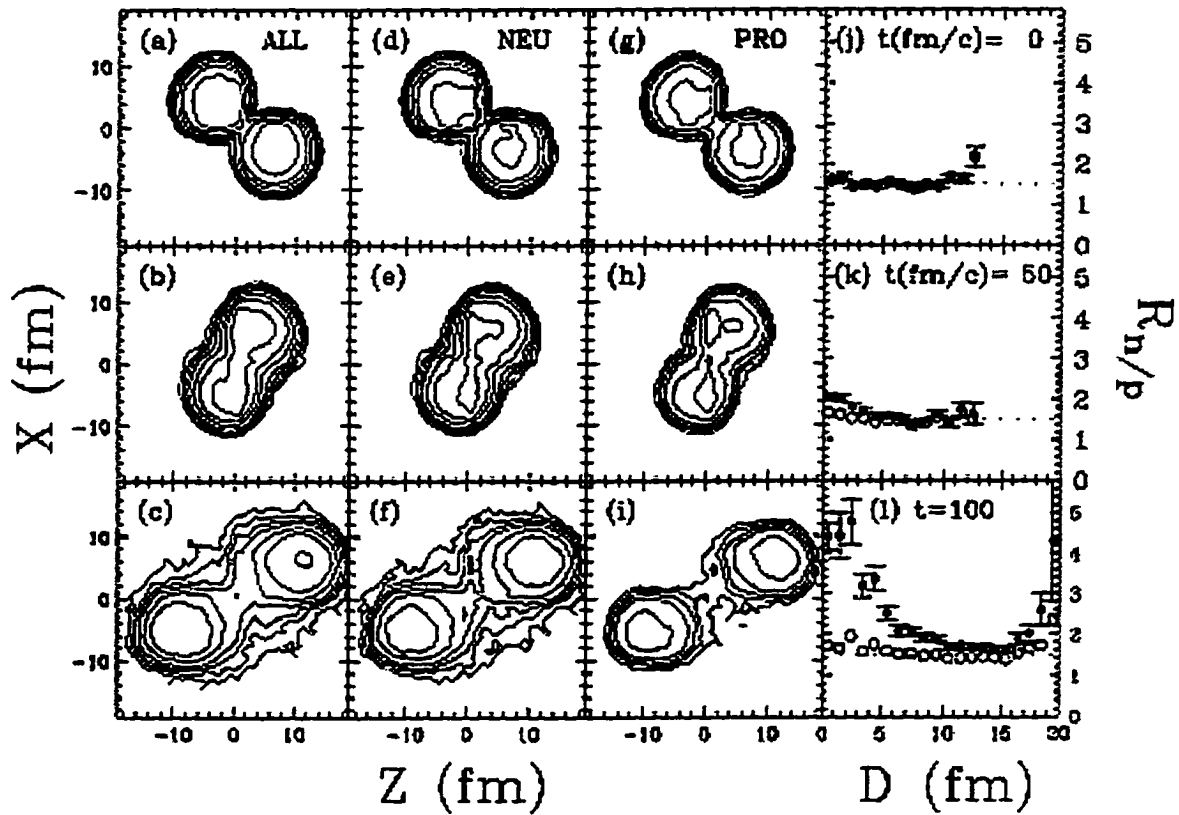


Figure 4.4: BUU simulation of a collision at an impact parameter of 8.8 fm between ^{136}Xe and ^{124}Xe at 55 MeV/nucleon[89]. The different panels show projections (in the plane defined by the projectile momentum (Z -axis) and the impact parameter (X -axis) of the total (a),(b),(c), neutron (d),(e),(f), and proton (g),(h),(i) densities. The nucleons bound in light clusters are **excluded** from the contour plots (d-i). Sections (j-l) display the N/Z ratio $R_{n/p}$ as a function of the distance D from the center of mass along the projection of the space coordinates on the projectile-target separation axis, excluding (solid) and including (open) the nucleons bound in small clusters.

engage in some speculation. First of all it can be imagined that if the clustering of light-symmetric clusters is important then the clustering of α -particles would be even more significant than deuteron clustering. Secondly there must be a mechanism by which some of the symmetric clusters escape the mid-velocity region intact and some coalesce with the excess neutrons. In the end, however, there is little that can be soundly concluded other than the fact that there exists an interesting mechanism that could potentially be responsible for the neutron-rich species observed in the mid-velocity region. Clearly, further study with more refined models is necessary.

4.2.4 Summary

While it can be expected that a proper description of heavy-ion collisions at intermediate energies must include a proper treatment of the quantal properties of the system, solutions of the BUU equation have been pursued to include the influence of two-body interactions on the dynamics. Time-dependent Hartree-Fock (TDHF) simulations provide a quantum treatment of the dynamics, although their ignorance of two-body interactions is thought to lead to an insufficient prediction of the extent of energy dissipation produced in the collisions. So, BUU is presently considered to be a “state-of-the-art” simulation despite its semiclassical nature. We can see from this study, however that the BUU simulations suffer from just the opposite problem of TDHF simulations, too much energy dissipation. It may be that quantal effects not included (or not properly “mocked-up”) in BUU simulations may be the cause of the model’s failure. It has been proposed that a possible improvement for these mean-field type simulations may lie in the inclusion of a stochastic term in the mean field to account for fluctuations that are lost in such single-particle descriptions of the dynamics. A revisiting of time-dependent Hartree-Fock (TDHF) simulations where a stochastic term is included in the mean field (STDHF) is being presently developed which promises to overcome the energy dissipation problems of standard TDHF and, of course, also includes a proper quantum treatment of the system[85, 90]. For the present, BUU simulations can provide us with a qualitative view into the possible reaction mechanisms of intermediate-energy heavy-ion collisions. The inclusion of light-cluster degrees of freedom into the BUU-like transport equation has led to the discovery of an interesting mechanism that may be responsible for the preponderance of neutron-rich species in the mid-velocity region. Interestingly, the BUU simulations

without this clustering mechanism are incapable of producing a significantly neutron-rich region in the mid-velocity region. This seems to indicate that one must consider the many-body aspects of the system in such a way that the clustering of particles can be treated fully and/or the quantal aspects of collisions, before the mechanism behind the neutron-rich fragment production can be properly understood. The mechanism found in the present model is tantalizing but can not lead us anywhere beyond speculation.

4.3 Liquid-Gas Phase Transitions in Asymmetric Nuclear Matter

4.3.1 Equilibrium Expectations

As was discussed in the introduction, numerous models based on equilibrium thermodynamics and the expected liquid-gas coexistence region for nuclear matter have been proposed to explain the phenomenon of multifragmentation in intermediate-energy heavy-ion collisions[20-35]. These models were encouraged, early on, by their ability to predict the experimentally observed dependence of the fragment mass yields for both proton and heavy-ion induced multifragmentation[91, 92]. The yields follow a power-law dependence on fragment mass A , $Y(A) \propto A^{-\tau}$. This dependence is predicted by the droplet model of Fisher[93] (which considers fragment formation near the critical point) when applied to symmetric nuclear matter[94]. However, this predictive power has become less impressive in light of studies of macroscopic fragmentation where power-law mass yields are observed as well, but the physics obviously has nothing to do with equilibrium thermodynamics. An excellent example of this is the recent study of Anders and Balslev[95] where square clay plates were allowed to “fall on a hard floor” and the fragments were collected and found to exhibit a two-component power law for the mass yield. On a more basic level, Sobotka and Moretto have shown that the partitioning of an integer in all possible ways with equal likelihood predicts a power-law yield for the integer size[96]. It becomes immediately obvious that a power-law mass yield found for the fragmentation of an object need not signify the importance of a phase transition. The observation that the mass yield follows a power law may be a necessary condition for the relevance of the liquid-gas coexistence region of nuclear matter, but it is definitely not a sufficient condition.

Furthermore, it is obviously questionable as to whether or not the equilibrium expectations of bulk nuclear matter can be extrapolated in a meaningful way to finite charged drops of nuclear matter. The experimental observables seem to be building a case against such models as well (for the types of systems examined in this study), and the BUU simulations studied in the last section seem to conspire with the data to cast doubt on this phase-transition scenario. Despite this mounting evidence, it remains useful to fully understand what the equilibrium expectations actually are. This study has placed much attention on N/Z observables and for us the question becomes, “How does the N/Z degree of freedom behave at equilibrium?”. We already know from the experimental sections of this study that there is an N/Z signature for multifragmentation in heavy-ion collisions. Perhaps this observation can be checked against the behavior of the N/Z degree of freedom in a liquid-gas phase transition.

Oddly enough, all models known to the author which attempt to describe the phenomenon of heavy-ion multifragmentation in the framework of a liquid-gas phase transition have completely ignored or artificially constrained the N/Z degree of freedom. This is not to say that the EOS of bulk uncharged asymmetric matter has not been well studied. In fact, more than 16 years ago Barranco and Buchler studied the phase diagram of asymmetric nuclear matter at low temperatures using a phenomenological equation of state[12]. They found that for the binary system of asymmetric nuclear matter, the coexistence region, called a binodal, is a two-dimensional surface (an object that reminded them of a Filet Mignon) rather than a one-dimensional line as expected for a one-component fluid. They also found that in general the concentrations of neutrons and protons must fractionate between the different density phases at equilibrium. It was only recently pointed out by Glendenning[18], however, that the driving force behind this fractionation is the isospin asymmetry energy of nuclear matter and that multifragmentation in heavy-ion collisions modeled within a framework of a liquid-gas phase transition should exhibit such a fractionation.

Even more recently, a study by Müller and Serot[19], which utilizes a relativistic mean-field model (without Coulomb interactions) of nuclear matter capable of reproducing bulk nuclear properties, has demonstrated some new and remarkable features of the predicted liquid-gas phase transition in asymmetric nuclear matter (including a confirmation of the expected fractionation). They found that the liquid-gas phase transition is second order (continuous entropy/nucleon as a function of temperature) rather than first order (discontinuous entropy/nucleon as a function of temperature),

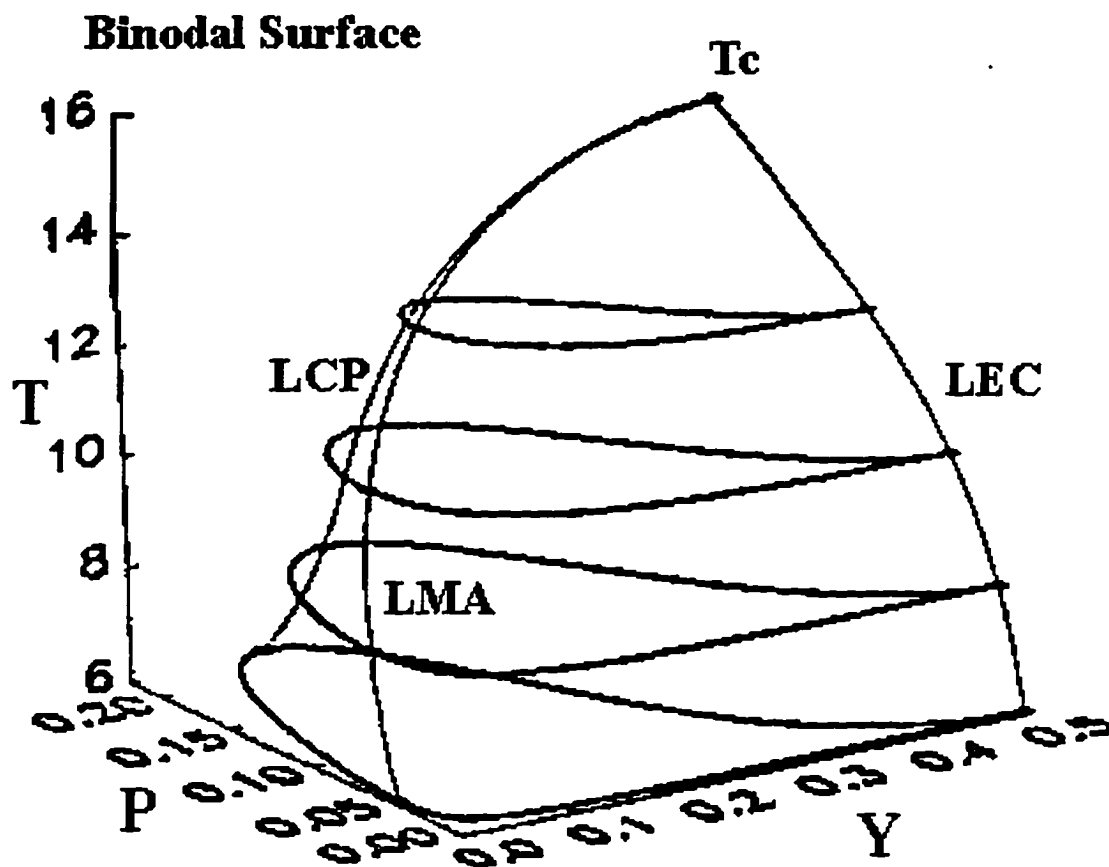


Figure 4.5: The binodal surface defining the phase-coexistence boundary for asymmetric nuclear matter plotted in Temperature T [MeV], pressure P [MeV/ $f m^3$], and proton fraction Y space. The critical temperature T_c at $Y = 0.5$, the line of equal concentrations (LEC), the line of critical points (LCP), Taken from Müller and Serot.

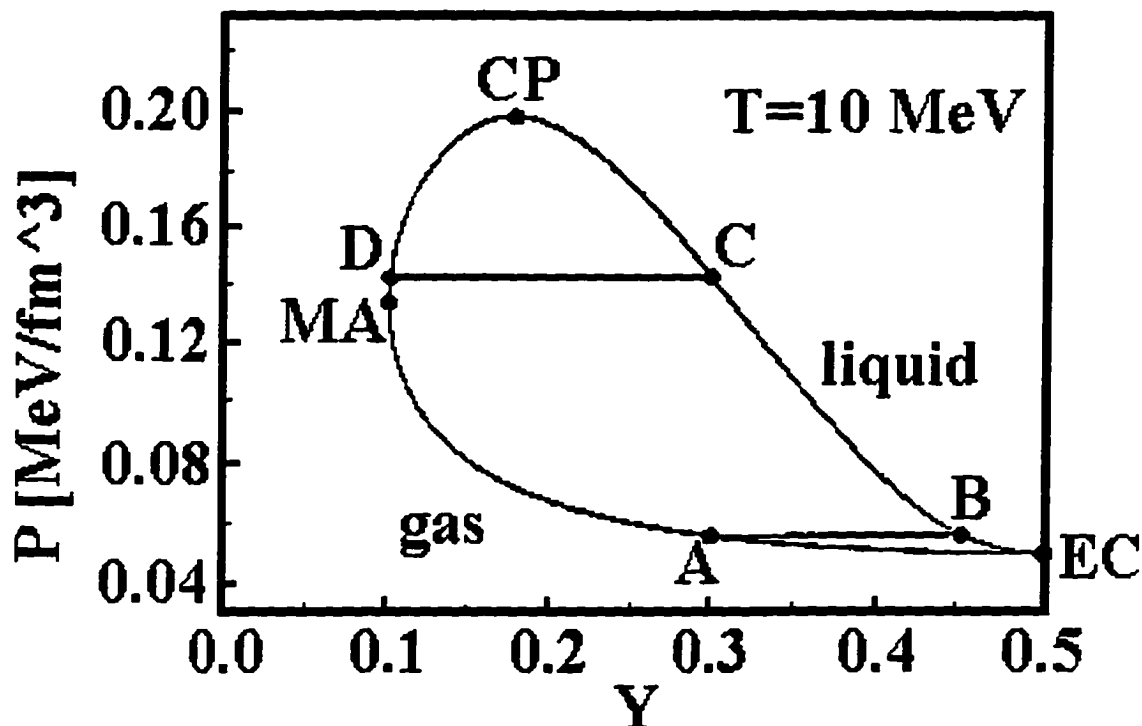


Figure 4.6: An isothermal slice of the binodal surface shown in figure 4.5 for $T=10$ MeV. The critical point (CP), the point of equal concentration (EC), and the point of maximal asymmetry (MA) are all indicated.

as expected in one component systems, and the instabilities that are contained in the coexistence region may occur from chemical instabilities as well as mechanical instabilities. The binodal surface of the two-dimensional phase-coexistence surface found in their study is displayed in figure 4.5. The binodal is displayed here as a surface in pressure p , temperature T , and proton fraction $Y = \frac{N_p}{N_p + N_n}$ space.

To understand the nature of the fractionation of neutron and proton concentrations between phases, which is our main interest, we now consider an isothermal slice ($kT = 10$ MeV) of this surface shown in figure 4.6. If we imagine a system with an overall proton fraction of $Y = 0.3$ that is initially at low pressure (the bottom of figure 4.6) and undergoes isothermal compression we see that as the coexistence region is traversed the proton concentration fractionates so that the gas-phase proton fraction Y_{gas} evolves from A to D while the liquid-phase proton fraction Y_{liquid} evolves from B to C. Thus the low-density gas phase becomes more asymmetric than the overall

system while the high-density liquid phase becomes less asymmetric. This behavior is understandable if one considers the density dependence of the isospin asymmetry energy. The kinetic part of this energy goes as $\rho^{2/3}$, as expected from an ideal Fermi gas model while the potential part is less certain, depending on the model considered but having a dependence between $\rho^{1/2}$ and ρ^2 [97]. Hence, the minimum free energy of the system is realized when the proton concentration fractionates among the phases, such that the high-density phase is more symmetric and the low-density phase is less symmetric than the total system. Note that there is overall neutron and proton conservation as Y at A equals Y at C. This fractionation is predicted for asymmetries or proton fractions that are quite accessible in heavy-ion collisions. The systems studied in this work have proton fractions of 0.40 for HH, 0.42 for HL-LH, and 0.44 for LL. Future experiments with heavy radioactive beams should be able to probe proton fractions as low as 0.30. However, there are some important physics issues missing from these bulk equilibrium calculations that must be addressed before we can consider comparing equilibrium expectations with heavy-ion reaction data.

While the fractionation discussed above is reasonable for nuclear matter that is uncharged or Coulombically screened such as supernova matter, caution must be exercised when considering heavy-ion collisions. Naively, for very heavy nuclei which start out necessarily already neutron rich, these models would predict the production of a proton-enriched liquid phase and an even further neutron-enriched vapor phase. The necessity of Coulomb and surface energy terms to describe the bulk properties of ground state nuclei (e.g. the liquid drop model) can be taken as a good indication that one needs to take account of such effects when attempting to apply these results to the finite nuclei involved in heavy-ion collisions. A reasonable estimation of the influence of the Coulomb energy of a charged drop on the fractionation of neutron and proton concentrations can be obtained by constructing a model that exhibits a reasonable density dependence for the isospin asymmetry and Coulomb energies. Although surface energy corrections can be large, the Coulomb energy shifts the chemical potential of the protons alone and can be expected to perturb the neutron and proton concentrations to the greatest extent. Therefore, a simple two-component van der Waals model was developed to study the influence of finite Coulomb interactions on the expected neutron and proton fractionation between phases in the liquid-gas coexistence region.

4.3.2 Two-Component van der Waals Liquid

To deal with the influence of the Coulomb energy of a finite charged spherical drop on the neutron and proton fractionation in the phase-coexistence region, a model for asymmetric nuclear matter as a simple two-component van der Waals liquid is developed. The canonical partition function Z , for a dense liquid with two indistinguishable components interacting via a short range attractive potential with a hard core is given by

$$Z(N_n, N_p, V, T) = e^{-\beta A} = \frac{(V - V_{nn}N_n - V_{np}N_p)^{N_n} (V - V_{pp}N_p - V_{np}N_n)^{N_p}}{N_n! N_p! \Lambda_n^{3N_n} \Lambda_p^{3N_p}} \times e^{-\frac{\beta}{V} [(N_n + N_p)(U_{eff}^n + U_{eff}^p)]}, \quad (4.32)$$

where β is the inverse temperature, A is the Helmholtz free energy, N_n is the number of neutrons, N_p is the number of protons, and V is the total volume of the system. V_{nn} , V_{pp} , and V_{np} are the neutron-neutron, proton-proton, and neutron-proton interaction excluded volumes respectively. Λ_n and Λ_p are the thermal deBroglie wavelengths of the neutrons and the protons respectively, while $U_{eff}^{n,p}$ is the effective mean-field interaction due to nn, pp, and np interactions. The model is further simplified by setting $V_{hc} = V_{nn} = V_{pp} = V_{np}$, which is equivalent to saying the hard-core part of the potential is independent of the isospin projection. The Helmholtz free energy can be immediately obtained, with the use of Stirling's approximation which requires that we are in the thermodynamic limit (i.e. $N_n \Rightarrow \infty$ and $N_p \Rightarrow \infty$), and is given by

$$-\beta A = N_n \ln \left[\frac{V - V_{hc}(N_n + N_p)}{N_n \Lambda_n^3} e \right] + N_p \ln \left[\frac{V - V_{hc}(N_n + N_p)}{N_p \Lambda_p^3} e \right] + \frac{\beta}{V} (a_{nn}N_n^2 + a_{pp}N_p^2 + 2a_{np}N_nN_p) \quad (4.33)$$

where the mean-field interaction term $N_n U_{eff}^n + N_p U_{eff}^p$ has been replaced by van der Waals-like terms a_{ij} to describe the attractive strong nuclear interactions. The terms a_{ij} are defined by $a_{ij} \equiv -\frac{1}{2} \int_{r_{12} > R_0} dr_{12} U_{ij}(r_{12})$, where U_{ij} is the pair wise interaction between a particle of type i and j . Note that the integrand defined above is only evaluated over the attractive part of the potential outside of the hard-core volume $b = \frac{2\pi}{3} R_0^3$. As we did with the hard core we can again assume that $a = a_{nn} = a_{pp} = a_{np}$, which implies that the attractive part of the interaction potential is also isospin-projection independent. Making the substitutions $b = V_{hc}$, $a = a_{nn} = a_{pp} = a_{np}$, we

arrive at

$$-\beta A = N_n \ln \left[\frac{V - b(N_n + N_p)}{N_n \Lambda_n^3} e \right] + N_p \ln \left[\frac{V - b(N_n + N_p)}{N_p \Lambda_p^3} e \right] + \frac{\beta}{V} (aN^2) \quad (4.34)$$

From this we can calculate some relevant thermodynamic quantities. First the pressure is derived,

$$p = \frac{1}{\beta} \frac{\partial \ln(Z)}{\partial V} = -\frac{\partial A}{\partial V} = \frac{\rho}{\beta(1 - b\rho)} - a\rho^2. \quad (4.35)$$

One can immediately see that the inclusion of the hard-core excluded volume b and the mean-field effective interaction a in the partition function leads to the famous van der Waals equation of state (EOS). Next, the chemical potential of neutrons,

$$\mu_n = -\frac{1}{\beta} \frac{\partial \ln(Z)}{\partial N_n} = \frac{\partial A}{\partial N_n} = \frac{1}{\beta} \left(\frac{1}{1 - b\rho} \right) - 2a\rho + \frac{1}{\beta} \ln \left(\frac{\rho_n}{1 - b\rho} \frac{\Lambda_n^3}{e} \right), \quad (4.36)$$

the chemical potential of protons,

$$\mu_p = -\frac{1}{\beta} \frac{\partial \ln(Z)}{\partial N_p} = \frac{\partial A}{\partial N_p} = \frac{1}{\beta} \left(\frac{1}{1 - b\rho} \right) - 2a\rho + \frac{1}{\beta} \ln \left(\frac{\rho_p}{1 - b\rho} \frac{\Lambda_p^3}{e} \right), \quad (4.37)$$

and the total energy of the system

$$E = \frac{\partial \ln(Z)}{\partial \beta} = -\frac{\partial \beta A}{\partial \beta} = \frac{3N}{2\beta} - a\rho N, \quad (4.38)$$

are determined, where we have expressed quantities in terms of nucleon densities $\rho = \frac{N_i}{V}$, $\rho = \rho_n + \rho_p$, and total number of nucleons $N = N_n + N_p$. The van der Waals parameter a for symmetric uncharged nuclear matter can be determined by fixing the binding energy at zero temperature and saturation density $E(\beta = 0, \rho_o) = -16[MeV]$. When saturation density is taken to be $\rho_o = 0.16[fm^{-3}]$, this yields, $a = 100[MeV fm^{-3}]$.

The excluded volume b can be determined by fixing the critical temperature, $T_c \approx 15[MeV]$ to correspond with values determined by more sophisticated models[19]. Unfortunately, this causes the coexistence region to enclose saturation density at zero temperature and this can only be prevented by altering the value of a . Keeping in mind that this calculation is only to provide a rough estimate of the degree of fractionation in the system, we take $R_o = 1.0$ and do not change the value

of a . This yields a value of $b = 6.57[fm^3]$ and a critical temperature of $4.83[MeV]$. This is roughly a factor of three lower than accepted values but is acceptable for this simple classical model (However, this shortcoming did motivate the investigation of a more sophisticated model. See the next section.). While the mean-field nature of this model makes the internuclear potential somewhat arbitrary, a simple hard-core plus Yukawa potential consistent with these parameters is shown in figure 4.7 to orientate the reader. The hard core is seen to extend from the origin to $r = R_o$ and a short-range attractive region follows which satisfies the condition $a = -100.0[MeV fm^{-3}]$.

The inclusion of asymmetry-dependent terms in the equation of state of nuclear matter is a topic of renewed interest, due to the relevance of these terms in predicting the dynamics of supernovae. Several theoretical studies have suggested that the asymmetric EOS for nuclear matter takes the form[97]

$$E(\rho, \Delta) = E(\rho, \Delta = 0) + S(\rho) \times \Delta^2 \quad (4.39)$$

where $E(\rho, \Delta)$ is the energy per nucleon, $E(\rho, \Delta = 0)$ is the density dependent EOS for symmetric nuclear matter, $\Delta = (\rho_n - \rho_p) / (\rho_n + \rho_p)$ is the relative neutron excess, and $S(\rho)$ is the bulk isospin asymmetry energy. At normal nuclear density, the value of $S(\rho_o)$ is approximately 32 MeV, while the actual density dependence varies with model. A convenient parameterization of the density dependence of the various asymmetry energies suggested in the literature has been provided by Prakash et al.[97]

$$S\left(\frac{\rho}{\rho_o}\right) = (2^{2/3} - 1) \frac{3}{5} \epsilon_f^o \left[\left(\frac{\rho}{\rho_o}\right)^{2/3} - F\left(\frac{\rho}{\rho_o}\right) \right] + S_o F\left(\frac{\rho}{\rho_o}\right) \quad (4.40)$$

where ϵ_f^o is the Fermi Energy at saturation density and $F(x)$ takes the forms

$$F(x) = x \quad (4.41)$$

$$F(x) = \frac{2x^2}{1+x} \quad (4.42)$$

$$F(x) = \sqrt{x} \quad (4.43)$$

The isospin asymmetry energy $S\left(\frac{\rho}{\rho_o}\right)$ is displayed as a function of $\frac{\rho}{\rho_o}$ for these three parameterizations in figure 4.8. For this study, $F(x) = x$ was taken as a representative.

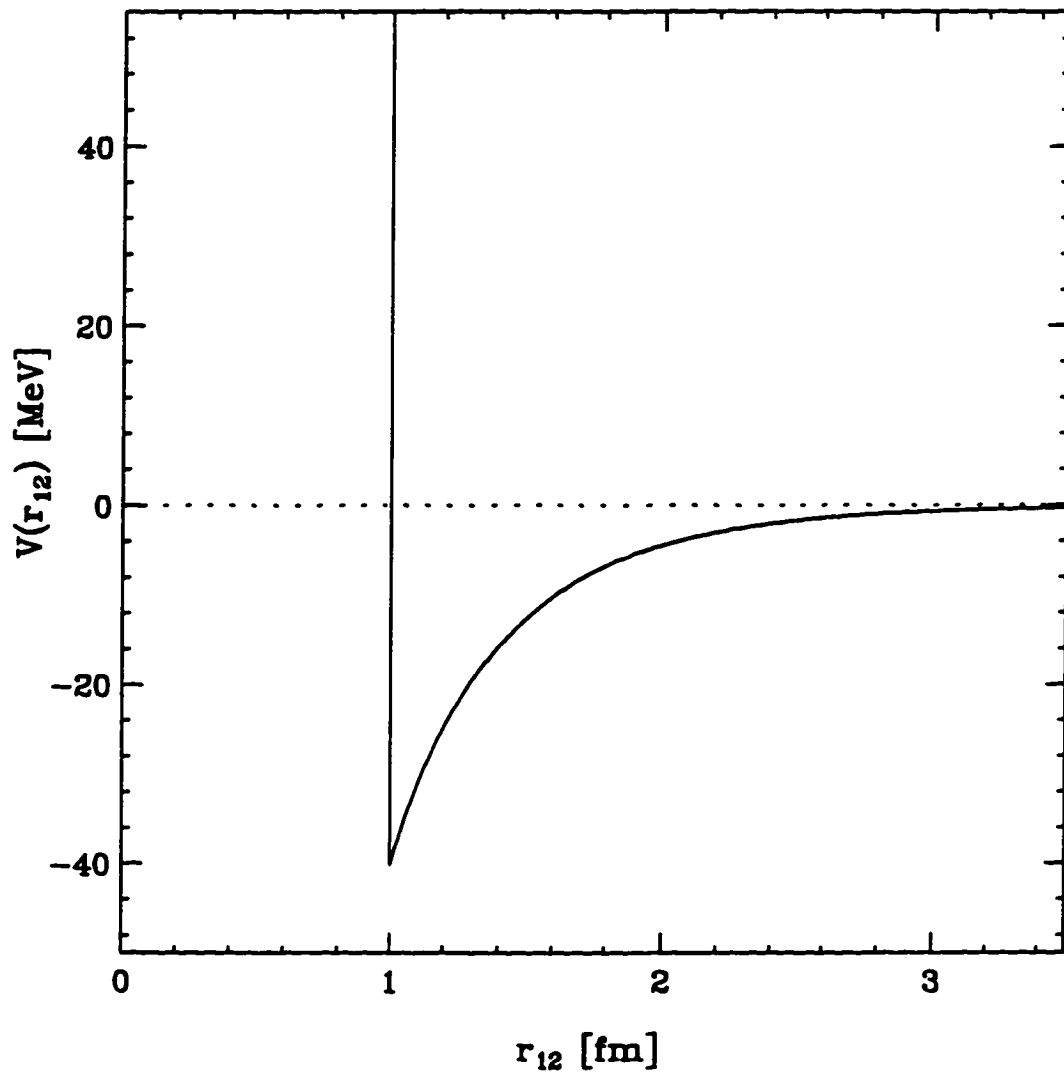


Figure 4.7: A hard-core and Yukawa interaction that is consistent with the parameters of the van der Waals parameters used in this study.

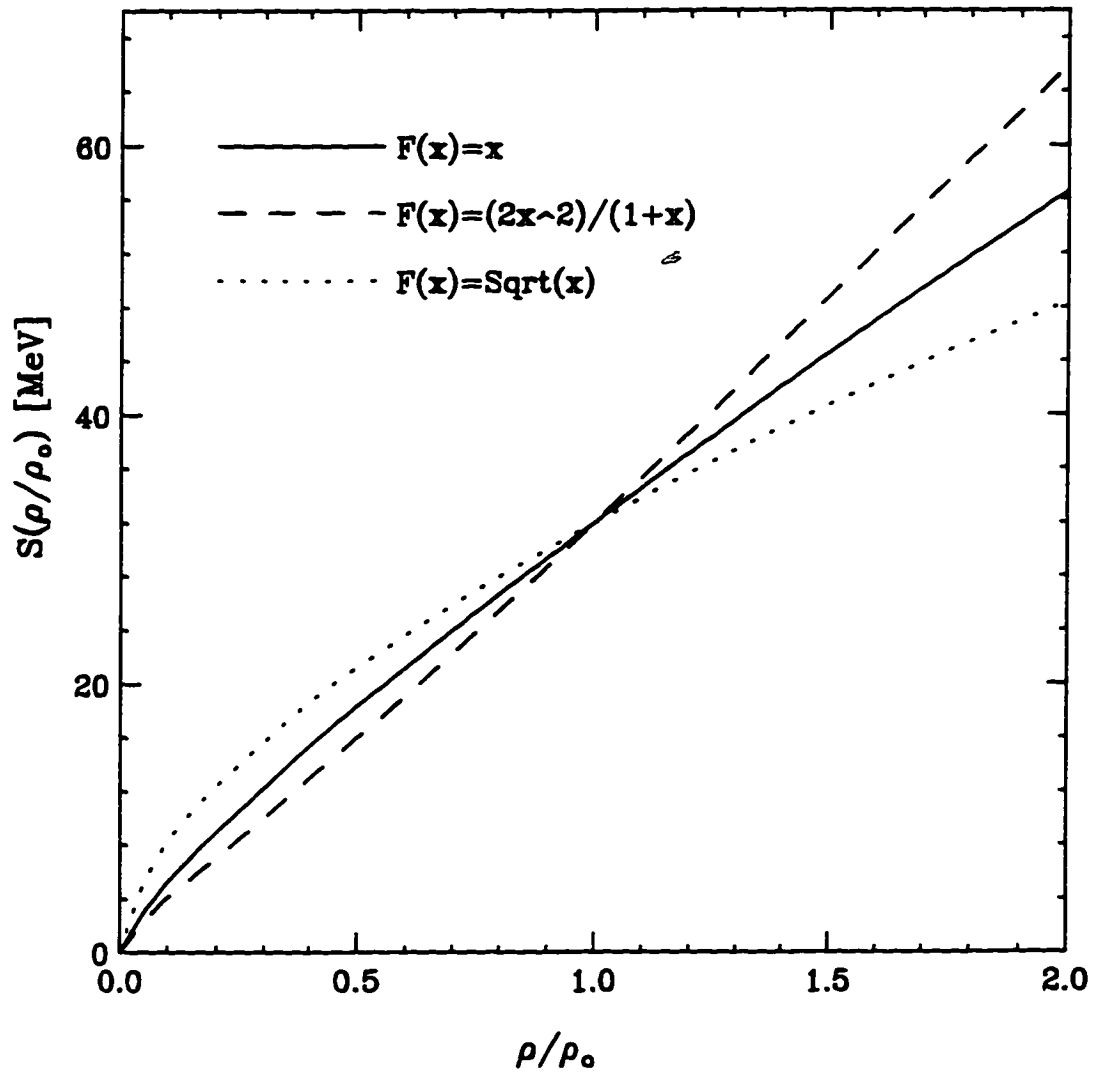


Figure 4.8: The isospin asymmetry energy $S\left(\frac{\rho}{\rho_0}\right)$ as a function of $\frac{\rho}{\rho_0}$ for the three parameterizations suggested in the literature [97].

parameterization, as they are all of similar magnitude, and we have

$$S(\rho) = e_a \left[\left(\frac{\rho}{\rho_o} \right)^{2/3} - \left(\frac{\rho}{\rho_o} \right) \right] + S_o \times \left(\frac{\rho}{\rho_o} \right), \quad (4.44)$$

where the appearance of this expression was simplified by setting $e_a = (2^{2/3} - 1) \frac{3}{5} \epsilon_f^o$. Including an appropriate mean-field term in the partition function results in the following expressions for the Helmholtz free energy,

$$-\beta A = N_n \ln \left[\frac{V - b(N_n + N_p)}{N_n \Lambda_n^3} e \right] + N_p \ln \left[\frac{V - b(N_n + N_p)}{N_p \Lambda_p^3} e \right] + \frac{\beta}{V} \left(aN^2 - \frac{(\rho_n - \rho_p)^2}{\rho^3} \left[e_a \left[\left(\frac{\rho}{\rho_o} \right)^{2/3} - \left(\frac{\rho}{\rho_o} \right) \right] + S_o \times \left(\frac{\rho}{\rho_o} \right) \right] N^2 \right), \quad (4.45)$$

the pressure,

$$p = \frac{\rho}{\beta(1-b\rho)} - a\rho^2 + \frac{(\rho_n - \rho_p)^2}{\rho} \left[e_a \left[\left(\frac{\rho}{\rho_o} \right) - \frac{2}{3} \left(\frac{\rho}{\rho_o} \right)^{2/3} \right] + S_o \times \frac{2}{3} \left(\frac{\rho}{\rho_o} \right)^{2/3} \right], \quad (4.46)$$

the chemical potential of neutrons,

$$\begin{aligned} \mu_n = & \frac{1}{\beta} \left(\frac{1}{1-b\rho} \right) - 2a\rho + \frac{1}{\beta} \ln \left(\frac{\rho_n \Lambda_n^3}{1-b\rho} e \right) \\ & + (1 - 4y + 4y^2) \left[e_a \left[\left(\frac{\rho}{\rho_o} \right) - \frac{2}{3} \left(\frac{\rho}{\rho_o} \right)^{2/3} \right] + S_o \times \frac{2}{3} \left(\frac{\rho}{\rho_o} \right)^{2/3} \right] \\ & + (1 - 4y^2) \left[e_a \left[\left(\frac{\rho}{\rho_o} \right) - \left(\frac{\rho}{\rho_o} \right)^{2/3} \right] + S_o \times \left(\frac{\rho}{\rho_o} \right)^{2/3} \right], \end{aligned} \quad (4.47)$$

the chemical potential of protons,

$$\begin{aligned} \mu_p = & \frac{1}{\beta} \left(\frac{1}{1-b\rho} \right) - 2a\rho + \frac{1}{\beta} \ln \left(\frac{\rho_p \Lambda_p^3}{1-b\rho} e \right) \\ & + (1 - 4y + 4y^2) \left[e_a \left[\left(\frac{\rho}{\rho_o} \right) - \frac{2}{3} \left(\frac{\rho}{\rho_o} \right)^{2/3} \right] + S_o \times \frac{2}{3} \left(\frac{\rho}{\rho_o} \right)^{2/3} \right] \\ & - (3 - 8y + 4y^2) \left[e_a \left[\left(\frac{\rho}{\rho_o} \right) - \left(\frac{\rho}{\rho_o} \right)^{2/3} \right] + S_o \times \left(\frac{\rho}{\rho_o} \right)^{2/3} \right], \end{aligned} \quad (4.48)$$

and the total energy of the system,

$$E = \frac{3N}{2\beta} - a\rho N + S(\rho) \times \Delta^2. \quad (4.49)$$

Notice that the expression for the energy has the form suggested above in equation 4.39 and all terms related to the isospin asymmetry energy vanish for $Y = 0.5$.

A simple Coulomb energy term for a spherical charged drop of radius R is given by

$$E_{coul} = \frac{3\alpha\hbar c Z^2}{5R}. \quad (4.50)$$

Assuming uniform density, the density dependence can be readily included,

$$E_{coul}(Z, \rho) = C_{coul}(Z) \times \rho_p^{1/3}, \quad (4.51)$$

where $C_{coul}(Z)$ gives the Coulomb energy for a drop with Z protons. Inclusion of the term $C_{coul}(Z) \times \rho_p^{1/3} N$ into the exponent of the partition function yields new expressions for the pressure

$$p = \frac{\rho}{\beta(1-b\rho)} - a\rho^2 + \frac{(\rho_n - \rho_p)^2}{\rho} \left[e_a \left[\left(\frac{\rho}{\rho_o} \right) - \frac{2}{3} \left(\frac{\rho}{\rho_o} \right)^{2/3} \right] + S_o \times \frac{2}{3} \left(\frac{\rho}{\rho_o} \right)^{2/3} \right] + \frac{1}{3} C_{coul}(Z) \rho^{4/3} \quad (4.52)$$

and the chemical potential of protons,

$$\begin{aligned} \mu_p = & \frac{1}{\beta} \left(\frac{1}{1-b\rho} \right) - 2a\rho + \frac{1}{\beta} \ln \left(\frac{\rho_p}{1-b\rho} \frac{\Lambda_p^3}{e} \right) \\ & + (1 - 4y + 4y^2) \left[e_a \left[\left(\frac{\rho}{\rho_o} \right) - \frac{2}{3} \left(\frac{\rho}{\rho_o} \right)^{2/3} \right] + S_o \times \frac{2}{3} \left(\frac{\rho}{\rho_o} \right)^{2/3} \right] \\ & - (3 - 8y + 4y^2) \left[e_a \left[\left(\frac{\rho}{\rho_o} \right) - \left(\frac{\rho}{\rho_o} \right)^{2/3} \right] + S_o \times \left(\frac{\rho}{\rho_o} \right)^{2/3} \right] + \frac{4}{3} C_{coul}(Z) \rho^{1/3} \end{aligned} \quad (4.53)$$

By fixing $C_{coul} = C_{coul}(54)$, the pressure and chemical potential of protons are adjusted by the average amount appropriate for nucleons in Xenon drops with densities of the given bulk phases at equilibrium. This produces equilibrium values that are more relevant to heavy-ion collisions. Physically this approximation can be seen as an equilibrium between phases where the influence of being inside a uniformly charged Xenon drop (with the density of the given phase) perturbs the pressure and proton chemical potential.

Results

Given the expressions for the pressure and the chemical potentials, the binodal surface is found by solving the system of non-linear equations given by Gibbs's criteria. The criteria for two phases ψ and ϕ in equilibrium are that the pressure must be equal in

both phases,

$$P^\psi(\rho_n, \rho_p, \beta) = P^\phi(\rho_n, \rho_p, \beta) \quad (4.54)$$

the chemical potentials for neutrons are equal in both phases,

$$\mu_n^\psi(\rho_n, \rho_p, \beta) = \mu_n^\phi(\rho_n, \rho_p, \beta) \quad (4.55)$$

and the chemical potentials for protons are equal in both phases.

$$\mu_p^\psi(\rho_n, \rho_p, \beta) = \mu_p^\phi(\rho_n, \rho_p, \beta) \quad (4.56)$$

Nontrivial solutions for this system of equations which provide distinct phases can be found if the proton fraction of one phase is specified for a given inverse temperature β . In practice, the one-dimensional spinodal for symmetric matter was determined analytically and the asymmetry and Coulomb modified solutions were found by slowly perturbing the symmetric solution and using Newton's Method to solve the system of equations. Figure 4.9 schematically displays the binodals for this model in density ρ , temperature T and proton fraction Y space with and without the influence of the finite Coulomb energy of a charged xenon drop. The larger binodal is the coexistence surface considering only the density-dependent isospin asymmetry energy. The smaller surface (enclosed by the larger one) is the coexistence surface when both the density dependent isospin asymmetry energy and the density dependent finite Coulomb energy are included in the free energy. The two surfaces become quite similar and approach each other in the region of low density and low temperature shown in the graph. The critical temperature of symmetric matter including Coulomb is $\approx 2[MeV]$ less than the critical temperature without Coulomb. This is in qualitative agreement with previous studies that have attempted to account for the influence of the Coulomb energy on the critical temperature[98].

Figure 4.10 shows the proton fraction of the gas phase Y_{gas} as a function of the proton fraction of the liquid phase Y_{liquid} for all proton fractions attainable on the binodal (for neutron-rich systems $Y_{liquid} < 0.5$) at four fixed temperature slices with and without the influence of the finite Coulomb energy (of a charged xenon drop). The dotted lines in this plot show the line of equal concentration in both phases. A solution on this line represents an azeotrope or indifferent equilibrium where there is no fractionation. Solutions above this dotted line indicate that the

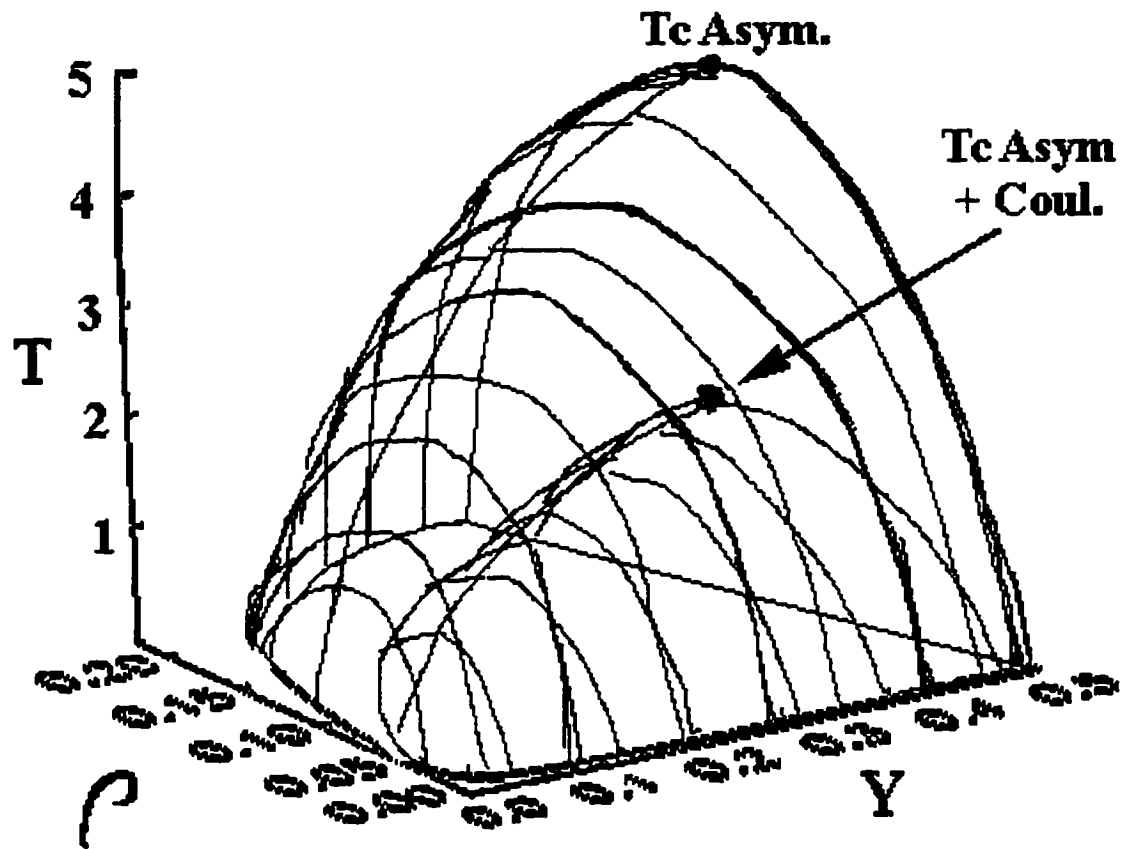


Figure 4.9: A sketch of the binodal surface defining the phase-coexistence boundary for the two-component van der Waals model plotted in Temperature T [MeV], density ρ [fm^{-3}], and proton fraction Y space, with and without the influence of finite Coulomb interactions.

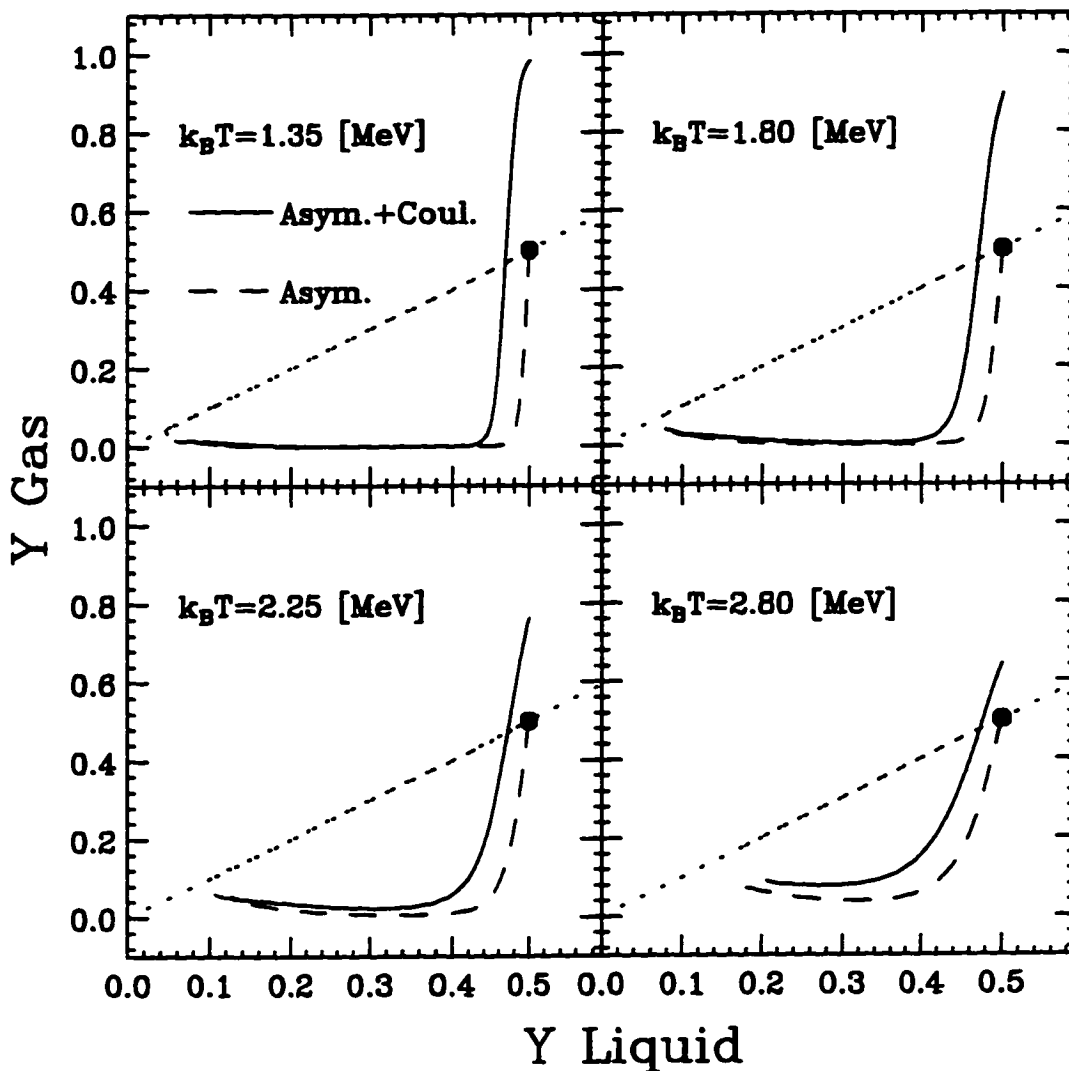


Figure 4.10: The proton fraction found in the low-density phase Y_{gas} as a function of the proton fraction found in the high-density phase Y_{liquid} at equilibrium for four different temperatures with Coulomb (solid line) and without Coulomb (dashed line) for the Two-Component van der Waals Model. The dotted line marks equal concentrations in the phases. Above this line the gas phase is proton rich and below this line the gas phase is neutron rich relative to the liquid phase.

high-density phase contains a neutron excess and solutions below this line indicate that the low-density phase contains a neutron excess. The dashed lines in this plot represent the solution **without** finite Coulomb interactions and show the behavior expected from the studies discussed above, i.e. the lines intersect the dotted lines at symmetry and remain below the dotted line with decreasing Y_{liquid} . So as expected, a system which is already neutron rich ($Y < 0.5$) will fractionate into a more neutron-rich low-density gas phase and more proton-rich high-density liquid phase (i.e. the dashed line remains below the dotted line). The solution including the effect of finite Coulomb interactions are displayed as solid lines in the plot. One might naively expect the isospin asymmetry energy to dominate over the Coulomb energy in this model when considering that the isospin asymmetry energy is roughly proportional to $\rho^{2/3}$ while the Coulomb energy of a charged sphere is proportional to $\rho^{1/3}$. So the benefit of placing protons in the liquid phase might outweigh the penalty incurred by the Coulomb energy. However, a heavy ion such as a Xenon drop is sufficiently highly charged that when the system is near symmetry the system actually prefers to fractionate such that the low-density phase becomes proton rich. This, of course, is the opposite to the uncharged case considered above. We see that for sufficiently asymmetric matter, one recovers the same sense of the fractionation that is observed for uncharged matter, the low-density phase being enriched in neutrons. Between these two cases (neutron-rich high-density phase and neutron-rich low-density phase) lies the azeotrope asymmetry which is approximately $Y_{liquid} = 0.45$ in this case.

An analogy between the position of the azeotrope and the N/Z of the valley of beta stability for ground state nuclei can be drawn so that such a prediction seems reasonable for the warmer matter considered in this model. We see then that the N/Z fractionation expected for charged matter can produce a neutron excess in either phase depending on the N/Z (or proton fraction) of the total system. Looking to the different temperature slices in figure 4.10 it can be seen that the severity of the fractionation decreases with temperature. In this model this is due to the fact that near the top of the binodal (high temperature) the difference in the density of the phases is diminished until it vanishes at the critical point. One would even suspect that at the critical points the fractionation might vanish altogether. This is not necessarily the case as, in analogy to the enormous density fluctuations expected near the critical point, there should also be large concentration fluctuations which might provide us with another fractionation observable. Consideration of the temperature

dependence of the fractionation in general, however, raises another concern. In this model the isospin asymmetry energy is independent of temperature. The purely quantum nature of this effect, however, leads one to conclude that as the temperature increases the isospin asymmetry energy should decrease. This feature of the isospin asymmetry energy has been completely ignored in this model. As this effect could significantly alter the predicted N/Z fractionation a classical correspondence that requires that this energy vanishes in a non-degenerate system should be built into the model.

Examination of the magnitude of the N/Z fractionation predicted for all temperatures displayed in figure 4.10 demonstrates that a significant N/Z signature should be expected in any IMF's produced by a liquid gas phase transition at equilibrium. However, the lack of a temperature dependence in the isospin asymmetry energy and the low value of the critical point in this model leave the results suspect, and raise a question about the influence of thermal effects on the fractionation.

4.3.3 Two-Component Hard-Core Skyrme Liquid

To overcome the inability of the van der Waals model to produce a reasonable critical temperature and to include an asymmetry energy which has a reasonable temperature dependence, a model for asymmetric nuclear matter is borrowed from H.R. Jaqaman[98] and modified, to suit our purposes, as described below. This model is based on a general zero-range Skyrme Interaction

$$v_{12} = -\frac{8a_o}{3} (1 + x_o P_\sigma) \delta(r_1 - r_2) + \frac{16a_3}{6} (1 + x_3 P_\sigma) \rho^\sigma \left[\frac{r_1 - r_2}{2} \right] \delta(r_1 - r_2), \quad (4.57)$$

where the Skyrme constants a_o and a_3 are related to the more familiar t_o and t_3 Skyrme parameters in the following way: $t_o = \frac{8a_o}{3}$, $t_3 = \frac{16a_3}{6}$, and P_σ is the spin exchange operator (it prevents Hartree-Fock "exchange" terms), σ , x_o , and x_3 are more fit parameters and ρ is the nucleon density.

For symmetric nuclear matter without Coulomb, the following EOS was found by Jaqaman using "finite-temperature Hartree-Fock" theory, yielding the pressure

$$P(\rho, \beta) = -a_o \rho^2 + a_3 (1 + \sigma) \rho^{\sigma+2} + \frac{\rho}{\beta} \left[1 + \sum_{n=1}^{\infty} b_n \left(\frac{\Lambda^3 \rho}{g} \right)^n \right] \quad (4.58)$$

and the chemical potential for nucleons

$$\mu(\rho, \beta) = -2a_0\rho + a_3(2 + \sigma)\rho^{1+\sigma} + \frac{1}{\beta} \left[\ln \left(\frac{\Lambda^3 \rho}{g} \right) + \sum_{n=1}^{\infty} \frac{n+1}{n} b_n \left(\frac{\Lambda^3 \rho}{g} \right)^n \right], \quad (4.59)$$

where β is the inverse temperature, g is the spin-isospin degeneracy factor, g_s is the spin degeneracy factor, Λ is the thermal deBroglie wavelength, and the b_n are the virial expansion coefficients for a weakly-degenerate ideal Fermi gas[99]. The expressions given in equations 4.58 and 4.59 are what one would expect for system of Fermions at moderate temperatures interacting via the potential defined by equation 4.57. The expansions found in equations 4.58 and 4.59 converge quite rapidly, within five terms, for moderately high temperatures $\frac{1}{\beta} \geq 3.5$ MeV. The first five coefficients are:

$$b_1 = \frac{\sqrt{2}}{8} \quad (4.60)$$

$$b_2 = \frac{1}{8} - \frac{2\sqrt{3}}{27} \quad (4.61)$$

$$b_3 = \frac{3}{32} + \frac{5\sqrt{2}}{64} - \frac{\sqrt{6}}{12} \quad (4.62)$$

$$b_4 = \frac{317}{1728} - \frac{\sqrt{2}}{8} + \frac{\sqrt{3}}{6} - \frac{4\sqrt{5}}{125} \quad (4.63)$$

$$b_5 = \frac{35}{128} + \frac{1687\sqrt{2}}{1728} - \frac{5\sqrt{3}}{72} - \frac{5\sqrt{6}}{36} - \frac{\sqrt{10}}{20}. \quad (4.64)$$

The parameters a_0 , a_3 , and σ are fixed in this model by the properties of ground state nuclear matter. This can be accomplished by requiring the average nuclear binding energy E_B to have a value of -16 MeV at saturation density ρ_0

$$E_B = E_K(\rho_0^{2/3}) - a_0\rho_0 + a_3\rho_0^{\sigma+1}, \quad (4.65)$$

the average nuclear binding energy E_B to have a minimum at saturation density

$$\rho \left[\frac{\partial E_B}{\partial \rho} \right]_{\rho_0} = \frac{2}{3} E_K(\rho_0^{2/3}) - a_0\rho_0 + a_3(1 + \sigma)\rho_0^{\sigma+1}, \quad (4.66)$$

and the isothermal compressibility κ to have a value of 222 Mev

$$\kappa = 9\rho^2 \left[\frac{\partial^2 E_B}{\partial \rho^2} \right]_{\rho_o} = -3E_K (\rho_o^{2/3}) + 9a_3\sigma (1 + \sigma) \rho_o^{\sigma+1}. \quad (4.67)$$

The term $E_K (\rho_o^{2/3})$ is the average kinetic energy per nucleon, taken to be that of an ideal Fermi gas. The parameters a_o , a_3 , and σ then take on the values of 800.0 [MeV fm³], 879.4 [MeV fm^{3+3σ}], and $\frac{1}{4}$ respectively. The parameter x_3 is set to 1 (by convention) and x_o is fixed by setting the isospin asymmetry energy, taken to be 30 MeV such that

$$S(\rho_o) = \frac{1}{3} \frac{\hbar^2 K_F^2}{2m} + \frac{2}{3} \left(x_o + \frac{1}{2} \right) a_o \rho_o - a_3 \rho_o^{1+\sigma} \quad (4.68)$$

where K_F is the Fermi wave number.

For an asymmetric system the chemical potential for the species q is given by

$$\mu_q(\rho, \beta) = \epsilon_q + \frac{1}{\beta} \left[\ln \left(\frac{\Lambda^3 \rho}{g_s} \right) + \sum_{n=1}^{\infty} \frac{n+1}{n} b_n \left(\frac{\Lambda^3 \rho_q}{g_s} \right)^n \right] \quad (4.69)$$

where the potential part is given by

$$\begin{aligned} \epsilon_q = & -\frac{8a_o}{3} \left[\left(1 + \frac{x_o}{2} \right) \rho - \left(x_o + \frac{1}{2} \right) \rho_q \right] \\ & + 4a_3 \left[\rho^{\sigma+1} - \sigma \rho^{\sigma-1} \rho_q^2 + (\sigma - 1) \rho^\sigma \rho_q \right] + \delta_{qp} V_{Coul}(\rho_p), \end{aligned} \quad (4.70)$$

where the Coulomb potential, taken to be the same as in the the van der Waals model, has been added to the chemical potential for protons. While this EOS naturally has a critical point which is closer to those predicted by more sophisticated models, it has another problem of its own. The shape of the binodal produced by this EOS is somewhat pathological in that the critical point increases with increasing asymmetry instead of decreasing as it should. This is not terribly surprising in that the Skyrme parameters are fit to the properties of symmetric matter at saturation density. The result is that the repulsive term in the potential part is not increasing as fast as it should with asymmetry. An intuitive way to fix this problem is to add a repulsive hard-core term into EOS. This term will only be important at the higher temperatures, near the critical temperatures, and causes the binodal to behave in a reasonable fashion, i.e. the critical point decreases with increasing asymmetry. Thus the expression has been modified to include the influence of a hard core and expressed

in terms of the proton fraction y . Specifically, for protons we have

$$\mu_p(\rho, y, \beta) = \epsilon_q + \frac{1}{\beta} \left[\frac{1}{(1-b\rho)} + \ln \left(\frac{\Lambda^3 \rho}{g_s (1-b\rho)} \right) + \sum_{n=1}^{\infty} \frac{n+1}{n} b_n \left(\frac{\Lambda^3 \rho y}{g_s} \right)^n \right], \quad (4.71)$$

$$\begin{aligned} \epsilon_p(\rho, y) = & -\frac{8a_0}{3} \left[\left(1 + \frac{x_0}{2}\right) \rho - \left(x_0 + \frac{1}{2}\right) \rho y \right] \\ & + 4a_3 \rho^{1+\sigma} [1 - \sigma y^2 + (\sigma - 1)y] + V_{Coul}(\rho, y), \end{aligned} \quad (4.72)$$

and correspondingly for neutrons,

$$\mu_n(\rho, y, \beta) = \epsilon_q + \frac{1}{\beta} \left[\frac{1}{(1-b\rho)} + \ln \left(\frac{\Lambda^3 \rho}{g_s (1-b\rho)} \right) + \sum_{n=1}^{\infty} \frac{n+1}{n} b_n \left(\frac{\Lambda^3 \rho (1-y)}{g_s} \right)^n \right], \quad (4.73)$$

$$\begin{aligned} \epsilon_n(\rho, y) = & -\frac{8a_0}{3} \left[\left(1 + \frac{x_0}{2}\right) \rho - \left(x_0 + \frac{1}{2}\right) \rho (1-y) \right] \\ & + 4a_3 \rho^{1+\sigma} [1 - \sigma (1-y)^2 + (\sigma - 1)(1-y)]. \end{aligned} \quad (4.74)$$

The value of b was then adjusted to yield a reasonable critical temperature of ~ 12 MeV. Notice that the hard-core term is included by replacement of the density terms, ρ , by a term $\rho/(1-b\rho)$ and that a term $\frac{1}{(1-b\rho)}$ is added inside the thermal term. These terms are what were derived in the previous canonical model. Finally we can utilize the Gibbs-Duhem relation

$$\frac{\partial P}{\partial \rho} = y\rho \frac{\partial \mu_p}{\partial \rho} + (1-y)\rho \frac{\partial \mu_n}{\partial \rho}, \quad (4.75)$$

to obtain an expression for the pressure,

$$P(\rho, y, \beta) = -a_0 \rho^2 + a_3 (1+\sigma) \rho^{\sigma+2} + \frac{\rho}{\beta} \left[\frac{1}{1-b\rho} + \sum_{n=1}^{\infty} b_n \left(\frac{\Lambda^3 \rho}{g_s} \right)^n (y^{n+1} + (1-y)^{n+1}) \right]. \quad (4.76)$$

This equation of state has potential terms that are somewhat similar to the van der Waals EOS (having a repulsive higher-order density term) but the thermal terms are markedly different at low temperature and become equivalent in the limit of high temperature. These equations are then used to solve for densities and proton fractions satisfying Gibbs's conditions in order to find the coexistence binodal.

Results

Figure 4.11 shows a two-dimensional slice of the binodal surface with and without finite Coulomb interactions at symmetry. These binodal surfaces are qualitatively similar to the one found for the van der Waals model, although scaled up in temperature and thus in better agreement with more sophisticated EOSs. The critical point of the system without Coulomb is $T_c = 12.1$ MeV, which is ≈ 3 MeV less than the generally accepted value of ~ 15 MeV. The predicted critical point of the model with finite Coulomb interactions is again found to be approximately 2 MeV less than the system without Coulomb. Here however we also see the effect of a Coulomb induced “limiting temperature”, that is to say that Gibbs’s conditions could not be satisfied all the way to the critical point. This phenomenon was predicted some time ago in a temperature-dependent Hartree-Fock model that utilized a Skyrme interaction that is quite similar to the one used in this study[100]. In that study it was found that there were no bound protons above a “limiting temperature”. It was noted that this was due to a “Coulomb instability”. An analogous situation is found here with the inability for phase coexistence above a limiting temperature. The limiting temperature found here is rather high being ~ 10.5 MeV but would be further reduced by the inclusion of surface corrections.

Figure 4.12 is a similar plot to figure 4.10, except that it shows the results from the Hard-Core Skyrme Model. Both the dashed lines, which show the results of the calculation without finite Coulomb, and the solid lines, which show the results of the calculation with finite Coulomb interactions, are qualitatively similar to the results found in the Two-Component van der Waals Model. The inclusion of an isospin asymmetry energy in this case, however, shows a less pronounced fractionation effect at higher temperature. This is especially evidenced by the shift of the azeotrope back near symmetry for the results at 10 [MeV]. Still at moderate temperatures ($\approx 4 - 8$ [MeV]) the fractionation found in this calculation is as significant as that predicted by the van der Waals model. Thus, despite the weakening of the isospin asymmetry energy at higher temperatures a significant N/Z fractionation can be expected if the temperature attained by system remains moderate.

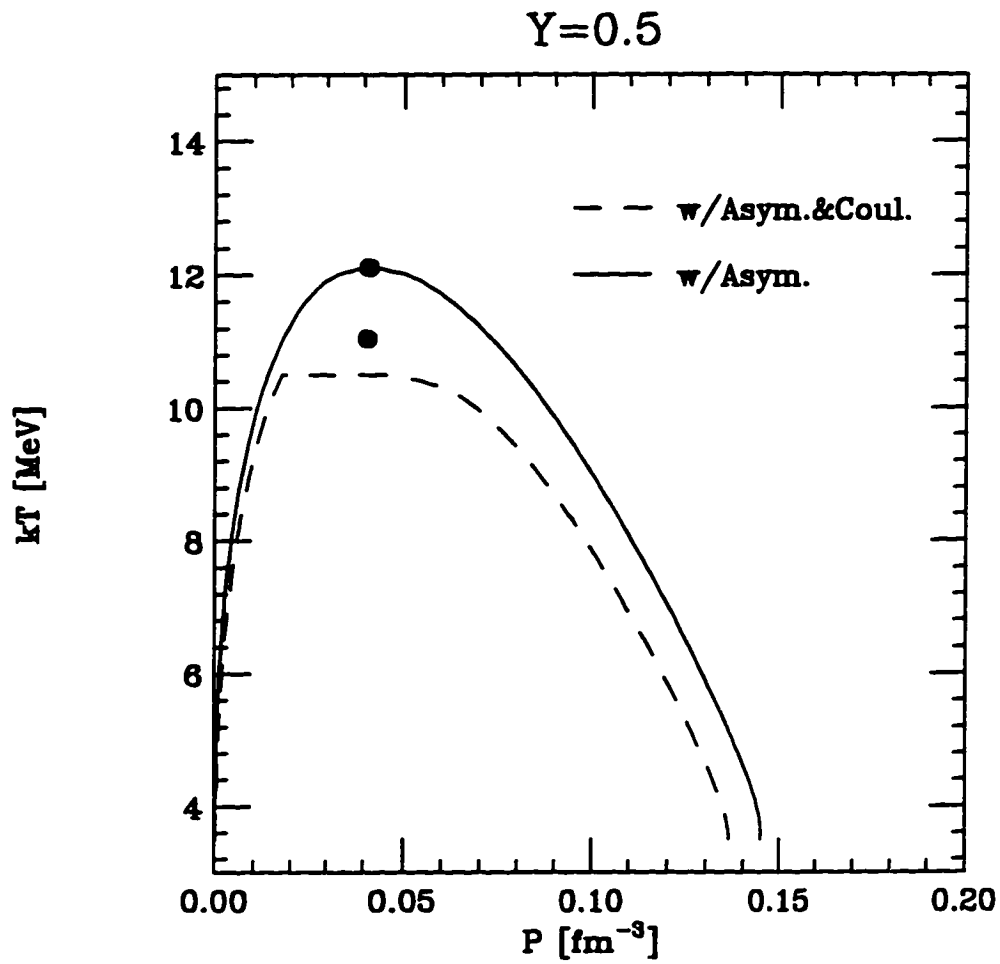


Figure 4.11: The liquid-gas phase coexistence curve for symmetry ($Y=0.5$) with and without Coulomb for the two-component Skyrme liquid.

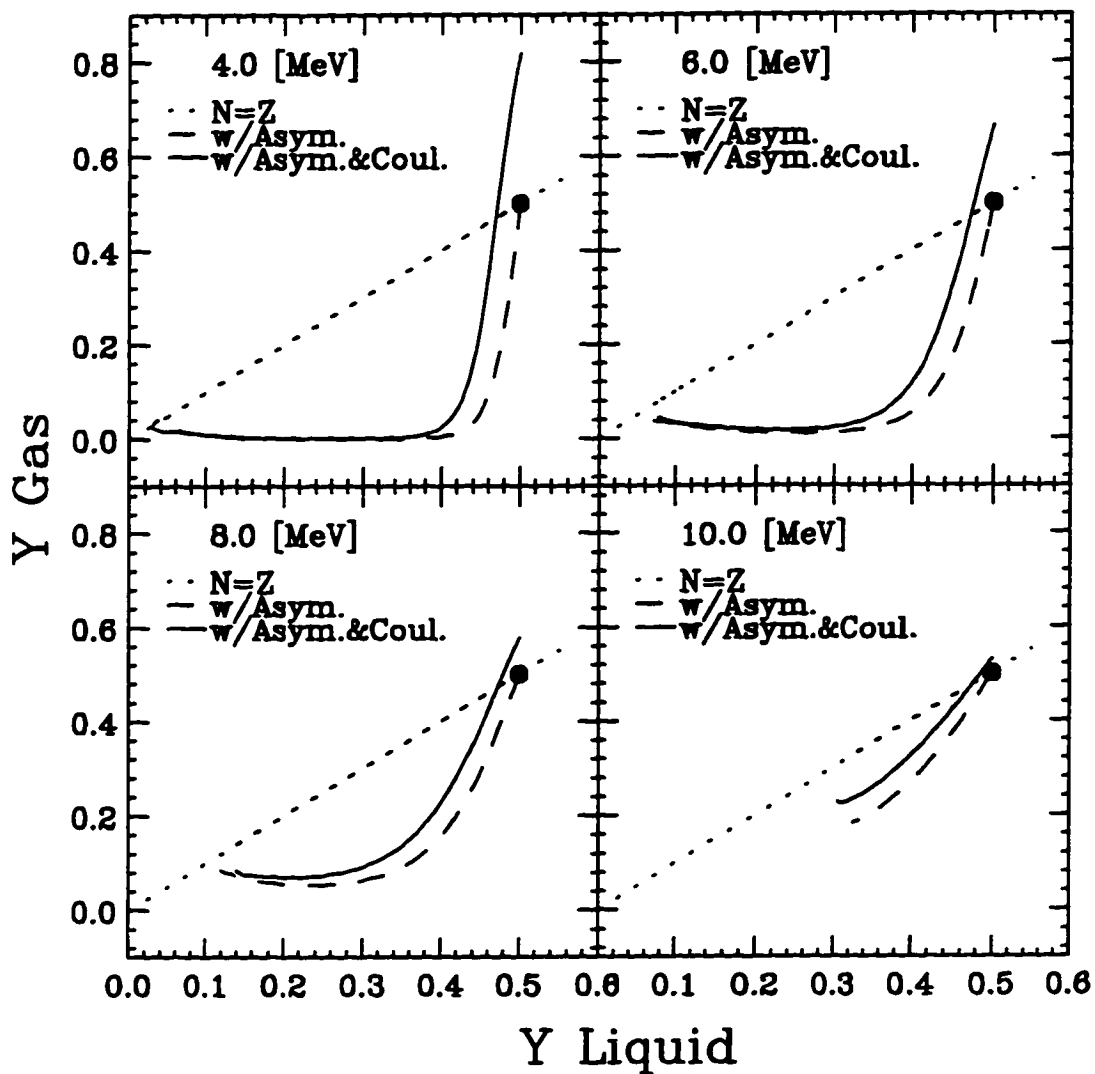


Figure 4.12: The proton fraction found in the low-density phase Y_{gas} as a function of the proton fraction found in the high-density phase Y_{liquid} at equilibrium for four different temperatures with Coulomb (solid line) and without Coulomb (dashed line) for the Hard-Core Skyrme Model. The dotted line marks equal concentrations in the phases. Above this line the gas phase is proton rich and below this line the gas phase is neutron rich relative to the liquid phase.

4.3.4 Summary

In summary, the N/Z degree of freedom has some very interesting features inside the liquid-gas phase coexistence region expected for asymmetric nuclear matter. Namely, an N/Z fractionation among different density phases is predicted and this prediction can be significantly altered by the inclusion of finite Coulomb interactions in the EOS. The temperature and density dependence of the isospin asymmetry energy can also strongly influence this prediction.

Future studies of this N/Z fractionation in the framework of either a mesoscopic model, such as a temperature-dependent Thomas-Fermi calculation, or microscopic model, such as a temperature-dependent Hartree-Fock calculation which include a proper treatment of the N/Z degree of freedom and the Coulomb interaction may provide a means for predicting an equilibrium N/Z observable for IMFs. This prediction can then be compared to the N/Z signature of multifragmentation observed in this and future studies to determine the relevance (if any) of the liquid-gas phase transition to the phenomenon of multifragmentation.

Chapter 5

Conclusions

5.1 Experimental Findings

The present work examines a set of systems, $^{124,136}\text{Xe} + ^{112,124}\text{Sn}$ at 55 MeV*A, which allowed for a study of the influence of entrance-channel N/Z ratio on the production of IMFs. The data indicate that both the incremental neutron-to-charged-particle emission ratios and the production of IMFs are nearly identical for all four systems when viewed as functions of excitation energy. Projectile-like fragments detected at forward angles display only a small amount of velocity damping and the average damping is independent of the size of the remnant while the variation in damping grows with decreasing remnant size. The Galilean-invariant cross-section maps of LCPs indicate that they originate mainly from the sequential decay of TLF and PLF sources, while the IMF maps show that they emanate mainly from the mid-velocity region. Azimuthal correlations between PLFs and IMFs show that much of the IMF production is inconsistent with simple sequential decay. These observations are consistent with the observations of previous studies of similarly heavy systems at intermediate energy which attribute such features to a neck fragmentation or directed fission mechanism. Isobaric and isotopic ratios of fragments as a function of velocity parallel to the beam show that fragments emitted from the mid-velocity region are neutron rich relative to those emitted from the projectile-velocity region. These ratios also confirm the expected lack of complete charge equilibration or neutralization for intermediate energy collisions.

Taken together, the observations of this work suggest that the intermediate-mass fragments are, to a large extent, formed dynamically by a multiple neck rupture

or proximity fission type mechanism. Although it remains unexplained, this process enhances the neutron-to-proton ratio of the emitted fragments.

5.2 Theoretical Insights

Statistical-model simulations were used to explore possible explanations for the neutron richness of fragments emitted in the mid-velocity region. It has been shown that differences in initial excitation or angular momentum can not explain this trend. This trend can be qualitatively accounted for if the mid-velocity source (or sources) is either more neutron rich or smaller, with the same neutron-to-proton ratio, than the source with the velocity of the projectile. An attempt to reproduce the values of N_n/N_c as a function of Z_{plf} or the dependence of $\langle N_n \rangle$ on N_c with statistical-model calculations was also performed. The exercise of reproducing the dependence of these quantities was found to be very sensitive to the prescription of the level-density parameter a and hence under determined. The differences observed in the increasing maximum value of $\langle N_{imf} \rangle$ with increasing N/Z of the system were also studied within the framework of the statistical model. It was found that this trend can be completely explained by differences in the survivability of the primary IMFs. This can be understood as being due to a simple neutron enrichment of IMFs from a neutron-rich system that increases the probability of neutron emitting sequential decay that preserves the $Z \geq 3$ IMF definition.

BUU reaction model simulations were run to compare with PLF observables. The model makes a significant over prediction of the amount of velocity damping for the PLF. The data have a negligible cross section (less than 100 mb) for the production of PLFs with values of E/A less than 40 MeV while the calculations predict large cross sections (as much as 1 b) in this energy region. This discrepancy is decreased by using a softer equation of state, including an asymmetric term in the mean field, or reducing the nucleon-nucleon cross section. The inclusion of light-cluster degrees of freedom into the BUU transport equation has led to the discovery of an interesting mechanism that may be responsible for the preponderance of neutron-rich species in the mid-velocity region. More refined models will be necessary to confirm this result. BUU simulations without this clustering mechanism are incapable of producing a significantly neutron-rich mid-velocity region.

The behavior of the N/Z degrees of freedom in the liquid-gas phase-coexistence region of nuclear matter was investigated. The concentrations of neutrons and protons were found to fractionate among the different density phases at equilibrium. Two simple models were implemented to determine the influence of finite Coulomb interactions and an isospin asymmetry energy that is both density and temperature dependent. These influences were found to significantly modify the nature of the fractionation.

5.3 Future Studies

At the end of this study, the question posed in the introduction, "What does the production of these IMFs indicate?", remains unanswered. The elusive mechanism or mechanisms behind the phenomenon of multifragmentation seem to be very difficult prey indeed. The results of this study[101], however have made definite progress toward realizing the objectives declared in the introduction. The remarkable N/Z signature of LCPs and IMFs produced in the mid-velocity region for all of the collisions studied provides a promising new observable with which the phenomenon of multifragmentation may eventually be subdued. Future study of this feature has already begun on both experimental and theoretical fronts. Experimentally, a study to search for the evolution of the N/Z of IMFs with increasing fragment mass has already been approved at the NSCL and will be performed sometime in the summer of 1997, by the research group of Sobotka and Charity. Theoretically, this work has shown that a definite and interesting N/Z observable exists in the equilibrium limit and provides the incentive for the inclusion of the N/Z degree of freedom in the many fragmentation models that already exist. A theoretical working group has already been formed by a dozen or so theorists from Europe, with the express intent of exploring the behavior of N/Z degree of freedom in intermediate-energy heavy-ion collisions. (The author was lucky enough to have attended the first meeting of this working group and draw special attention to the results of the work presented in this thesis). Comparison of the equilibrium N/Z expectations with isotopically resolved IMF yields, over the full range of observed masses, may eventually provide a means to establish the relevance, or lack of relevance, of a liquid-gas phase transition in nuclear matter to the phenomenon of multifragmentation. Dynamical reaction models will of course

have to meet the same standards in supporting a neck-rupture mechanism scenarios, when they too are ready to meet the challenge.

Bibliography

- [1] L.G. Moretto and G.J. Wozniak, *Ann. Rev. Nucl. Part. Sci.* **43**, 379 (1993).
- [2] H.J. Rose and G.A. Jones, *Nature*, **307**, 245 (1984).
- [3] P.B. Price, *Ann. Rev. Nucl. Part. Sci.* **39**, 19 (1989).
- [4] A.M. Poskanzer, R.G. Sextro, A.M. Zebelman, H.H. Gutbrod, A. Sandoval, and R. Stock, *Phys. Rev. Lett.* **35**, 1701 (1975).
- [5] L.G. Sobotka, M.L. Padgett, G.J. Wozniak, G. Guarino, A.J. Pacheco, L.G. Moretto, Y. Chan, R.G. Stokstad, I. Tserruya, and S. Wald, *Phys. Rev. Lett.* **51**, 2187 (1983).
- [6] M.B. Tsang, W.C. Hsi, W.G. Lynch, D.R. Bowman, C.K. Gelbke, M.A. Lisa, G.F. Peaslee, G.J. Kunde, M.L. Begemann-Blaich, T. Hofmann, J. Hubele, J. Kempter, P. Kreutz, W.D. Kunze, V. Lindenstruth, U. Lynen, M. Mang, W.F. Müller, M. Neumann, B. Ocker, C.A. Ogilvie, J. Pochodzalla, F. Rosenberger, H. Sann, A. Schüttauf, V. Serfling, J. Stroth, W. Trautmann, A. Tucholski, A. Wörner, E. Zude, B. Zwieglinski, S. Aiello, G. Immé, V. Pappalardo, G. Raciti, R.J. Charity, L.G. Sobotka, I. Iori, A. Moroni, R. Scardoni, A. Ferrero, W. Seidel, Th. Blaich, L. Stuttge, A. Cosmo, W.A. Friedmann, G. Peilert, *Phys. Rev. Lett.* **71**, 1502 (1993).
- [7] R.G. Palmer and P.W. Anderson, *Phys. Rev. D* **9**, 3281 (1974).
- [8] W.G. Kupper, G. Wegmann, and E.R. Hilf, *Ann. Phys.* **88**, 454 (1974).
- [9] G. Sauer, H. Chandra, and U. Mosel, *Nucl. Phys.* **A264**, 221 (1976).
- [10] J.M. Lattimer and D.G. Ravenhall, *Astrophys. J.* **223**, 314 (1978).
- [11] P. Danielewicz, *Nucl. Phys.* **A314**, 465 (1979).
- [12] M. Barranco and J.R. Buchler, *Phys. Rev. C* **22**, 1729 (1980).

- [13] D.Q. Lamb, J.M. Lattimer, C.J. Pethick, and D.G. Ravenhall, Nucl. Phys. **A360**, 459 (1981).
- [14] H. Schulz, L. Munchow, G. Ropke, and M. Schmidt, Phys. Lett. **B119**, 12 (1982), Nucl. Phys. **A399**, 587 (1983).
- [15] M.W. Curtin, H. Toki, and D.K. Scott, Phys. Lett. **B123**, 289 (1983).
- [16] A.D. Panagiotou, M.W. Curtin, H. Toki, D.K. Scott, and P.J. Siemens, Phys. Rev. Lett. **52**, 496 (1984).
- [17] J.M. Lattimer, C.J. Pethick, D.G. Ravenhall, and D.Q. Lamb, Nucl. Phys. **A432**, 646 (1985).
- [18] N.K. Glendenning, Phys. Rev. **D46**, 1274 (1992).
- [19] H. Müller and B. D. Serot, Phys. Rev. **C52**, 2072 (1995).
- [20] J. Randrup and S. Koonin, Nucl. Phys. **A356**, 223 (1981).
- [21] D.H.E. Gross, L. Sapathy, M. Ta-chung, and M. Sapathy, Z. Phys. **A309**, 41 (1982).
- [22] G. Fai and J. Randrup, Nucl. Phys. **A381**, 557 (1982), Nucl. Phys. **A404**, 551 (1983).
- [23] G. Bertsch and P.J. Siemens, Phys. Lett. **B126**, 9 (1983).
- [24] H. Jaqaman, A.Z. Mekjian, and L. Zamick, Phys. Rev. **C27**, 2782 (1983).
- [25] J. Aichelin and J. Hufner, Phys. Lett. **B136**, 15 (1984).
- [26] H.R. Jaqaman, A.Z. Mekjian, and L. Zamick, Phys. Rev. **C29**, 2067 (1984).
- [27] D.H.E. Gross and X. Zhang, Phys. Lett. **B161**, 47 (1985).
- [28] J. Bondorf, R. Donangelo, I. Mishustin, C. Pethick, H. Schulz, and K.Sneppen, Nucl. Phys. **A443**, 321 (1985).
- [29] J. Bondorf, R. Donangelo, I. Mishustin, C. Pethick, H. Schulz, and K.Sneppen, Nucl. Phys. **A443**, 321 (1985).
- [30] J. Bondorf, R. Donangelo, I. Mishustin, and H. Schulz, Nucl. Phys. **A444**, 460 (1985).
- [31] D.H. Boal, Nucl. Phys. **A447**, 479c (1985).

- [32] B.M. Waldhauser, J. Theis, J.A. Maruhn, H. Stöcker, and W. Greiner, *Phys. Rev. C* **36**, 1019 (1987).
- [33] G. Fai and A. Mekjian, *Phys. Lett. B* **169**, 281 (1987).
- [34] J. Diaz Alonso, J.M. Ibañez, and H. Sivak, *Phys. Rev. C* **39**, 671 (1989).
- [35] V.R. Pandharipande and D.G. Ravenhall, in *Nuclear Matter and Heavy-Ion Collisions*, Proceedings of the 1989 Les Houches Winter School, edited by M. Soyeur, H. Flocard, B. Tamain, and M. Porneuf (Plenum, New York, 1989).
- [36] A.R. DeAngelis and A. Mekjian, *Phys. Rev. C* **40**, 105 (1990).
- [37] D.R. Bowman, C.M. Mader, G.F. Peaslee, W. Bauer, N. Carlin, R.T. de Souza, C.K. Gelbke, W.G. Gong, Y.D. Kim, M.A. Lisa, W.G. Lynch, L. Phair, M.B. Tsang, C. Williams, N. Colonna, K. Hanold, M.A. McMahan, G.J. Wozniak, L.G. Moretto and W.A. Friedman, *Phys. Rev. C* **46**, 1834 (1992).
- [38] W.A. Friedman, *Phys. Rev. Lett.* **60**, 2125(1988) and *Phys. Rev. C* **42**, 667(1990).
- [39] V. Weisskopf, *Phys. Rev.* **52**, 295(1937).
- [40] B. Lott, S.P. Baldwin, B.M. Szabo, B.M. Quednau, W.U.Schröder, J. Töke, L.G. Sobotka, J. Barreto, R.J. Charity, L. Gallamore, D.G. Sarantites, D.W. Stracener, and R.T. de Souza, *Phys. Rev. Lett.* **68**, 3141 (1992).
- [41] C.P. Montoya, W.G. Lynch, D.R. Bowman, G.F. Peaslee, N. Carlin, R.T. de Souza, C.K. Gelbke, W.G. Gong, Y.D. Kim, M.A. Lisa, L. Phair, M.B. Tsang, J.B. Webster, C. Williams, N. Colonna, K. Hanold, M.A. McMahan, G.J. Wozniak, L.G. Moretto, *Phys. Rev. Lett.* **73**, 3070 (1994).
- [42] J. Töke, B. Lott, S.P. Baldwin, B.M. Quednau, W.U.Schröder, L.G. Sobotka, J. Barreto, R.J. Charity, D.G. Sarantites, D.W. Stracener, and R.T. de Souza, *Phys. Rev. Lett.* **75**, 2920 (1995).
- [43] A.A. Stefanini, C. Casini, P.R. Maurenzig, A. Olmi, R.J. Charity, R. Freifelder, A. Gobbi, N. Herrmann, K.D. Hildenbrand, M. Petrovici, F. Rami, H. Stelzer, J.P. Wessels, M. Gnirs, D. Pelte, J. Galin, D. Guerreau, U. Jahnke, A. Pèghaire, J.C. Adloff, B. Bilwes, R. Bilwes, and G. Rudolf, *Z. Phys. A* **351**, 167 (1995).
- [44] C. Wagemans, in *The Nuclear Fission Process*, edited by C. Wagemans (CRC Press, Boca Raton, 1991) p. 545.

- [45] U. Brosa, S. Grossmann, and A. Müller. Phys. Rep. **197**, 167 (1990).
- [46] M.B. Tsang, G.F. Bertsch, W.G. Lynch, and M. Tohyama, Phys. Rev. C **40**, 1685 (1989).
- [47] L.G. Sobotka, Phys. Rev. C **50**, R1272 (1994).
- [48] P. Lubiński, J. Jastrzębski, A. Grochulska, A. Stolarz, A. Trzcńska, W. Kurcewicz, F.J. Hartmann, W. Schmid, T. von Egidy, J. Skalski, R. Smolańczuk, S. Wycech, D. Hilscher, D. Polster, and H. Rossner, Phys. Rev. Lett. **73**,3199(1994).
- [49] T. Suzuki, H. Geissel, O. Bochkarev, L. Chulkov, M. Golovkov, D. Hirata, H. Irnich, Z. Janas, H. Keller, T. Kobayashi, G. Kraus, G. Münzenberg, S. Neumaier, F. Nickel, A. Ozawa, A. Piechaczek, E. Roeckl, W. Schwab, K. Sümmerer, K. Yoshida, and I. Tanihata, Phys. Rev. Lett. **75**,3241(1995).
- [50] B.A. Brown and W.A. Richter, Phys. Rev. C **54**, 673 (1996).
- [51] Design S from: Micron Semiconductor, 1 Royal Buildings, Marlborough Road, Churchill Industrial Estate, Lancing, Sussex BN15 8UN, England. This device is sectioned into 4 sets of 16 radial strips each and 16 azimuthal (pie shaped) sectors.
- [52] Private communication from Jon Elson.
- [53] D.G. Sarantites, P-F. Hua, P.-F., M. Devlin, L.G. Sobotka, J. Elson, J.T. Hood, D.R. LaFosse, J.E. Sarantites, M.R. Maier, Nucl. Instru. Meth. **A381**, 418 (1996).
- [54] N. Colonna, G.J. Wozniak, A. Veeck, W. Skulski, G.W. Goth, L. Manduci, P.M. Milazzo, and P.F. Mastinu, Nucl. Instru. Meth. **A321**, 529 (1992).
- [55] *Numerical Recipes in FORTRAN: the Art of Scientific Computing*, W.H. Press Editor, 2nd Ed., (Cambridge University Press, 1992).
- [56] J.B. Birks, *The Theory and Practice of Scintillation Counting*, (Permagon, 1964) p. 465
- [57] J. Alarja, A. Dauchy, A. Giorni, C. Morand, E. Pollaco, P. Stassi, R. Billerey, B. Chambon, B. Cheynis, D. Drain, and C. Pastor, Nucl. Instru. Meth. **A242**, 352 (1985).

- [58] R.J. Charity, L.G. Sobotka, N.J. Robertson, D.G. Sarantites, J. Dinius, C.K. Gelbke, T. Glasmacher, D.O. Handzy, W.C. Hsi, M.J. Huang, W.G. Lynch, C.P. Monotoya, G.F. Peaslee, C. Schwarz, and M.B. Tsang, *Phys. Rev. C* **52**, 3126 (1995).
- [59] R.T. deSouza, N. Carlin, Y.D. Kim, J. Ottarson, L. Phair, D.R. Bowman, C.K. Gelbke, W.G. Gong, W.G. Lynch, R.A. Pelak, T. Peterson, G. Poggi, M.B. Tsang, and H.M. Xu, *Nucl. Instru. Meth.* **A295**, 109 (1990).
- [60] D.W. Stracener, D.G. Sarantites, L.G. Sobotka, J. Elson, J.T. Hood, Z. Majka, V. Abenante, and A. Chbihi, *Nucl. Instru. Meth.* **A294**, 485 (1990).
- [61] Private communication with Jan Töke, University of Rochester.
- [62] The Superball is described in detail in the unpublished report, W.U. Schröder, University of Rochester Report DOE-ER-79048-1, (1995).
- [63] J.F. Lecolley, L. Stuttgé, M. Aboufirassi, A. Badala, B. Bilwes, R. Bougault, R. Brou, F. Cosmo, J. Colin, D. Durand, J. Galin, A. Genoux-Lubain, D. Guerreau, D. Horn, D. Jacquet, J.L. Laville, F. Lefebvres, C. Le Brun, J. Lemiére, O. Lopez, M. Louvel, M. Mahi, M. Morjean, C. Paulot, A. Pèghaire, N. Prot, G. Rudolf, F. Scheibling, J.C. Steckmeyer, B. Tamain, S. Tomasevic, *Phys. Lett. B* **325**, 317 (1994).
- [64] S.P. Baldwin, B. Lott, B.M. Szabo, B.M. Quednau, W.U.Schröder, J. Töke, L.G. Sobotka, J. Barreto, R.J. Charity, L. Gallamore, D.G. Sarantites, D.W. Stracener, and R.T. de Souza, *Phys. Rev. Lett.* **74**, 1299 (1995).
- [65] R.J. Charity, D.R. Bowman, Z.H. Liu, R.J. McDonald, M.A. McMahan, G.J. Wozniak, L.G. Moretto, S. Bradley, W.L. Kehoe, and A.C. Mignerey, *Nucl. Phys.* **A476**, 516 (1988).
- [66] R. Planeta, S.H. Zhou, K. Kwiatkowski, W.G. Wilson, V.E. Viola, H. Breuer, D. Benton, F. Khazaie, R.J. McDonald, A.C. Mignerey, A. Weston-Dawkes, R.T. de Souza, J.R. Huizenga, and W.U. Schröder, *Phys. Rev. C* **38**, 195 (1988).
- [67] S.J. Yennello, B. Young, J. Yee, J.A. Winger, J.S. Winfield, G.D. Westfall, A. Vander Molen, B.M. Sherrill, J. Shea, E. Norbeck, D.J. Morrissey, T. Li, E. Gualtieri, D. Craig, W. Benenson, and D. Bazin, *Phys. Lett.* **B321**, 15 (1994).
- [68] J.M. Alexander, M.T. Magda, and S. Landowne, *Phys. Rev. C* **42**, 1092 (1990).



- [69] Computer code GEMINI, R.J. Charity. The code is available via anonymous FTP from WUNMR.WUSTL.EDU in directory /pub/gemini.
- [70] W. Hauser and H. Feshbach, *Phys. Rev.* **87** 366 (1952).
- [71] N. Bohr and J.A. Wheeler, *Phys. Rev.* **56**, 426 (1939).
- [72] S. Landowne and S.C. Pieper, *Phys. Rev.* **C29**, 1352 (1984).
- [73] C.M. Perey and F.G. Perey, *ADNDT* **17**, 1 (1976).
- [74] H. Bethe, *Rev. Mod. Phys.* **9**, 69 (1937).
- [75] A. Bohr and B. Mottelson, *Nuclear Structure Vol. 1*, Benjamin, New York (1969).
- [76] W. E. Ormand, P.F. Bortignon, A. Bracco, and R.A. Broglia, *Phys. Rev. C* **40**, 1510 (1989).
- [77] W.A. Friedman and W.G. Lynch, *Phys. Rev.* **C28**,16 (1983).
- [78] N.G. Nicolis, D.G. Sarantites, L.G. Sobotka, and R.J. Charity, *Phys. Rev.* **C45**, 2393 (1992).
- [79] E.A. Uehling and G.E. Uhlenbeck, *Phys. Rev.* **43**, 552 (1933), *Phys. Rev.* **46**, 917 (1934).
- [80] W. Bauer, *Prog. Part. Nucl. Phys.* **30**, 45 (1993).
- [81] C.Y. Wong, *Phys. Rev. C* **25**, 1460 (1982).
- [82] K.T.R. Davies, K.R. Sandhya Devi, M. R. Strayer, *Phys. Rev. C* **20**, 1372 (1979).
- [83] N. Cârjan, A. Sierk, and J.R. Nix, *Nucl. Phys.* **A452**, 381 (1986).
- [84] G. D. Westfall, W. Bauer, D. Craig, M. Cronqvist, E. Gaultieri, S. Hannuschke, D. Klakow, T. Li, T. Reposeur, A.M. Vander Molen, W.K. Wilson, J.S. Winfield, J. Yee, S.J. Yennello, R. Lacey, A. Elmaani, J. Lauret, A. Nadasen, and E. Norbeck. *Phys. Rev. Lett.* **71**, 1986 (1993).
- [85] P.G. Reinhard and E. Suraud, *Nucl. Phys.* **A545**, 59c (1992).
- [86] P. Danielewicz and G.F. Bertsch. *Nucl. Phys.* **533**, 712 (1991).
- [87] P. Danielewicz. *Phys. Rev. C* **51**, 716 (1995).
- [88] H.A. Bethe, *Ann. Rev. Nucl. Sci.*, **21**, 93 (1971).
- [89] L.G. Sobotka, J.F. Dempsey, R.J. Charity, and P. Danielewicz. *Phys. Rev. C* in press.

- [90] P.G. Reinhard and E. Suraud, *Ann. Phys.* **216**, 98 (1992).
- [91] J.E. Finn, S. Agarwal, A. Bujak, J. Chuang, L. Gutay, A.S. Hirsch, R.W. Minich, N.T. Porile, R.P. Scharenberg, B.C. Stringfellow, and F. Turkot, *Phys. Rev. Lett.* **49**, 1321 (1982)
- [92] H.H. Gutbrod, A.I. Warwick, and H. Wieman, *Nucl. Phys.* **A387**, 177c (1982).
- [93] M. Fisher, *Physics* **3**, 255 (1967).
- [94] P.J. Siemens, *Nature*, **305**, 410 (1983).
- [95] A. Meibom and I. Balslev *Phys. Rev. Lett.*, **76**, 2492 (1996).
- [96] L.G. Sobotka and L.G. Moretto, *Phys. Rev.* **C31**, 668 (1988).
- [97] M. Prakash, T.L. Ainsworth, and J.M. Lattimer, *Phys. Rev. Lett.* **61**, 2518 (1988).
- [98] H.R. Jaqaman. *Phys. Rev.* **C39** 169 (1989).
- [99] D.A. McQuarrie, "Statistical Thermodynamics", (University Science Books, 1973) p. 162.
- [100] P. Bonche, S. Levit, and D. Vautherin, *Nucl. Phys.* **A436**, 265 (1985).
- [101] J.F. Dempsey, R.J. Charity, L.G. Sobotka, G.J. Kunde, S. Gaff, C.K. Gelbke, T. Glasmacher, M.J. Huang, R.C. Lemmon, W.G. Lynch, L. Manduci, L. Martin, M.B. Tsang, D.K. Agnihortri, B. Djerround, W.U. Schröder, W. Skulski, J. Töke, and W.A. Friedman. *Phys. Rev.* **C54**, 1710 (1996).